Application of Cavity Expansion Analysis to Penetration Problems

S. Satapathy
Institute for Advanced Technology
The University of Texas at Austin

July 1997

IAT.R 0136

19971016 146

Institute for Advanced Technology
The University of Texas at Austin

REPORT DOCUMENTATION PAGE

1. AGENCY USE ONLY (Leave blank)	2. REPORT DATE July 1997	3. REPORT TYPE AND DATES COVERED Technical Report Sept 93- April 97

4. TITLE AND SUBTITLE

Application of Cavity Expansion Analysis to Penetration Problems

5. FUNDING NUMBERS

Contract # DAAA21-93-C-0101

6. AUTHOR(S)

S. Satapathy

7. PERFORMING ORGANIZATION NAME(S) AND ADDRESS(ES)

Institute for Advanced Technology
The University of Texas at Austin
4030-2 W. Braker Lane, #200
Austin, TX 78759

8. PERFORMING ORGANIZATION REPORT NUMBER

IAT.R 0136

9. SPONSORING / MONITORING AGENCY NAME(S) AND ADDRESS(ES)

U.S. Army Research Laboratory
ATTN: AMSRL-WT-T
Aberdeen Proving Ground, MD 21005-5066

10. SPONSORING / MONITORING AGENCY REPORT NUMBER

11. SUPPLEMENTARY NOTES

The view, opinions and/or findings contained in this report are those of the author(s) and should not be considered as an official Department of the Army position, policy, or decision, unless so designated by other documentation.

12a. DISTRIBUTION / AVAILABILITY STATEMENT

Approved for public release; distribution unlimited.

12b. DISTRIBUTION CODE

A

13. ABSTRACT (Maximum 200 words)

Cavity Expansion Analysis (CEA) is extended in three different areas: a) analysis of ductile targets accounting for finite boundaries and finite ductility; b) analysis of brittle ceramics considering the cracking and comminution behavior; c) development of a new penetration model for metals to overcome limitations of the existing models. CEA is modified to account for a finite boundary and to incorporate the effects of finite ductility of metallic targets, which develop tensile cracks. The results of the analyses are shown to be in good agreement with test data. A constitutive behavior based on the current understanding of the brittle behavior is used to derive quasi-static and dynamic cavity expansion pressures. Important material parameters that affect the penetration resistance are identified. The cavity expansion pressure derived in this analysis is in excellent agreement with experimental penetration resistance values. The existing penetration models do not always agree with the experimental penetration behavior of eroding rod projectiles at different velocities. A new approach is hypothesized to model the penetration in ductile targets. In addition to the elastic and plastic zones, a "damaged zone" zone is recognized in the target. In comparison to the existing models, the new approach shows superior agreement with experimental data, both for low and high velocities.

14. SUBJECT TERMS

cavity expansion analysis, ceramics, penetration resistance, punch tests, penetration models

15. NUMBER OF PAGES

155

16. PRICE CODE

17. SECURITY CLASSIFICATION OF REPORT	18. SECURITY CLASSIFICATION OF THIS PAGE	19. SECURITY CLASSIFICATION OF ABSTRACT	20. LIMITATION OF ABSTRACT
Unclassified	Unclassified	Unclassified	UL

Preface

This report constituted the PhD thesis of Sikanda Satapathy that was submitted to and approved by the University of Texas, Department of Mechanical Engineering in May 1997. Dr. Satapathy is now employed by the Institute for Advanced Technology, where development of penetration theories for ceramics is continuing.

Table of Contents

List of Figures

List of Tables

Application of Cavity Expansion Analysis to Penetration Problems

Sikhanda Satapathy

Chapter 1: Introduction

1.1   Motivation and objective

The problem of penetration of a projectile into metallic and ceramic targets has received extensive attention from the research community. Given the geometry of impact and the material properties of the penetrator and target, the primary goal is to predict the depth of penetration. Furthermore, for finite targets, determination of the ballistic limit and the characteristics of the ejecta behind the target are important. This research finds application in a wide variety of problems involving impact and penetration, such as armor and anti-armor design and protection of space structures from orbital debris and meteoritic impact. In addition, the analysis can aid in the design and evaluation of protective structures for high-speed machinery such as turbines, in the determination of vehicle crash-worthiness, and in the design and evaluation of nuclear reactor containment.

There have been several review articles on different aspects of penetration mechanics (Zukas 1990; Herrman and Wilbeck 1987; Backman and Goldsmith 1977; Johnson 1972). The various physical phenomena that occur in the impact and penetration situation include wave propagation, elastic-plastic deformation, crack formation and propagation, petalling, plugging and spalling, shear band formation, melting and phase change, and fragmentation. While most of the above phenomena belong to distinct established areas of science, in impact and penetration mechanics one has to deal with the entire gamut of these physical phenomena, which makes the subject complicated. Depending on the penetration regime, different phenomena predominate. The mechanics of penetration varies for different impact velocities, material properties and geometries of the penetrator and the target. For example, the phenomena that exist near ballistic limit penetration (like spall fracture, petalling, plugging, etc.) are absent in semi-infinite target penetration (Figures 1.1-a, b). Similarly, at very high impact velocities, the projectile penetration can be explained by fluid flow models. At low velocities, the penetration is explained by elastic-plastic deformation and wave propagation.

1
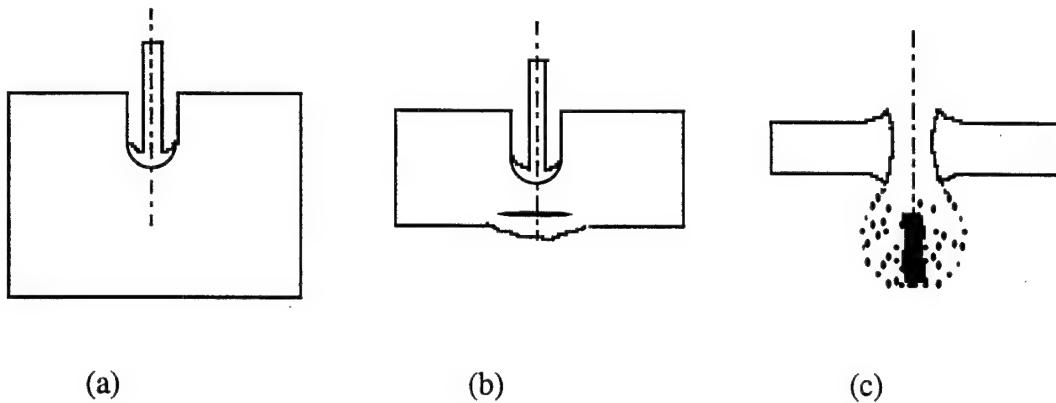
Figure 1.1. Effect of target thickness on penetration mechanics.

One of the most important parameters used in penetration analysis is the resistance of the target material to impact and penetration. In conjunction with some form of Newton's second law, one uses the target resistance value to predict the depth of penetration, size of the cavity made, deceleration and erosion of the projectile, and other dynamic response characteristics. In the break-out problem (Figure 1.1-c), one is concerned with the mass and momentum distribution of the ejecta after the projectile passes through the target/ armor. In such cases, modeling the penetration of the finite target is necessary before any attempt can be made to describe the residual characteristics.

In this dissertation cavity expansion analyses are used to calculate target resistance values for metals and ceramics. The problems of cavity expansion in ductile and brittle materials are completely different. While ductile materials flow plastically and eventually fail under increasing applied load, brittle materials develop extensive cracking and comminution (Figure 1.2). This behavior complicates the analysis of brittle materials. Introduction of a finite boundary changes the penetration resistance values of both metals and ceramics significantly. There is no physically based model to quantify this effect for use in penetration equations. Furthermore, in metals having relatively low failure strain, a cracked zone is observed near the penetration channel. Finite ductility seems to play a role for such cases. To capture the physics of these different kinds of situations, the analyses are necessarily specialized depending on the case at hand.
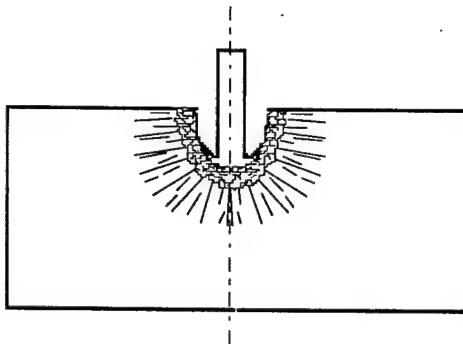
Figure 1.2. Penetration phenomenology of brittle materials.

The main objectives of this research were:

a) To present a complete account of the existing cavity expansion theory for ductile and brittle materials;

b) To extend the cavity expansion theory for certain cases of practical importance, i.e., for finite metal targets where presence of a finite boundary affects the penetration resistance, and for brittle metallic targets which show a distinct cracked zone surrounding the penetration channel;

c) To derive quasi-static and dynamic cavity expansion pressures for brittle ceramics and identify and quantify the important material parameters that influence their penetration resistance;

d) To critically analyze the application of cavity expansion theory for modeling the penetration resistance parameter.

1.2   Organization and summary of research

In this chapter the existing literature on cavity expansion theory is reviewed briefly and a summary of this research is presented. Cavity expansion analyses of ductile materials are described in Chapter 2. Existing incompressible and compressible theories are presented for both static and dynamic cavity expansions. The effect of finite ductility on the cavity expansion pressure is then quantified in a new analysis. The effect of a finite boundary on the penetration resistance is investigated. Comparisons with experimental data are presented. Quasi-static punch

3

experiments performed on PMMA are then described and cavity expansion analysis is used to model these experiments. Finally, the theoretical predictions of load-displacement curves and the size of the plastic zone are compared with the experimental data.

Cavity expansion analysis for brittle materials is presented in Chapter 3. Existing models are reviewed, then simplifying assumptions are introduced to model the cracking and comminution behavior observed in experiments. The static cavity expansion problems in spherical and cylindrical symmetries are solved. Two different methods are employed to solve the dynamic cavity expansion problem in ceramics. The important material parameters determining the penetration resistance are identified and compared with experimental data. The results from cavity expansion analyses of ductile and brittle materials are used to model the penetration into ceramic tiles backed by thick metallic substrates.

In Chapter 4 existing penetration models for rigid and eroding projectiles are reviewed. Strengths and limitations of these models are pointed out. A new approach is hypothesized for modeling penetration by long rod projectiles into metallic targets. The connection between cavity expansion pressure and the target resistance is established in this model. Comparisons with experimental data are presented.

The findings of this research are summarized in Chapter 5. The significant conclusions are presented and scope of future work in this area is indicated.

1.3   History and literature on cavity expansion analyses

Cavity expansion theory has received a great deal of attention for the past few decades. Here I present an overall narrative review of the past work in this area. Technical details for ductile materials are presented in Chapter 2. Similarly, existing cavity expansion analyses for brittle materials are presented in Chapter 3. In Chapter 4, some of the currently used penetration models are discussed.

In the 19th century, Poncelet's equation (see Johnson 1972) was used as a penetration model for rigid penetration into geologic materials like sand and clay. The resistive force was determined to be a function of the square of the penetration velocity plus a constant.

Since World War II, attention has been focused on development of higher velocity impacts that generate stresses high enough to deform and erode the projectile. The highest-velocity penetrator, shaped charge jets, for which one can ignore the strength of the projectile and target materials compared to the high impact pressure generated, can be modeled by a hydrodynamic analysis. Subsequently, the penetration resistance of the target and the strength of the projectile were introduced into the hydrodynamic penetration equation (Tate 1967, 1969; Alekseevskii 1966).

Cavity expansion analysis began in the middle of this century, when Bishop, Hill and Mott (BHM) (1945) derived formulas for the pressure required to open spherical and cylindrical cavities from zero radius in metals. They found that for a deep punching event, the punch pressure is closely bracketed by the spherical and cylindrical cavity expansion pressures. Hill (1946) subsequently derived a formula for dynamic cavity expansion pressure in metals that took inertial effects into account. Hill (1950) suggested that the cavity expansion pressure be considered as the work required to open a cavity of unit volume. He contended further that this energy per unit volume should be a constant irrespective of how the cavity is formed, as long as friction can be neglected. Subsequently, the cavity expansion pressure has been used as an approximation to the penetration resistance of target materials.

Chadwick (1959) solved the spherical cavity expansion problem in a Mohr-Coulomb material. Hopkins (1960) presented an excellent summary of the post World War II work done on static and dynamic cavity expansion. Hunter and Crozier (1967) derived the dynamic cavity expansion pressure for a compressible metal using a similarity transformation under the assumption that the ratio of yield stress to density remains constant. Goodier (1965) successfully applied the cavity expansion results to model linear penetration of hard rigid spheres into soft targets assuming that the dynamic cavity expansion pressure has a sinusoidal variation from the tip to the edge. Hanagud and Ross (1971) used a locking hydrostat assumption in their cavity expansion solution to model target compression for hypervelocity impact of steel projectiles into aluminum targets. Tate (1967, 1969) also discussed the utility of using cavity expansion pressure to represent the target resistance term. Durban and Baruch (1976) numerically solved the non-linear equations for an incremental elastic-plastic material and showed that asymptotic value of expansion pressure exists. Forrestal, Longcope and Norwood (1981) and Forrestal (1986) estimated the force on a conical penetrator in dry porous rock from the cavity expansion pressure, assuming a linear hydrostat and a linear shear-pressure relation. The dynamic cavity expansion

problem in an elastic-plastic solid was solved by Forrestal and Luk (1988) using a similarity transformation. This solution showed that the elastic-plastic boundary speed asymptotically approaches the plastic wave speed in the material and does not indefinitely rise with cavity expansion velocity as was suggested by the incompressible models. Forrestal, Okajima and Luk (1988) then used this solution to model penetration of Aluminum targets by long rod projectiles made of steel. Subsequently, Luk, Forrestal and Amos (1991) developed a dynamic spherical cavity expansion solution for strain-hardening materials. Tzao and Li (1994) calculated the thermal wave profile generated in penetration of metals using the dynamic cavity expansion solution of Forrestal and Luk (1988). Forrestal, Brar and Luk (1991) and Forrestal et al. (1995) have successfully used the cavity expansion solution to model rigid penetration into ductile targets.

Sternberg (1989) discussed the application of cavity expansion pressure to model the strength term in Tate's penetration equation for ceramic targets. Forrestal and Longcope (1990) incorporated tensile cracking into their cavity expansion solution to model a ceramic material as a plastic-cracked-elastic material. Huang, Hutchinson and Travergaard (1991) exploited cavity expansion analysis to characterize the cavitation instabilities in elastic-plastic solids. In an attempt to describe deep penetration of polycarbonate by a cylindrical punch, Wright, Huang and Fleck (1992) modified the cylindrical cavity expansion solution to account for the hackle zone surrounding the penetration channel, with limited success. Florence et al. (1992) derived a solution for the dynamic cavity expansion pressure in brittle ceramics by assuming a constant "flow" stress for the failed material. Partom (1993, 1995, 1996) used cavity expansion analysis for modeling ceramic materials and to describe finite lateral effects in metallic targets. Klopp et al. (1994) conducted spherical cavity expansion experiments in ceramics to study their behavior under impulsive loading situations. Satapathy and Bless (1995) and Bless, Satapathy and Simha (1996) presented static and dynamic cavity expansion theories for ceramic materials. Recently, Forrestal and Tzao (1996) developed a spherical cavity expansion based penetration model for concrete targets.

This dissertation thoroughly reviews the existing cavity expansion theories for both metals and ceramics. These theories are then extended to several cases of practical application for both metals and ceramics. Several examples are cited in which the theoretical results are compared with experimental data. Finally, a new penetration model is hypothesized which shows excellent agreement with several sets of experimental data. The hypothesized material behavior still needs to be experimentally verified.

Chapter 2: Cavity Expansion in Ductile Materials

The cavity expansion pressure required to open a cavity from zero radius in a metal has been shown to provide a good approximation for target resistance properties such as the values of R_t used in Tate-Alekseevskii model (Tate 1967; Anderson et al. 1993) and the penetration resistance properties for rigid body penetration (Goodier 1965; Hanagud and Ross 1971; Forrestal et al. 1995). For an infinite target medium, this pressure is independent of the cavity size and is fully determined by fundamental material properties. Thus it elevates the target resistance term in the Tate-Alekseevskii formulation from quasi-empirical status to being a "first principle" solution. Penetration models are discussed in Chapter 4.

The cavity expansion theory has received the attention of a distinguished group of researchers in the past few decades. In their pioneering work, Bishop, Hill and Mott (1945) derived formulas for spherical and cylindrical cavity expansion pressures in ductile metals and found that these two values closely bracket the deep punching pressure. Hill (1950) later included compressibility in the cavity expansion formula. Chadwick (1959), adopting a slightly different approach, derived a compressible cavity expansion solution which did not vary much from Hill's formula numerically. Chadwick's expression encompassed both metals and soils obeying Mohr-Coulomb type constitutive behavior. Hopkins (1960) presented an excellent summary of the post World War II work in this area. Hunter and Crozier (1967) studied the problem of expansion of a spherical cavity at a constant velocity. Among others, Forrestal's et al. (1988, 1991, 1995) works on dynamic cavity expansion taking into account the compressibility effects are noteworthy. They applied the dynamic cavity expansion analysis to model penetration of metals, rock, and concrete by rigid penetrators. Wright et al. (1992) studied the effect of finite ductility on cavity expansion pressure in an attempt to describe the hackle zone they observed in punch tests of PMMA. Huang et al. (1991) used the cavity expansion solution to study cavitation instability in metals. For penetration mechanics of ductile materials, cavity expansion solutions have been used by Tate (1967, 1986), Goodier (1965), Hanagud and Ross (1971), Forrestal (1988, 1991, 1995), Partom (1996), Rosenberg (1990), Walker and Anderson (1995), and Bless and Lee (1996).

7

In this chapter, the existing literature on spherical and cylindrical cavity expansion analyses are reviewed in some detail (Sections 2.1 and 2.2). The derivations for the quasi-static spherical cavity expansion pressure are shown for various elastic-plastic constitutive behaviors in incompressible and compressible media. The dynamic cavity expansion solution for an elastic-perfectly plastic material is presented for both incompressible and compressible cases. The strain-hardening case is then discussed. The existing cylindrical cavity expansion theory is presented and compared with the spherical cavity expansion theory. During this detailed review, certain new derivations are presented and some of the existing results are analyzed.

Subsequently, the existing theory is modified to account for the presence of a finite boundary. The resulting theory is compared with experimental data. The implications of finite ductility on the spherical cavity expansion analysis are discussed. Such effects are quantified and compared with experimental data. Finally, quasi-static experiments performed on PMMA are described. The predictions from the cavity expansion analysis are compared with experimental data.

2.1 Spherical cavity expansion

2.1.1 Static spherical cavity expansion in an incompressible medium

There are several equivalent derivations of the static spherical cavity expansion solution in the literature (Bishop et al. 1945; Hill 1950; Chadwick 1959; Hopkins 1960; Huang et al. 1991; Luk et al. 1991). Here the most generalized derivation is presented, showing details of all the equations used.

2.1.1.1 Elastic solutions

Consider expansion of a spherical cavity in an infinite elastic-plastic continuum by gradual application of radial pressure on the inner boundary, $r = a_0$. The ensuing deformation is quasi-static. Initially, the state of stress in the medium is elastic. Taking stresses to be positive in tension, for spherical symmetry the equilibrium equation is given by:

$$\frac{d\sigma_r}{dr} + 2\frac{\sigma_r - \sigma_\theta}{r} = 0,$$
(2.1)

8

where σ_r and σ_θ are the radial and hoop stresses, respectively, and r is the radial coordinate. The linear elastic constitutive equation is

$$\sigma_r = (\lambda + 2\mu)\varepsilon_r + 2\lambda\varepsilon_\theta \quad \text{and} \quad \sigma_\theta = \lambda\varepsilon_r + 2(\lambda + \mu)\varepsilon_\theta, \tag{2.2}$$

where λ and μ are the Lamé constants and ε_r and ε_θ are the radial and hoop strains respectively. Assuming small strain theory, in which strains are related to displacement, u, through

$$\varepsilon_r = \frac{du}{dr} \quad \text{and} \quad \varepsilon_\theta = \varepsilon_\phi = \frac{u}{r}, \tag{2.3}$$

where θ and ϕ denote the two equivalent hoop directions, the equilibrium equation reduces to

$$\frac{d^2u}{dr^2} + \frac{2}{r}\frac{du}{dr} - \frac{2u}{r^2} = 0. \tag{2.4}$$

This equation has a solution of the form

$$u = c_1 r + \frac{c_2}{r^2}, \tag{2.5}$$

where c_1 and c_2 are integration constants to be evaluated from the boundary conditions. Since the displacement has to be zero at infinity, c_1 has to be zero. For the other boundary condition, let the pressure applied at the inner boundary be P_0, i.e., $\sigma_r|_{r=a_0} = -P_0$. Evaluating Eqs. (2.2), (2.3), (2.5) and the boundary conditions, one obtains

$$c_2 = \frac{P_0 a_0^3}{4\mu}. \tag{2.6}$$

9

This completes the solution for the elastic field. As the pressure P_0 is increased, the material might become plastic, depending on its yield behavior. For spherical symmetry, von Mises and Tresca yield criteria coincide (Mendelson 1968) and are given by

$$|\sigma_\theta - \sigma_r| = Y, \tag{2.7}$$

where Y is the yield strength. From the elastic solution, the stress difference is given by

$$\sigma_\theta - \sigma_r = \frac{3P_0}{2}\left(\frac{a_0}{r}\right)^3. \tag{2.8}$$

This expression is greatest at the inner boundary. Thus from Eqs. (2.7) and (2.8), the internal pressure required to just yield the material is given by

$$P_0 = \frac{2Y}{3}. \tag{2.9}$$

At this pressure, the elastic strains, which are maximum at the inner surface, are given by

$$\varepsilon_r = -\frac{Y}{3\mu} \text{ and } \varepsilon_\theta = \frac{Y}{6\mu}. \tag{2.10}$$

Since for most metals, $Y \ll \mu$, the assumption of small strain theory for the elastic region is justified. This was originally shown by Chadwick (1959).

2.1.1.2   Elastic-plastic solutions

As the applied pressure is increased beyond the value given by Eq. (2.9), a plastic zone will appear surrounding the cavity (Figure 2.1). A yield function is needed to describe the

10

constitutive behavior of the plastic deformation. Let the effective stress, σ_e, be related to the effective strain, ε, through the following functional relation, which is essentially the uniaxial stress-strain curve:

$$\frac{\sigma_e}{Y} = f(\varepsilon). \tag{2.11}$$
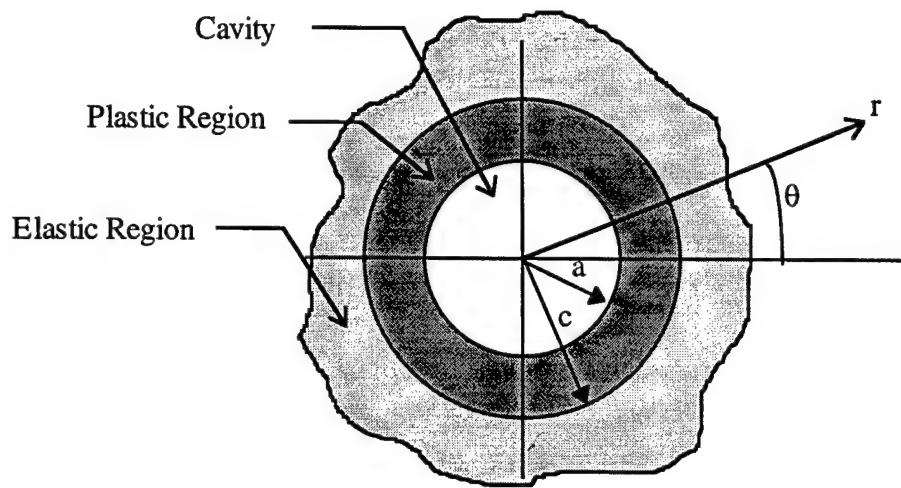
Figure 2.1. Response regions.

For radial loading, the Prandtl-Reuss equations (the associated flow-rule for the von Mises yield criterion) are given by

$$\varepsilon_{ij}^p = \frac{3}{2}\frac{\varepsilon^p}{\sigma_e}S_{ij}, \tag{2.12}$$

where ε_{ij}^p is the plastic part of the strain tensor, ε_{ij}, ε^p is the effective plastic strain and S_{ij} is the stress deviator. The total effective strain ε is the summation of the elastic part, ε^e, and the plastic part ε^p. Using this decomposition, one obtains from Eqs. (2.11) and (2.12)

11

$$\varepsilon_{ij}^p = \frac{3}{2\sigma_e} f^{-1}\left(\frac{\sigma_e}{Y}\right) S_{ij} - \frac{3S_{ij}}{2E}, \tag{2.13}$$

where the elastic relation $\sigma_e = E\varepsilon^e$ has been used. The elastic strain tensor, ε_{ij}^e, is given by

$$
\begin{aligned}
\varepsilon_{ij}^e &= \frac{1+\nu}{E}\sigma_{ij} - \frac{\nu}{E}\sigma_{kk}\delta_{ij} \\
&= \frac{3}{2E}\left[\sigma_{ij} - \frac{1}{3}\sigma_{kk}\delta_{ij}\right] \quad \text{(for incompressibility, } \nu = 0.5\text{)} \\
&= \frac{3}{2E}S_{ij},
\end{aligned} \tag{2.14}
$$

where δ_{ij} is Kronecker delta. Now adding Eqs. (2.13) and (2.14), the total strain tensor becomes

$$\varepsilon_{ij} = \frac{3}{2\sigma_e} f^{-1}\left(\frac{\sigma_e}{Y}\right) S_{ij}. \tag{2.15}$$

This is the same expression derived by Wright et al. (1992). For spherical symmetry, the von Mises yield criterion becomes,

$$\sigma_e = \sqrt{3J_2} = |\sigma_r - \sigma_\theta| = \sigma_\theta - \sigma_r, \tag{2.16}$$

since $\sigma_\theta > \sigma_r$. The term $J_2 = S_{ij}S_{ij}/2$ is the second invariant of the deviatoric stress tensor. Taking either the radial component or the hoop component of Eq. (2.15) and realizing that for an incompressible material, $\varepsilon_r = -2\varepsilon_\theta$, the plastic constitutive equation for the elastic-plastic material becomes

$$f(-\varepsilon_r) = f(2\varepsilon_\theta) = \frac{\sigma_\theta - \sigma_r}{Y}. \tag{2.17}$$

12

Before using Eq. (2.17), one needs to derive an expression for strain so that the functional form of Eq. (2.11) can be used. For the elastic region, the use of small strain theory was shown to be justified. In the plastic region, even though the strain is small near the elastic-plastic boundary, it is not small as one proceeds towards the cavity surface. Thus for the plastic region the use of logarithmic true strain is appropriate. Using the convective differentiation of particle displacement, the particle velocity is

$$v = \frac{\partial u/\partial t}{1 - \partial u/\partial r},$$

(2.18)

Integrating the physical strain rates defined by

$$\dot{\varepsilon}_r = \frac{\partial v}{\partial r} \quad \text{and} \quad \dot{\varepsilon}_\theta = \frac{v}{r},$$

(2.19)

Hopkins (1962) derived the following formulas for logarithmic true strains,

$$\varepsilon_r = -\ln\left(1 - \frac{\partial u}{\partial r}\right), \quad \varepsilon_\theta = -\ln\left(1 - \frac{u}{r}\right).$$

(2.20)

Eq. (2.20) reduces to Eq. (2.3) for small strains. The mass conservation equation in Eulerian coordinates is given by (Forrestal 1990)

$$\frac{d}{dr}(r - u)^3 = 3r^2 \frac{\rho}{\rho_0}.$$

(2.21)

For incompressible material, integration of (2.21) from a to r yields

$$\ln\left(1 - \frac{u}{r}\right) = \frac{1}{3}\ln\left(1 - \frac{a^3 - a_0^3}{r^3}\right).$$

(2.22)

13

Now from Eqs. (2.17), (2.20) and (2.22), one obtains

$$f\left[-\frac{2}{3}\ln\left(1-\frac{a^3-a_0^3}{r^3}\right)\right]=\frac{\sigma_\theta-\sigma_r}{Y}.$$ (2.23)

The location of the elastic-plastic interface, $r = c$, is given by $\sigma_c/Y=f(\varepsilon_y)$, where $\varepsilon_y=Y/E$ is the strain at incipient yield. Thus from Eq. (2.23), the following expression for the relative size of the plastic zone is obtained.

$$\frac{c}{a}=\left[1+\left(\frac{a_0}{c}\right)^3-e^{-3\varepsilon_y/2}\right]^{-1/3}.$$ (2.24)

Eq. (2.24) is plotted in Figure 2.2 for different values of ε_y. It is seen that the plastic zone size relative to the cavity radius rapidly approaches a limiting value. Thus if one were to open a cavity in a continuous medium (i.e., from zero radius), the plastic zone expands in a constant proportion to the current cavity size. On the other hand, the initial cavity size does not matter as long as the final cavity size is larger than about twice its initial value. This situation is akin to an instability, since no matter how much the applied pressure is increased, there will be a limited plastic deformation induced. Hence the material cannot support any pressure higher than that required to deform the material to this limiting cavity size. This pressure, which is independent of the initial cavity size and depends only on the material constants, is called the cavity expansion pressure. Consequently, since the limiting value of the cavity expansion pressure is independent of a/a_0 and only depends on the value of c/a, in the following derivations a_0 is dropped out of the equations. This is true for cases where $a/a_0>2$, or for expansion from zero initial radius. This limiting value also quantifies the extent of plastic region in the penetration model of Walker and Anderson (1995).

14
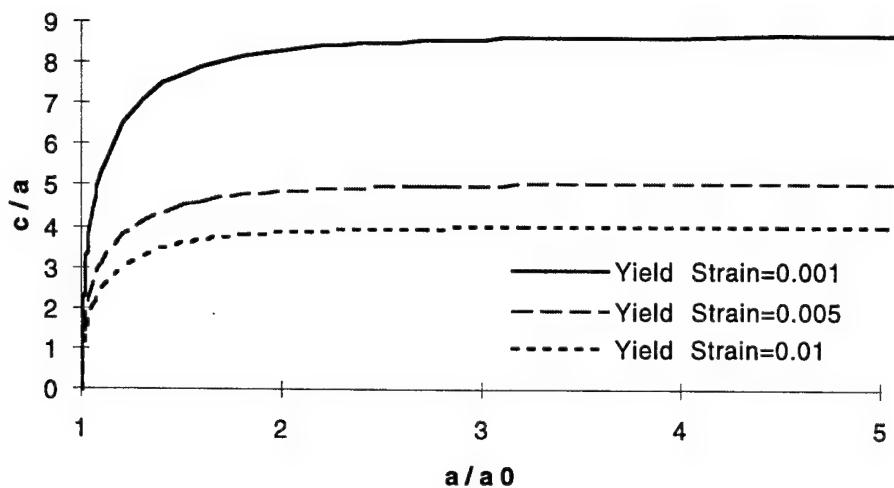
Figure 2.2. Cavity expansion instability.

Now, using Eqs. (2.24), the equilibrium equation (2.1) can be integrated from $r = a$ to ∞. Defining the cavity expansion pressure to be $P_c = -\sigma_r(r = a)$,

$$\frac{P_c}{Y} = 2\int_a^\infty f\left[-\frac{2}{3}\ln\left(1-\frac{a^3}{r^3}\right)\right]\frac{dr}{r}.$$ (2.25)

Introducing a change of variable, $\eta = a/r$, this integral becomes

$$\frac{P_c}{Y} = 2\int_1^\infty f\left[-\frac{2}{3}\ln\left(1-\frac{1}{\eta^3}\right)\right]\frac{d\eta}{\eta}.$$ (2.26)

Introducing one more change of variable, $X = -(2/3)\ln(1-1/\eta^3)$, the cavity expansion pressure is given by

$$\frac{P_c}{Y} = \int_0^\infty \frac{f(X)}{\exp(3X/2)-1}dX.$$ (2.27)

15

Hence, once the stress-strain curve of the material is known, Eq. (2.27) can be integrated to find the cavity expansion pressure, which is about 4 to 5 times the yield strength for metals (shown later). As will be shown in the next few sections, integration of Eq. (2.27) gives a constant value for the cavity expansion pressure purely determined by material constants. Hill (1950) noted that this pressure may be thought of as the work needed to make unit volume of a cavity. The following comment of Hill (1950, page 106) is noteworthy: "The work needed to make unit volume of cavity deep in a medium should not depend greatly on the shape of the indenter or, within broad limits, on the way the cavity is produced, provided friction is negligible." Thus in a penetration situation, where friction can be neglected in comparison to the high levels of dynamic stress operating, cavity expansion pressure does provide a reasonable estimate of the resistance of the target.

2.1.1.3 Elastic-perfectly plastic material

For an elastic-perfectly plastic material, the stress-strain curve is given by

$$\frac{\sigma_e}{Y} = f(\varepsilon) = \frac{\varepsilon}{\varepsilon_y} \qquad \text{for } \varepsilon \leq \varepsilon_y,$$

$$= 1 \qquad \text{for } \varepsilon > \varepsilon_y. \tag{2.28}$$

It was shown in Section 2.1.1.1 that the strains are small in the elastic region. Thus for the elastic part, $e^{3x/2} - 1 \cong 3x/2$. Substitution of Eq. (2.28) into Eq. (2.27) and integration yields

$$\frac{P_c}{Y} = \frac{2}{3} + \int_{\varepsilon_y}^{\infty} \frac{dX}{\exp{(3x/2)} - 1}$$

$$= \frac{2}{3}\left[1 - \ln\left(1 - \exp(-3\varepsilon_y/2)\right)\right]. \tag{2.29}$$

For small values of ε_y (for typical metals $\varepsilon_y \sim 0.01$), Eq. (2.29) reduces to

$$\frac{P_c}{Y} = \frac{2}{3}\left[1 + \ln\left(\frac{2E}{3Y}\right)\right]. \tag{2.30}$$

16

This is the same as the spherical cavity expansion pressure for incompressible material originally derived by Bishop et al. (1945).

2.1.1.4 Material showing strain hardening

Hopkins (1960) has pointed out that under a general condition of work hardening, numerical solution of the ensuing non-linear equations is unavoidable. For certain simple cases, analytical expressions have been found. Consider, for example, a linear strain hardening law of the type

$$\frac{\sigma_e}{Y} = f(\varepsilon) = \frac{\varepsilon}{\varepsilon_y} \qquad \text{for } \varepsilon \leq \varepsilon_y$$

$$= 1 + A\varepsilon \qquad \text{for } \varepsilon > \varepsilon_y. \tag{2.31}$$

Exact evaluation of the integral in Eq. (2.27) needs numerical solution. However, Bishop et al. (1945) showed that if $(a/c)^3$ can be ignored compared to unity, the strain hardening term is given by $2A\pi^2/27Y$ in addition to the non-strain hardening term of Eq. (2.30). For a power hardening material of the type

$$\frac{\sigma_e}{Y} = f(\varepsilon) = \frac{\varepsilon}{\varepsilon_y} \qquad \text{for } \varepsilon \leq \varepsilon_y$$

$$= \left(\frac{\varepsilon}{\varepsilon_y}\right)^n \qquad \text{for } \varepsilon > \varepsilon_y, \tag{2.32}$$

For small values of ε_y, integration of Eq. (2.27) yields

$$\frac{P_c}{Y} = \frac{2}{3} + \int_{\varepsilon_y}^{\infty} \frac{\left(X/\varepsilon_y\right)^n}{e^{3X/2} - 1} dX$$

$$= \frac{2}{3} + \frac{2}{3}\left(\frac{2E}{3Y}\right)^n \int_{1+3\varepsilon_y/2}^{\infty} \frac{(\ln\xi)^n}{\xi(\xi-1)} d\xi; \text{ where } \xi = \exp(3X/2)$$

17

$$= \frac{2}{3}\left[1+\left(\frac{2E}{3Y}\right)^{n}\int_{0}^{1-\frac{3Y}{2E}}\frac{(-\ln\chi)^{n}}{1-\chi}d\chi\right]; \text{ where } \chi=1/\xi. \tag{2.33}$$

Luk et al. (1991) arrived at the same expression as in Eq. (2.33) by using a similarity transformation method. For a given strain hardening coefficient n, the integral in Eq. (2.33) must be numerically evaluated. Huang et al. (1991) also presented graphically the cavity expansion pressure for a strain hardening material by numerically evaluating the equations involved.

For practical applications, the work hardening is usually ignored, since the contribution of the work-hardening part is small. For example, Bishop et al. (1945) found that for copper, work hardening contributed about 5% of the total cavity expansion pressure. On the other hand, as discussed in Chapter 4, at very high strain rates arising from hyper-velocity penetration, the typical target materials behave mostly in an elastic-perfectly plastic manner. Effect of finite ductility of hard metals would further reduce the effect of work hardening.

2.1.2 Static spherical cavity expansion in a compressible material

2.1.2.1 Elastic-perfectly plastic material

For an elastic-perfectly plastic material, evaluation of the field equations are straightforward. Recognizing that $|\sigma_r - \sigma_\theta| = Y$ for this case in the plastic region, integration of the equilibrium equation 2.1 yields

$$\sigma_r = 2Y\ln(r) + B. \tag{2.34}$$

Evaluation of the integration constant B is effected from the continuity of stress at the elastic-plastic boundary, r = c. At this boundary, the radial stress is 2Y/3 from Eq. (2.9). Thus using this boundary condition and evaluating Eq. (2.34) at r = a, one obtains

$$P_c = \frac{2Y}{3} + 2Y\ln\left(\frac{c}{a}\right). \tag{2.35}$$

18

From the elastic solution of Section 2.1.1, using Equations (2.5), (2.6) and (2.9) and with the understanding that the elastic-plastic interface is at $r = c$ (thus a_0 in Eq. 2.6 is replaced by c), the displacement at the interface is given by

$$\frac{u(c)}{c} = \frac{Y}{6\mu}. \tag{2.36}$$

If one ignored the compressibility effect in the plastic region, conservation of volume dictates that

$$[c-u(c)]^3 = c^3 - a^3 , \tag{2.37}$$

for a cavity opening from zero radius. Neglecting higher order terms in $u(c)/c$ (which is good for $Y \ll \mu$, as seen from Eq. 2.36), one gets

$$u(c) / c = (a/c)^3 / 3. \tag{2.38}$$

Equating this with Eq. (2.36), the relative size of the plastic zone is

$$c/a = (2\mu/Y)^{1/3}. \tag{2.39}$$

Finally, insertion of Eq. (2.39) into Eq. (2.35) results in the following expression for cavity expansion pressure:

$$P_c = \frac{2Y}{3}\left[1 + \ln\left(\frac{2\mu}{Y}\right)\right]. \tag{2.40}$$

For $\nu = 0.5$, Eq. (2.40) reduces to the incompressible solution, Eq. (2.30). Thus, ignoring compressibility in the plastic region only, c/a is thus calculated using volume conservation in that region. This was derived by Bishop et al. (1945). If the compressibility effect of the plastic region needs to be accounted for, the situation is slightly complicated. Hill (1950) and Hopkins (1960) adopted an innovative procedure. Taking the movement of plastic boundary as a scale of time, integration of the mass conservation equation yielded a formula for cavity expansion in a compressible elastic-plastic material. Hill (1950) suggested that the same result can be arrived at

19

by directly using the compressibility equation in the integrated form. I adopt the latter approach, which is considerably simpler than the former. The mass conservation equation can be written as

$$\frac{\rho_0}{\rho} = \frac{1}{3r^2}\frac{d}{dr}(u+r)^3.$$ (2.41)

Using the linear equation of state, $\rho_0/\rho = 1 - P/K$, where P is the hydrostatic pressure given by $P = -(\sigma_r + 2\sigma_\theta)/3$, and the von Mises yield criterion, $|\sigma_r - \sigma_\theta| = Y$, one obtains from Eq. (2.41),

$$-\frac{1}{3}(3\sigma_r + 2Y) = K\left[1 - \frac{1}{3r^2}\frac{d}{dr}(u+r)^3\right].$$ (2.42)

The stress σ_r is given by Eq. (2.34) and the boundary condition in the following paragraph. Integrating this equation from the Lagrangian positions $R = 0$ to $R = c - u(c)$ and ignoring higher order terms of $u(c)/c$ (in view of Eq. (2.36) for $Y \ll \mu$), I obtain the following expression for plastic zone size:

$$\frac{c}{a} = \left[\frac{E}{3Y(1-\nu)}\right]^{1/3}.$$ (2.43)

Substitution of Eq. (2.43) into Eq. (2.35) yields the following formula for compressible cavity expansion pressure, which is identical to the formula derived by Hill (1950):

$$P_c = \frac{2Y}{3}\left[1 + \ln\left(\frac{E}{3Y(1-\nu)}\right)\right].$$ (2.44)

Here the fact that $Y \ll \mu$ was used several times. For $\nu = 0.5$, Eq. (2.44) becomes identical to the incompressible solution, Eq. (2.30). Huang et al. (1991) also arrived at this formula by adopting a somewhat different approach, and showed that this is the cavitation limit, i.e., the material cannot support any higher pressure than this. Evaluation of the plastic zone size from Eqs. (2.24) and (2.43) for typical steels ($E = 206$ GPa, $Y = 1$ GPa, $\nu = 0.3$) indicates that the incompressible solution ($c/a = 5.16$) overpredicts the compressible solution ($c/a = 4.6$) by about 12%.

20

Similarly, evaluation of Eqs. (2.30) and (2.44) indicate that incompressible solution for cavity expansion pressure ($P_c = 3.95$ GPa) overpredicts the compressible solution ($P_c = 3.7$ GPa) by about 7%. On the other hand, BHM's partial compressible solution (Eqs. 2.39 and 2.40) overpredicts the plastic zone size and the cavity expansion pressure by about 17% and 10% respectively, compared to the fully compressible solution (Eqs. 2.43 and 2.44).

2.1.2.2   Strain hardening material

Both Hill (1950) and Hopkins (1960) pointed out the difficulties in obtaining the cavity expansion solution for a compressible strain hardening material. For general strain hardening, numerical integration by using incremental steps on the non-linear stress-strain curve is unavoidable. Thus they assumed incompressibility in deriving formulas for a strain hardening material, as discussed in Section 2.1.1. Later Luk et al. (1991) used a similarity transformation to solve the non-linear field equations and numerically evaluated the resulting differential equations. From their result, it is found that for quasi-static expansion, the compressible model predicts a slightly lower cavity expansion pressure than the incompressible model. The difference increased for the dynamic case with increasing cavity expansion velocity.

2.1.3   Dynamic cavity expansion in an incompressible material

So far, the cavity expansion solution for quasi-static expansion ignoring inertial effects, has been considered for different material behaviors. As discussed by Hopkins (1960), Hill was the first to derive the dynamic cavity expansion solution for an incompressible ductile material. Here this solution is presented briefly.

The equation of motion, written in spherical coordinates, is

$$\frac{\partial \sigma_r}{\partial r} + \frac{2}{r}\left(\sigma_r - \sigma_\theta\right) = \rho\left(\frac{\partial v}{\partial t} + v\frac{\partial v}{\partial r}\right).$$

(2.45)

The equation of conservation of mass is

$$\frac{1}{r^2}\frac{\partial}{\partial r}\left(\rho r^2 v\right) + \frac{\partial \rho}{\partial t} = 0.$$

(2.46)

21

For an incompressible material ρ = constant, and thus equation (2.46) becomes $\dfrac{\partial}{\partial r}\left(r^2 v\right) = 0$.

Integration of this equation with the boundary condition $v(a) = \dot{a}$ reveals that the particle velocity in the incompressible region is determined by

$$v = \frac{a^2 \dot{a}}{r^2}.$$ (2.47)

Insertion of Eq. (2.47) into Eq. (2.45), along with the yield condition $|\sigma_r - \sigma_\theta| = Y$ and subsequent integration yields

$$\sigma_r = 2Y\ln r - \rho\left[\frac{a^2\ddot{a} + 2a\dot{a}^2}{r} - \frac{a^4\dot{a}^2}{2r^4}\right] + g(t),$$ (2.48)

where $g(t)$ is an arbitrary function, which can be determined from the boundary condition at the elastic-plastic interface. Substitution of Eq. (2.47) into the strain rate definition given in Eq. (2.19) and subsequent integration between limits $r = a_0$ at $t = 0$ to $r = a$ at $t = t$ results in the following expressions for the strains in the incompressible medium:

$$\varepsilon_r = \frac{-2(a^3 - a_0^3)}{3r^3} \quad \text{and} \quad \varepsilon_\theta = \frac{(a^3 - a_0^3)}{3r^3}.$$ (2.49)

Finally, substitution of Eq. (2.49) into the elastic constitutive equation (2.2) and use of the yield criterion $|\sigma_r - \sigma_\theta| = Y$ results in the relative location of the plastic front as

$$\frac{c(t)}{a(t)} = \left(\frac{2\mu}{Y}\right)^{1/3} = \left[\frac{E}{(1+\upsilon)Y}\right].$$ (2.50)

Thus, evaluation of Eq. (2.45) results in the following behavior of the radial stress in the elastic region:

$$\sigma_r = -\frac{2Y}{3}\frac{c^3}{r^3} - \rho\left[\frac{a^2\ddot{a} + 2a\dot{a}^2}{r} - \frac{a^4\dot{a}^2}{2r^4}\right] \text{ for } r > c.$$ (2.51)

22

Here the fact that the material is at the yield point on the elastic-plastic interface has been used. Finally, using the continuity of the radial stress at the elastic-plastic interface, the following formula follows from Eqs. (2.48), (2.50) and (2.51):

$$P_c = \frac{2Y}{3}\left[1 + \ln\frac{2E}{3Y}\right] + \rho\left(a\ddot{a} + \frac{3}{2}\dot{a}^2\right). \tag{2.52}$$

The first term on the right-hand side is the quasi-static term derived in Eq. (2.30) for an incompressible elastic-perfectly plastic material.

2.1.4 Dynamic cavity expansion in a compressible material

Even though the incompressibility assumption resulted in an analytically tractable dynamic cavity expansion solution, there are certain limitations that were pointed out by Chadwick et al. (1964) and Hunter and Crozier (1967). For an incompressible material, the elastic wave speed is infinite. The plastic wave speed, which bears a constant ratio to the cavity expansion speed (Eq. 2.50), can increase indefinitely for high enough cavity expansion speed. They also criticized the instantaneous transmission of energy and failure to describe the shock discontinuity arising *a priori* due to the velocity field in Eq. (2.47). The assumption of a single plastic zone is valid only for $\dot{a} \geq 0$. However, this is usually true for penetration problems.

Hunter and Crozier (1967) noted that for the case where the cavity is expanded at a constant speed, i.e., $a = V_0 t$, the problem admits a similarity solution in which stress, velocity and density depend on a single similarity variable, $\eta = rt^{-1}$. Further, they assumed that throughout the cavity expansion process, the ratio of the yield stress to the density is constant. Their solution admitted a shock discontinuity for cases where the elastic-plastic boundary speed was in excess of $c_p = \leq \sqrt{(K/\rho)}$. Their solution showed that with increasing cavity expansion velocity, the elastic-plastic interface speed increases and ultimately reaches the elastic wave speed. Hopkins (1960) gave a detailed exposition of the nature of the plastic wave propagation in spherical symmetry. He recognized that a part of the plastic displacement can be derived from a plastic displacement potential function arising out of irrotational motion. This part *necessarily* travels at the plastic wave speed c_p, whereas the rest of the displacement does not satisfy the wave equation and hence nothing can be said about its speed. Thus he pointed out that the elastic-plastic boundary does not

23

necessarily travel at the plastic wave speed c_p. On the other hand, a later solution of Forrestal and Luk (1988) has shown that the elastic-plastic interface speed asymptotically approaches the plastic wave speed.

Forrestal and Luk (1988) presented a solution for expansion of a spherical cavity at a constant velocity. As pointed out earlier, this situation admits a self-similar solution[1] by a similarity transformation. For spherical symmetry, introduction of a similarity variable, $\xi = r/ct$, where c is the elastic-plastic interface speed, reduces the coupled partial differential equations to a set of coupled ordinary differential equations.

Unlike Hunter and Crozier, Forrestal and Luk did not envisage a shock discontinuity at the elastic-plastic interface. Rather, using the Hugoniot jump condition along with the condition that the material is about to yield on either side of the elastic-plastic interface, they determined that particle velocity, stresses and the density are continuous across the elastic-plastic boundary. They assumed a linear hydrostat for the plastic region. Using the following non-dimensional variables,

$$S = \sigma_r / K; \quad T = Y/K; \quad U = v/c; \quad \varepsilon = V/c; \quad \beta = c/c_p, \tag{2.53}$$

where $c_p = \sqrt{(E/\rho_0)}$, c is the elastic-plastic interface speed, and V is the constant cavity expansion speed, they derived the following approximate solution for the dynamic cavity expansion pressure:

$$
\begin{aligned}
S_c = S_2 &- \frac{\beta^2\left(\varepsilon^2 - U_2^2\right)}{2} + \frac{2\left(U_2\beta^2 + T\right)(1-\varepsilon)}{\varepsilon\left(1-\beta^2\right)} \\
&- 2T\ln\varepsilon + T\ln\left(\frac{1-\beta^2\varepsilon^2}{1-\beta^2}\right) + \frac{T}{\beta\varepsilon}\ln\left[\frac{\left(1+\beta^2\varepsilon\right)(1-\beta)}{\left(1-\beta^2\varepsilon\right)(1+\beta)}\right],
\end{aligned}
\tag{2.54}
$$

where S_2 and U_2 are obtained from evaluation of the elastic solution at the elastic-plastic boundary, and are given by

$$U_2 = \frac{T(1+\nu)}{3(1-2\nu)} \quad \text{and} \quad S_2 = \frac{2T}{3}\left[1 + \frac{(1+\nu)\alpha^2}{(1-2\nu)(1+\alpha)}\right], \tag{2.55}$$

---

[1] An excellent exposition on self-similar solutions and similarity transformations is given by Barenblatt (1979).

where $\alpha = c/c_d$ with $c_d{}^2 = E(1-\nu) / [(1+\nu)(1-2\nu)\rho_0]$.

To evaluate Eq. (2.54), the velocity of the elastic-plastic interface, c, has to be calculated first. From the condition that the cavity opens from zero initial radius, they obtained the following transcendental equation, whose root yields the interfacial velocity:

$$T\beta\varepsilon + \beta^3\varepsilon^3 - \frac{\beta\left(U_2\beta^2 + T\right)\left(1 - \beta^2\varepsilon^2\right)}{\left(1 - \beta^2\right)} - \frac{T\left(1 - \beta^2\varepsilon^2\right)}{2}\ln\left[\frac{(1 + \beta\varepsilon)(1 - \beta)}{(1 - \beta\varepsilon)(1 + \beta)}\right] = 0. \qquad (2.56)$$

Forrestal and Luk presented numerical solutions of Eqs. (2.54) and (2.56) and compared them with the full non-linear solution of the field equations. The approximate solutions were shown to be in excellent agreement with the full non-linear solution. The important aspect of their solution was that the elastic-plastic interface velocity asymptotically approached the plastic wave speed, c_p. As expected, the compressible solution predicted a lower value of dynamic cavity expansion pressure compared to the incompressible solution, while agreeing with the latter and the quasi-static solution (Eq. 2.44) for zero cavity expansion velocity. The effect of compressibility increased with expansion velocity. In a later paper, Forrestal et al. (1988) described the compressible dynamic cavity expansion pressure by the following curve-fit formula:

$$P_c(u) = P_{stat} + 1.041\rho u^2, \qquad (2.57)$$

where P_{stat} is the quasi-static term given by Eq. (2.44).

In Figure 2.3 I have plotted the dynamic cavity expansion solution from Eqs. (2.54) and (2.57) for steel together with the incompressible solution of Eq. (2.52). It is seen from this figure that even though Eq. (2.57) represents the compressible solution, Eq. (2.54), quite well for a velocity below about 1200 m/s, it diverges significantly from the former at higher velocities. Use of the full solution of Eq. (2.54) results in a significant drop in the inertial term with velocity (compared to the curvefit formula, Eq. 2.57), which will be shown in Chapter 4 to be in good agreement with the experimental data.
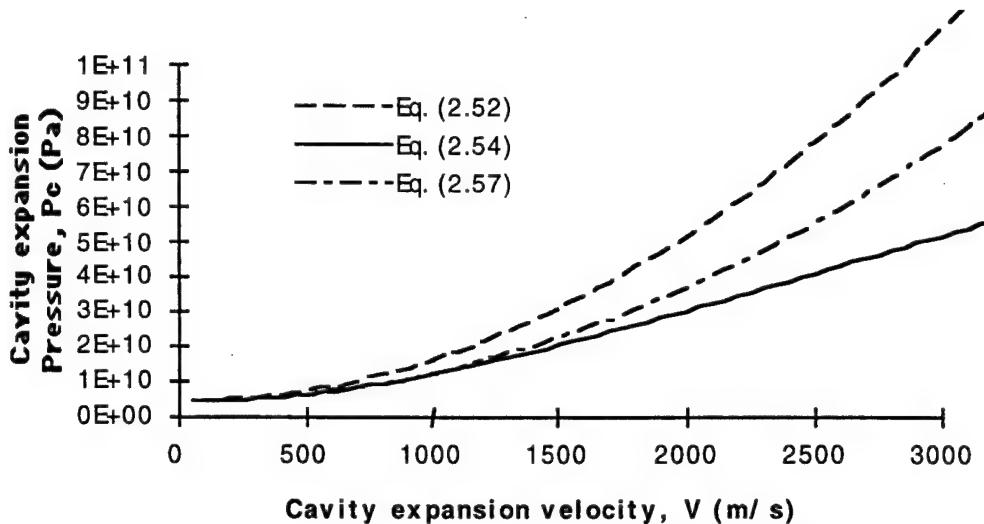
Figure 2.3. Dynamic cavity expansion pressure.

Recently, Warren and Forrestal (1997) derived the dynamic cavity expansion solution for aluminum targets taking into account the effects of compressibility, strain hardening and strain-rate sensitivity. This model explained the rigid penetration into aluminum targets quite well.

2.2   Cylindrical cavity expansion theory

The solution for cylindrical cavity expansion is more difficult than that for the spherical case, since this is a two dimensional problem as compared to the one dimensional spherical cavity problem. The cylindrical cavity problem requires some assumption about the longitudinal strain or the longitudinal stress. Hill (1950) has discussed this problem in length. For the spherical case, the von Mises and the Tresca yield criteria are the same. This is not true for the cylindrical case, and hence the choice of yield condition affects the solution. For cylindrical symmetry, the equilibrium equation is,

$$\frac{d\sigma_r}{dr} + \frac{\sigma_r - \sigma_\theta}{r} = 0. \tag{2.58}$$

Eq. (2.15) was derived from the Prandtl-Reuss equation, which is the associated flow rule for von Mises yield condition (Mendelson, 1968). Thus Eq. (2.15) cannot be used for the Tresca yield condition. However, for an elastic-perfectly plastic material, the yield condition is,

$$|\sigma_r - \sigma_\theta| = \beta Y, \tag{2.59}$$

26

where $\beta = 1$ for the Tresca and $\beta = 2/\sqrt{3}$ for the von Mises criterion. Integration of Eq. (2.58) with the elastic constitutive equation for the elastic region and with Eq. (2.59) for the plastic region, and satisfaction of the boundary conditions that the stress and displacements are continuous at the elastic-plastic boundary and that the cavity opens from zero initial radius, gives the expression for cavity expansion pressure. Assuming an incompressible plastic region and the von Mises yield condition, Bishop et al. (1945) derived the following formula for the cavity expansion pressure:

$$P_c = \frac{Y}{\sqrt{3}} \left[1 + \ln\left(\frac{\sqrt{3}E}{2(1+v)Y} \right) \right]. \tag{2.60}$$

For a compressible plastic zone, Hill (1950) derived the following formula:

$$P_c = \frac{\beta Y}{2} \left[1 + \ln\left(\frac{2E}{(5-4v)\beta Y} \right) \right]. \tag{2.61}$$

Here β takes the appropriate value for Tresca or von Mises yield criterion. For the von Mises criterion and an incompressible material ($v = 0.5$), Eq. (2.60) and (2.61) are identical. For an incompressible strain hardening material with the stress-strain curve of the form given by Eq. 2.31), the cavity expansion pressure is given by (Hill 1950)

$$P_c = \frac{Y}{\sqrt{3}} \left[1 + \ln\left(\frac{E}{\sqrt{3}Y} \right) \right] + \frac{\pi^2 A}{18}. \tag{2.62}$$

The dynamic cavity expansion problem for cylindrical symmetry has not been studied extensively. The only published work in this area appears to be that due to Forrestal (1986), where for application in the area of penetration in dry porous rock, he derived an approximate solution for dynamic cylindrical cavity expansion. In a later paper, Forrestal et al. (1988) presented the following curve-fit formula for this numerical solution:

$$P_c = \frac{Y}{2} \left[1 + \ln\left(\frac{2E}{(5-4v)Y} \right) \right] + 1.837 \rho V^2. \tag{2.63}$$

where V is the constant cavity expansion velocity.

A generalized dynamic cavity expansion analysis in cylindrical coordinates for cavities with arbitrary cross-sections (including cylindrical) is the subject of a current doctoral dissertation (Woo 1997).

2.3   Spherical vs. cylindrical cavity expansion

From the above description of the cavity expansion in spherical and cylindrical symmetry, it turns out that for commonly used metals, the quasi-static cavity expansion pressures differ by only about 15% (e.g., for steel with $E = 206$ GPa, $Y = 1$ GPa and $v = 0.3$, Eqs. 2.44 and 2.61 yield $P_c = 3.7$ GPa and 3.2 GPa respectively). Bishop et al.'s (1945) deep punching experiment into copper showed that the punch pressure was bracketed by the spherical and cylindrical cavity expansion pressure. Additionally, as described in Section 2.1.2, Hill (1950) contended that the spherical cavity expansion pressure may be thought of as the work needed to make a unit volume of cavity, which should not depend on how the cavity is formed. All this lead to the use of cavity expansion pressure as a good approximation of the target resistance even at high penetration velocities.

Researchers have used both the spherical cavity expansion theory (Tate 1967; Goodier 1965; Hanagud and Ross 1971; Forrestal et al. 1988) and the cylindrical cavity expansion theory (Wright et al. 1992; Rosenberg 1990) in penetration applications. Forrestal et al. (1988) found that for rigid penetration into aluminum targets, both cavity expansion theories gave close enough agreement with data. For this case, their figures showed that the experimental data had a somewhat better agreement with spherical cavity expansion solution. Hydrocode simulations of hypervelocity penetration (Walker and Anderson 1995) also indicates a spherical quality of the stress and velocity distributions ahead of the tip of the penetrator. Partom (1996) observed that application of a spherical cavity expansion model for understanding the degradation of target resistance in partially confined targets yields a better agreement with hydrocode simulations compared to a cylindrical cavity expansion solution. Forrestal and Luk's (1992) spherical cavity expansion solution for soil penetration compared well with field test data. Forrestal and Tzao (1996) noted that a cylindrical cavity expansion solution overpredicts the early time deceleration and underpredicts the later deceleration response for penetration into dry porous rock. On the other

hand, they noted that the spherical cavity expansion approximation (Forrestal and Luk 1992) is in reasonably good agreement for the entire deceleration response. I shall show in the next chapter that the spherical cavity expansion pressure provides a better approximation of penetration resistance of ceramics as compared to cylindrical cavity expansion pressure. On the other hand, as described at the end of this chapter, quasi-static punch experiments in PMMA agreed better with the cylindrical cavity expansion solution after the punch was fully embedded.

In view of the above discussion, it appears that the spherical cavity expansion solution is preferable for applications involving high velocity penetration. For cases where the penetrator is in contact with the target, e.g., in static punching, the cylindrical cavity expansion solution is preferable. Also, for yawed penetration (Bless and Satapathy 1997), the calculation of the trajectory of the penetrator in the slot cutting mode warrants use of the cylindrical cavity expansion solution since the penetrator is in contact with the target, and the deformation is plane strain.

2.4 Effects of finite ductility on cavity expansion pressure

In dealing with the plastic yielding of metals, it is usually assumed that once the material yields, it can plastically deform indefinitely. Thus an elastic-perfectly plastic material can support any amount of straining at the constant yield stress. However, both quasi-static and high-strain rate experiments show that there is a finite ductility associated with any metal, i.e., it fails at some finite strain. There seems to be little research on this aspect of material behavior, perhaps due to the difficulties in interpreting the experimental data. For tensile testing, the specimen necks and is subjected to a three dimensional (3D) state of stress at the neck. But the very fact that the material develops necking at a specific strain, points to the existence of a failure strain limit. What happens after this point can be explained using 3D stress analysis (Rajendran and Bless 1986). Similar finite failure strains are observable in compression testing as well, where necking is absent. In a compressive stress field, failure may occur due to localization effects, e.g., shear banding. In torsion tests the specimen fails by adiabatic shear banding. The observation of a specific strain at which this form of failure is initiated, points to the existence of a finite failure strain in this case as well.

29

Effects of finite ductility in a compressive 3D stress situation are not clear. Firstly, hydrostatic pressure increases ductility. Thus the failure strain value has to be corrected from its one-dimensional value appropriately. The effect of hydrostatic pressure on ductility has been studied for quasi-static cases (Rice and Tracy 1969; McClintock 1968; Hancock and Mackenzie 1976). No such studies appear in the literature for cases involving high strain rates experienced in penetration situations. Secondly, what happens to the material behavior beyond the failure strain is not clear either. In a one-dimensional experiment, the effective strength drops to zero because the specimen breaks. A direct extension to a 3D case would mean that the material cannot support any shear and thus will behave in a hydrodynamic fashion, capable of supporting only compressive pressure. On the other hand, if effective strain is taken as a failure criteria, cracks may appear in certain preferred directions. Wright et al. (1992) took this as the explanation for the appearance of a hackle zone in cylindrical symmetry, in which material was supposed to have cracked in the radial direction. In analogy, for spherical symmetry, either the material could crack simultaneously in both the equivalent hoop directions or could crack in either one of the hoop directions. If the cracks appear in either one of the hoop directions then the spherical symmetry is lost and the analysis becomes extremely complicated. In the following discussion, I consider the case where radial symmetry is preserved due to appearance of cracks in both hoop directions and the case where the material looses all its shear strength upon attaining the failure strain. This analysis addresses an important practical problem due to current interest in high strength steels and titanium as penetration barriers. These materials are prone to shear localization leading to cracking in a compressive stress field.

Consider an incompressible elastic-perfectly plastic material. Figure 2.4 shows the response regions in the material. Surrounding the cavity there is a failed zone where the strain has exceeded the failure strain. Beyond the failed zone, is a plastic zone, which is surrounded by an elastic region. For an incompressible material, Eq. (2.23) related the equivalent stress with the stress-strain curve for spherical symmetry. At the failed-plastic boundary, $r = b$, the function f of Eq. (2.11) is

$$f(\varepsilon_f) = \sigma_e/Y, \tag{2.64}$$

where ε_f is the failure strain. Thus taking a_0 as zero in Eq. (2.24), the following expression for the size of the failed region is obtained:

$$\frac{b}{a} = \left[1 - \exp\left(-\frac{3\varepsilon_f}{2} \right) \right]^{-1/3}. \qquad (2.65)$$

For comparison, Wright et al.'s (1992) formula for the case of cylindrical symmetry is

$$\left(\frac{b}{a} \right)_{cyl} = \left[1 - \exp\left(-\sqrt{3}\varepsilon_f \right) \right]^{-1/2}. \qquad (2.66)$$
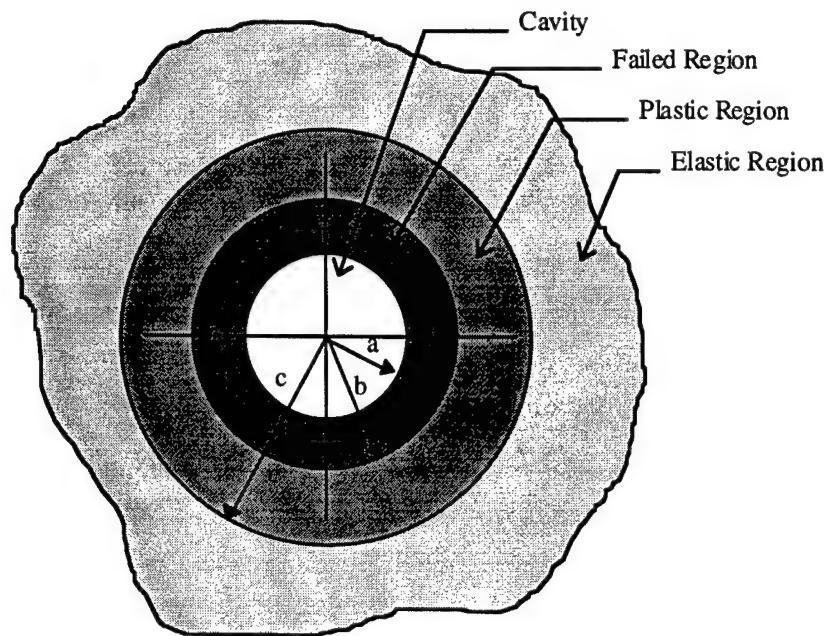
Figure 2.4. Material response regions with a failure zone, in spherical symmetry.

Eqs. (2.65) and (2.66) are plotted in Figure 2.5 for a range of ε_f. The size of the cracked region decreases with increasing failure strain value. As expected, for an infinitely ductile material (i.e., $\varepsilon_f = \infty$), the cracked region disappears.

31
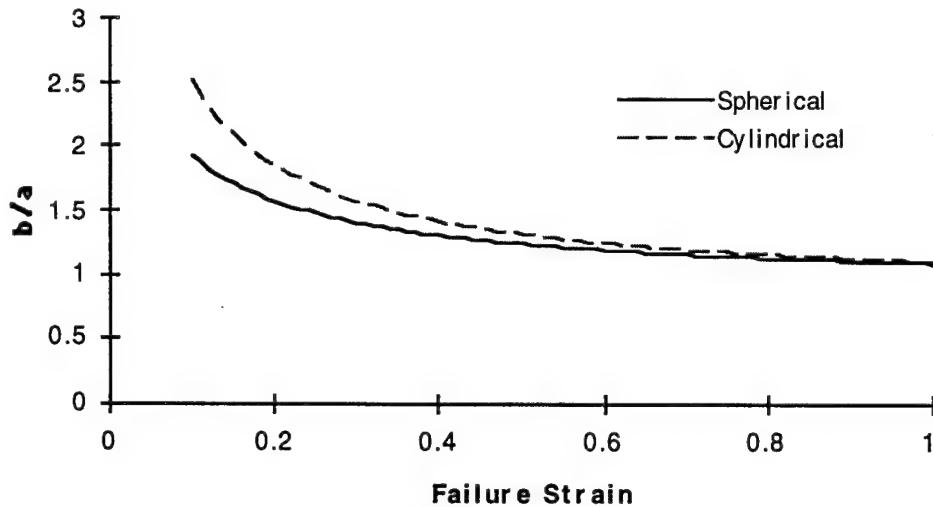
Figure 2.5. Size of the failed zone vs. failure strain.

Case-a: Spherically symmetric radial cracks (needle cracks)

If it is assumed that upon attainment of failure strain, radial cracks appear, then

$$\sigma_\theta = \sigma_\phi = 0 \quad \text{for } a < r < b. \tag{2.67}$$

Thus inserting Eq. (2.67) into the equilibrium equation, Eq. (2.1) and integrating from $r = a$ to $r = b$, one obtains

$$P_c = -\sigma_r\big|_{r=a} = -\sigma_r\big|_{r=b} \frac{b^2}{a^2}. \tag{2.68}$$

$\sigma_r(r = b)$ is obtained by integrating the equilibrium equation, Eq. (2.1) with the plastic constitutive equation, Eq. (2.23) with $a_0 = 0$. Thus,

$$\sigma_r(r = b) = -2\int_b^\infty f\left[-\frac{2}{3}\left(1 - \frac{a^3}{r^3}\right)\right]\frac{dr}{r}$$

$$= -2\int_{b/a}^\infty f\left[-\frac{2}{3}\ln\left(1 - \frac{1}{\eta^3}\right)\right]\frac{d\eta}{\eta} \quad \text{where } \eta = r/a$$

32

$$= -\int_0^{\varepsilon_f} \frac{f(X)}{\exp(3X/2)-1} dX, \qquad \text{where } X = -(2/3)\ln(1-1/\eta^3). \qquad (2.69)$$

Eq. (2.65) was used to change the upper limit of the integral in the last equality of Eq. (2.69). From Eqs. (2.65), (2.68) and (2.69), the cavity expansion pressure is given by

$$P_c = \left[1 - \exp(-3\varepsilon_f/2)\right]^{-2/3} \int_0^{\varepsilon_f} \frac{f(X)}{\exp(3X/2)-1} dX. \qquad (2.70)$$

Note that Eq. (2.70) reduces to Eq. (2.27) for the infinite ductility case, i.e., when $\varepsilon_f \rightarrow \infty$.

Case-b: Loss of shear strength.

In this case the material in the failed zone behaves in a hydrodynamic fashion, capable of supporting only hydrostatic compression with zero shear strength. Taking $\sigma_e = \sigma_\theta - \sigma_r = 0$ in the failed region, one deduces from the equilibrium equation, Eq. (2.1), that the radial stress is constant in this region. Thus from Eq. (2.69), the cavity expansion pressure is given by

$$P_c = -\sigma_r(r=b) = \int_0^{\varepsilon_f} \frac{f(X)}{\exp(3X/2)-1} dX. \qquad (2.71)$$

For $\varepsilon_f \rightarrow \infty$, Eq. (2.71) reduces to Eq. (2.27).

Example:

Bless et al. (1996) conducted penetration experiments into Ti6Al4V alloys. The elastic constants for these alloys are calculated from Steinberg's (1991) database as: E = 112.22 GPa, ν = 0.34. Macdougall and Harding (1996) reported a constant shear yield strength of about 0.675 GPa at a strain rate of 1000/s. The shear failure strain in their shear experiment was about 0.4. For the von Mises criterion, the yield strength is 1.17 GPa (yield strength=$\sqrt{3}$*shear strength). The failure strain, ε_f, is 0.2. Use of Eq. (2.44) for a compressible material with infinite ductility gives a cavity expansion pressure, P_c = 3.25Y. Bless et al. observed that the penetration

33

resistance of this material decreases from about 4.5Y to 3.5Y for impact velocities varying from 1.5 km/s to 2.3 km/s. This is the same trend that the cracked-failed zone model (case a) shows in Figure 2.6, if one assumes that the failure strain increases with impact velocity due to increase in hydrostatic pressure. On the other hand, case-b (loss of shear strength) indicates that the cavity expansion pressure increases from 2.5Y to 3.25Y as the failure strain increases. Thus the cracked-failed zone model (case-a) is in better agreement with the experimental observations.
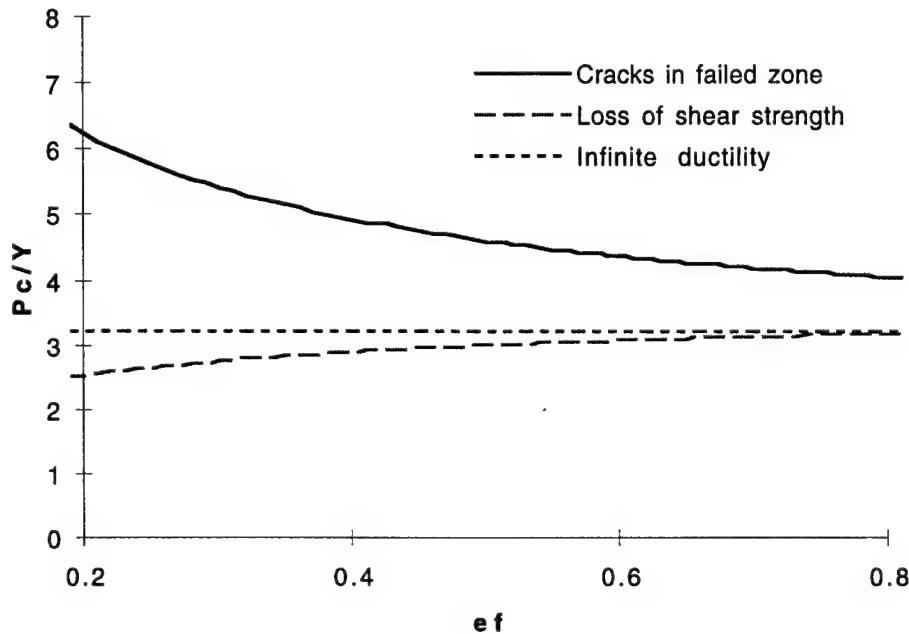
Figure 2.6. Cavity expansion pressures vs. failure strain.

In Figure 2.7, the post test sectioned specimen of the target used by Bless et al. (1996) is reproduced. It is observed that the cracked zone extends to about 1.6 times the cavity size. This is in reasonable correspondence with Figure 2.5 for $\varepsilon_f = 0.2$.

Figure 2.7. Cracked zone in Ti alloy target (Bless et al. 1996).

2.5 Effect of finite target thickness on penetration resistance

The common conceptual framework for describing penetration of long projectiles is based on the work of Tate (1967, 1969). Penetration is considered as steady state; the penetrator of density r_p and velocity V_p penetrates the target of density r_t with a velocity U_p. Along the center streamline, one uses the approximation

$$Y + \frac{1}{2}\rho_p\left(V_p - U_p\right)^2 = \frac{1}{2}\rho_t U_p^{\ 2} + R_t, \tag{2.72}$$

which equates the stresses in the target (RHS) and projectile (LHS) at their interface. Here, Y is the strength of the penetrator and R_t is the target resistance. This is referred to as the Tate equation. Quasi-static cavity expansion pressure is a good approximation for R_t.

In the cavity expansion analysis, it is assumed that the cavity opens in a infinite medium and hence the cavity expansion pressure turns out to be independent of the geometry of the cavity and only a function of the material parameters. However, for penetration into a finite target, the proximity to the boundary can affect the penetration resistance of the target. Normandia and Littlefield (1996) conducted penetration experiments into high hard 4340 steel (BHN 330) using

35

tungsten projectiles. The impact velocity was near the ballistic limit. They thereby, observed the effects of finite dimension on the average target resistance (Figure 2.8). The latter was calculated using Tate equation to match the depth of penetration.
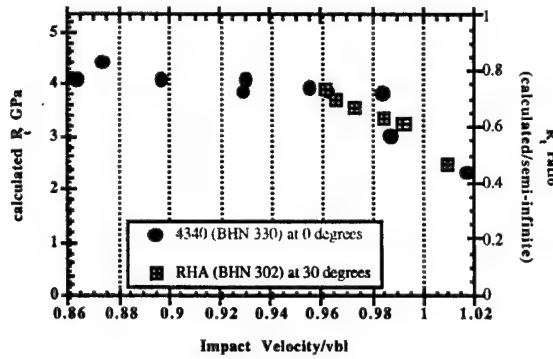
Figure 2.8. Degradation of penetration resistance near ballistic limit velocity (Normandia and Littlefield 1996).

The cavity expansion analysis can be easily modified to account for finite target thickness effects by solving the field equations with changed boundary conditions reflecting a stress free surface at a finite distance. The response regions in a finite target are depicted in Figure 2.9.
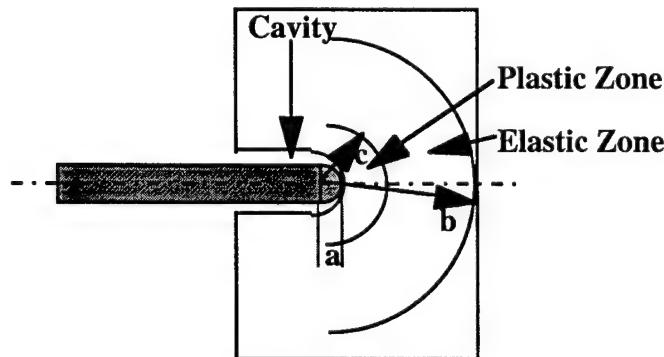
Figure 2.9. Response regions in a finite target.

The stress field ahead of the penetrator tip is assumed to have spherical symmetry. If the stress at the cavity surface is sufficiently high, the material yields. As a result, a plastic zone extends into the target with radius c, beyond which the target material is elastic. The displacement

36

in the elastic region is given in Eq. (2.5). Using Eqs. (2.2) and (2.3), the following solution is obtained for the stresses in the elastic region:

$$\sigma_r = c_1(3\lambda + 2\mu) - 4\mu\frac{c_2}{r^3} \quad \text{and} \quad \sigma_\theta = c_1(3\lambda + 2\mu) + 2\mu\frac{c_2}{r^3}. \tag{2.73}$$

Using a stress free boundary condition at $r = b$, i.e., $\sigma_r(r = b) = 0$ and the condition that the material begins to yield at $r = c$, i.e., $(\sigma_r - \sigma_\theta)|_{r=c} = Y$, one obtains

$$c_1 = \frac{2Y/3}{3\lambda + 2\mu}\left(\frac{c}{b}\right)^3 \quad \text{and} \quad c_2 = \frac{Yc^3}{6\mu}. \tag{2.74}$$

Thus, the solutions for displacement and the stresses in the elastic region are given by

$$u = \frac{Y}{6\mu} r \left(\frac{c}{r}\right)^3 \left[1 + \frac{4\mu}{3\lambda + 2\mu}\left(\frac{r}{b}\right)^3\right], \tag{2.75}$$

$$\sigma_r = \frac{2Y}{3}\left(\frac{c}{r}\right)^3\left[\left(\frac{r}{b}\right)^3 - 1\right] \quad \text{and} \quad \sigma_\theta = \frac{2Y}{3}\left(\frac{c}{r}\right)^3\left[\left(\frac{r}{b}\right)^3 + \frac{1}{2}\right]. \tag{2.76}$$

Integration of Eq. (2.1) for the plastic region with $\sigma_r - \sigma_\theta = Y$ yields

$$\sigma_r = 2Y \ln r + c_3. \tag{2.77}$$

Normal stress is continuous across the elastic-plastic interface ($r = c$). Thus c_3 is evaluated from Eqs. (2.73) and (2.76) as

$$c_3 = -2Y\ln c - \frac{2Y}{3}\left[1 + \frac{3\lambda + 2\mu}{4\mu}\left(\frac{c}{b}\right)^3\right]. \tag{2.78}$$

Denoting the negative of the stress at the cavity boundary, $r = a$, as the target resistance, R_t,

$$R_t = 2Y\ln\left(\frac{c}{a}\right) + \frac{2}{3}Y\left[1 - \left(\frac{c}{b}\right)^3\right], \tag{2.79}$$

37

where the explicit dependence of R_t on the proximity to the target rear surface is evident. The relative size of the plastic zone, c, is determined from mass conservation equation, Eq. (2.21). Assuming that the plastic zone is non-dilatant and neglecting higher order terms in u(c), integration of Eq. (2.21) between r = a and r = c yields

$$\frac{u(c)}{c} = \frac{1}{3}\left(\frac{a}{c}\right)^3 . \tag{2.80}$$

Displacement is continuous across the elastic-plastic interface (r = c) and hence from (2.75), an expression for the relative size of the plastic zone, a/c, is:

$$\left(\frac{a}{c}\right)^3 = \frac{Y}{2\mu}\left[1 + \frac{4\mu}{3\lambda + 2\mu}\left(\frac{c}{b}\right)^3\right]. \tag{2.81}$$

Finally, using this relationship in Eq. (2.79) to eliminate the cavity radius, a, an expression for R_t is obtained as a function of material constants and relative proximity to the target boundary.

$$R_t = \frac{2}{3}Y\left[1 - \left(\frac{c}{b}\right)^3\right] - \frac{2}{3}Y \ln\left[\frac{Y}{2\mu}\left\{1 + \frac{4\mu}{3\lambda + 2\mu}\left(\frac{c}{b}\right)^3\right\}\right] . \tag{2.82}$$

The target boundary limits the extent of the elastic region, b. The distance to the rear surface, b, appears in the expression normalized by the plastic zone radius, c, which from Eq. (2.75) is related to cavity size radius, a. Bishop et al.'s result (Eq. 2.40) for semi-infinite targets is recovered in the limit as, b → ∞. After the plastic region touches the boundary, Eq. (2.79) is used directly with c = b.

In a penetration formulation, it is more convenient to express R_t in terms of cavity radius a and b. One can rearrange Eq. (2.81) to determine c/b in terms of a/b. This gives an expression for the plastic zone size in terms of cavity radius, namely:

$$\left(\frac{c}{b}\right)^3 = \frac{-\dfrac{Y}{6\mu} + \sqrt{\left(\dfrac{Y}{6\mu}\right)^2 + \dfrac{4}{3}\left(\dfrac{2Y}{3}\right)\dfrac{1}{3\lambda + 2\mu}\left(\dfrac{a}{b}\right)^3}}{\left(\dfrac{4Y}{3}\right)\dfrac{1}{3\lambda + 2\mu}}. \tag{2.83}$$

Substitution of Eq. (2.83) into Eq. (2.82) gives the value of R_t for a given cavity radius, a, and distance from the boundary, b.

The cavity size can be calculated from Tate's (1986) formula,

$$\frac{a}{a_p} = \sqrt{1 + \frac{2\rho_p(V_p - U_p)^2}{R_t}}, \tag{2.84}$$

where a_p is the radius of the penetrator and V_p and U_p are the tail and tip velocities, respectively, of the penetrator calculated from Tate equation (2.72). Eqs. (2.82), (2.83) and (2.84) have to be solved simultaneously along with the Tate equation (2.72) to obtain the target resistance value at each time step.

Using 1.4 GPa as the dynamic flow stress of the target material, E = 206 GPa and $\nu = 0.3$, from Eq. (2.40) one obtains the target resistance for an infinite medium as 5.3 GPa. In Figure 2.10 the penetration depth calculated from Tate equation using a fixed target resistance of 5.3 GPa and that calculated from Eqs. (2.82), (2.83) and (2.84) are shown along with the experimental data from Normandia and Littlefield (1996). The cavity expansion pressure modified to account for finite target thickness is in good agreement with experimental data. Normandia et al. (1996) used this model to study the penetration into double RHA targets separated by an air gap. They found that the trends in the penetration velocity as predicted by the hydrocode CTH in the first RHA target are well captured by this model.
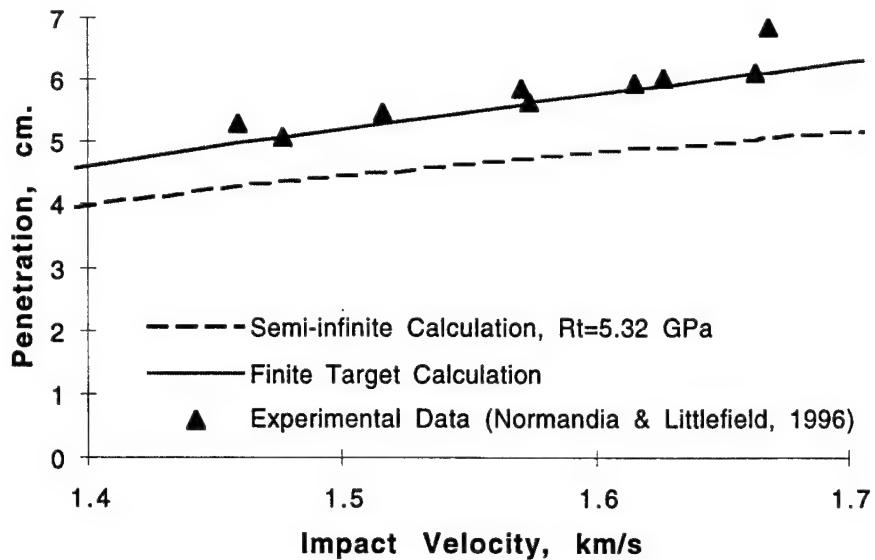
Figure 2.10. Comparison of finite target model with experimental data.

Recently, cavity expansion analysis has also been exploited to account for finite lateral extent of the target by Littlefield et al. (1997). A cylindrical cavity expansion pressure was derived taking into account the presence of the finite lateral extent. The cavity expansion pressure was averaged over the final cavity size to determine the penetration resistance of the target. Good agreement was found with hydrocode simulations. Partom (1996) developed a "limit of stability" concept for penetration resistance of finite targets. Solving the cavity expansion problem with non zero initial inner radius and a finite outer radius, he observed a maximum in pressure in the P_c/Y vs. a/a_0 plot. He defined this maximum as the "limit of stability." By this he meant that if the applied pressure was below this value, a stable cavity growth would ensue. On the other hand, if the applied pressure was more than this maximum pressure, the cavity would grow in an unstable manner. Using this concept, he showed that a spherical cavity expansion analysis results in better agreement with hydrocode simulations than a cylindrical cavity expansion analysis. His expression for the spherical cavity expansion pressure is identical to Eq. (2.79), which was derived independently by this author, prior to Partom's work. Partom's expression for the relative size of the plastic zone is

$$\left(\frac{c}{a}\right)^3 = \frac{2\mu}{Y} \frac{\left(1 - a_0^3/a^3\right)}{1 + 2\frac{1-2\nu}{1+\nu}\left(\frac{c}{b}\right)^3}. \tag{2.85}$$

For $a_0 = 0$ (i.e., expansion of the cavity from zero initial radius), Eqs. (2.85) and (2.81) are identical, in view of the relation, $\lambda = 2\mu\nu/(1-2\nu)$.

40

2.6   Punch tests in PMMA

Punch tests were conducted to explore the phenomenology of penetration in quasi-brittle materials and provide a quantification check on cavity expansion analysis. Armor materials are so hard that penetration by means of a rigid punch is probably impossible. Thus PMMA was selected as a surrogate on which to measure penetration force. It turned out that the PMMA developed brittle like cracks when tested without confinement. Under confinement, PMMA behaved more like a plastic than a brittle material. A distinct plastic zone could be observed surrounding the cavity. It was found that the load vs. displacement curves are well explained using elastic-plastic cavity expansion theory.

2.6.1   Test description

The tests (see Table 2.1) were conducted on an MTS machine with maximum capacity of 90 KN (20 klbs). A LVDT was used to measure the displacement of the punch. The load was plotted versus the stroke on a chart recorder. All the punch tests were done on PMMA, a low strength thermoplastic. Due to the time-dependent nature and temperature dependence of mechanical properties, its strength parameters are in general history dependent. All our tests were conducted at room temperature in a quasi-static manner. Steinberg (1991) gave the properties of PMMA as: shear strength = 2.32 GPa, bulk sound speed = 2180 m/s and density = 1182 kg/m^3. Other material properties calculated from Steinberg's data are: modulus of elasticity, E = 6.12 GPa, and ν = 0.32. Earlier compression tests (Lee and Satapathy 1994) on the samples studied in the present tests had shown the static yield strength to be 166 MPa.

The punches were tool hardened circular steel rods with a shank radius of 3.175 mm (0.125"). The conical punch had a 18.43° semi-included cone angle. All the PMMA specimens were 152 mm X 152 mm X 50 mm (6" X 6" X 2") blocks. The punches were held in place by a drill chuck attached to the load cell of the cross arm of the MTS testing machine. The specimens were placed on a platen, which was raised at the specified displacement rate by a hydraulic piston while the punch was held in a fixed position. For the confined tests, the blocks were confined peripherally by four steel plates (see Fig. 2.11), which were held against a hollow rectangular steel block by six bolts (3/8" nominal dia, 16 threads per inch) on each side. For the experiments where no initial pressure was to be applied, the bolts were sufficiently tightened so that the plates were

just in contact with the blocks. For the experiments in which confining pressure was to be applied, each bolt was tightened to a torque of 25 ft-lbf (34 m-N) by a torque wrench. The resulting transverse stress was about 6.89 MPa (1 ksi). Table 2.1 shows the test matrix.

Table 2.1. Test Matrix

Test No.	Punch shape	Max. Load(KN)	Defl. at max. load(mm)	Confinement	Comment
1	Conical	15.03	15.24	UC	Sample split into two
2	Conical	14.95	15.24	UC	Sample split into two
3	Conical	20.91	28.58	CWNP	No cracks
4	Conical	20.02	22.86	CWNP	No cracks
5	Conical	44.48	19.05	CWP	No cracks
6	Spherical	20.02	7.95	UC	Sample split into two
7	Spherical	17.79	8.89	UC	Sample split into two
8	Spherical	22.24	25.4	CWNP	Sample cracked but didnot split
9	Spherical	26.69	14.22	CWP	Cracks grew upon removal of confinement.

UC: Unconfined;   CWP: Confined With Pressure;   CWNP: Confined With No Pressure

The tests were conducted in the stroke control mode, with a maximum stroke of 63.5 mm (2.5") and with a maximum load of 44.48 KN (10,000 lbs). The input was in the form of a ramp of 5 seconds duration.
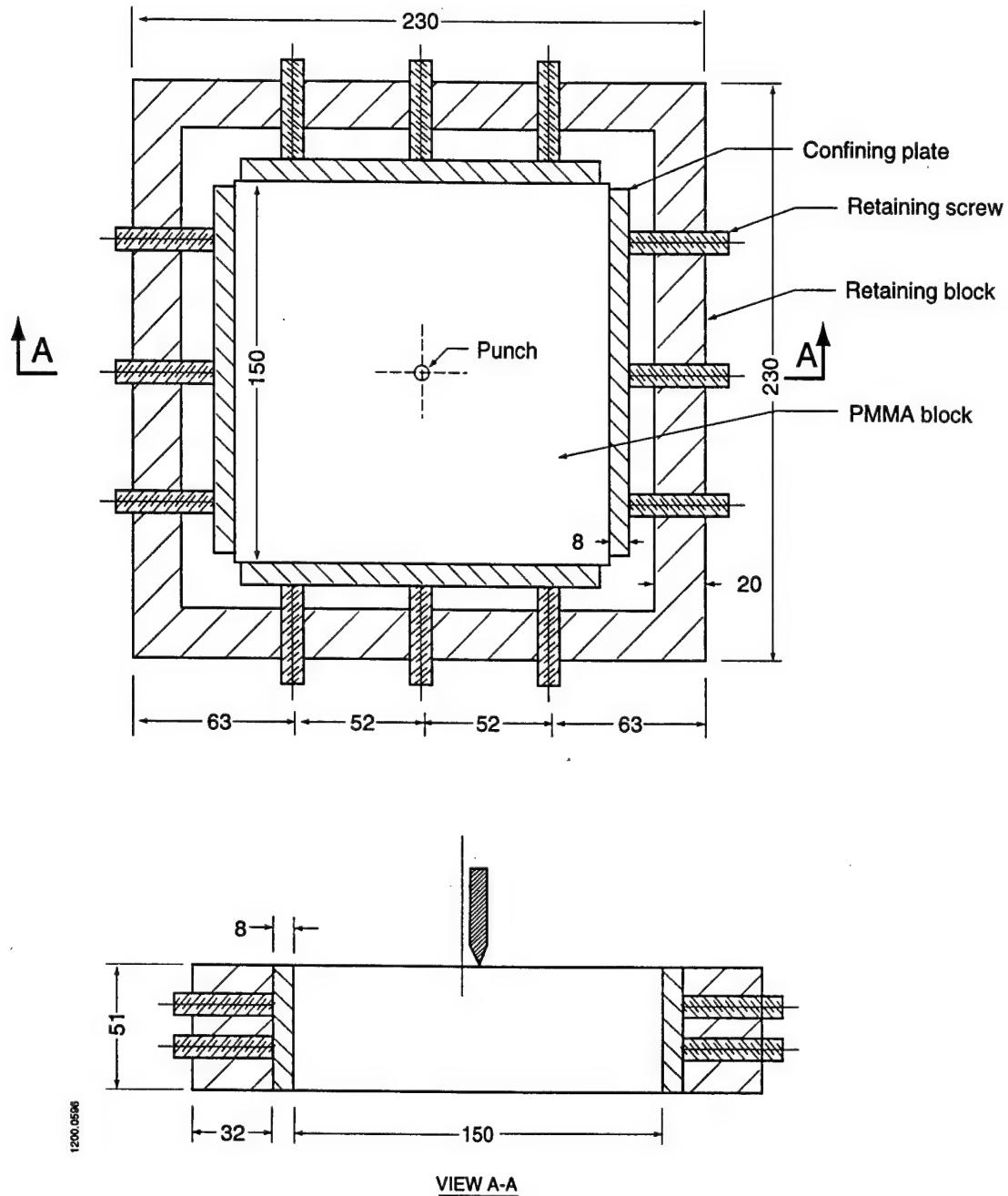
Figure 2.11. Arrangement for confined tests.

2.6.2 Results and discussions

The details of the cracking phenomenology observed in these experiments is described by Satapathy and Bless, (1995). The load (axial force) vs. stroke plots for various cases are presented in Figure 2.12 in the same diagram for ease of comparison. The legends used in Figure 2.12 are as follows: UC: Unconfined; CWP: Confined with Pressure; CWNP: Confined with no pressure. The last letters "s" and "c" stand for spherical and conical nosed punches, respectively.

Splitting of Unconfined Blocks: The acrylic blocks fractured into two separate pieces in both the unconfined tests with spherical nosed punch and in two of the three unconfined tests with conical punch. When the blocks split, the load dropped to zero. Although cracks sometimes formed in the confined tests, the block could not split apart.

Knee in Load-Displacement Curves: Knees in the load-stroke plot are observed at a penetration of about 0.5 X diameter (full embedment) of the spherical punch and at about 1.5 X diameter (full embedment) of the conical punch.

Increasing Load in Confined Tests: In the confined tests, force always increased with penetration, apparently due to friction on the lateral face of the punch, whereas in unconfined tests the force was nearly constant after full embedment. This is presumably because, in the absence of confinement, the lateral surface loses contact with the specimen as the cracks form and propagate.

Load Relaxation Due to Cracks: Drops in the load-displacement record are caused by crack initiation and propagation. For example, as can be seen from Figure 2.12 (CWNP-S), in the confined test with spherical nosed punch, the cracks started at a penetration of about 8 mm (0.3") and either stopped or stabilized at a penetration of about 13 mm (0.5").
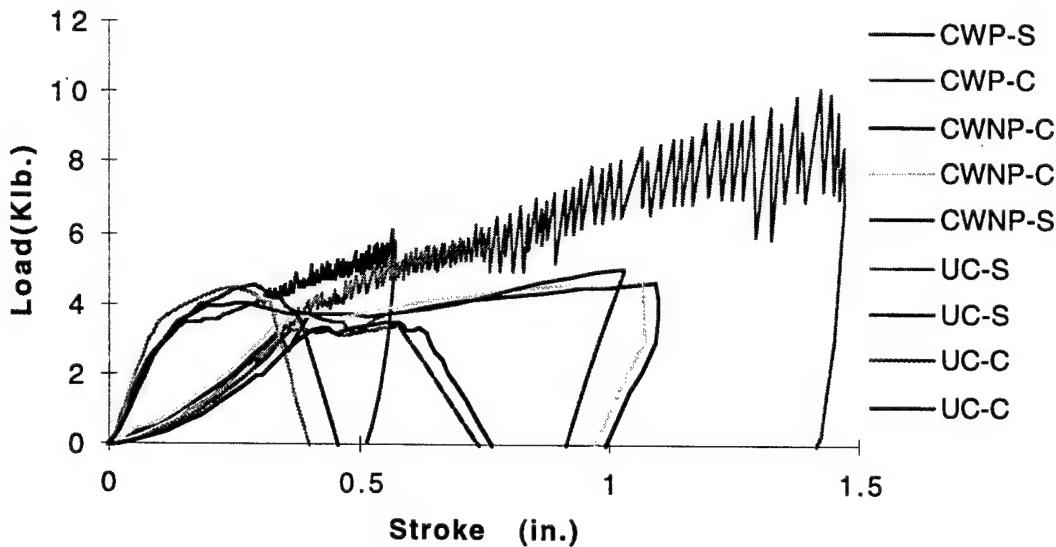
Figure 2.12. Load vs. stroke plot for all tests.

Oscillation in Load: For tests with initial confinement pressure, load spikes are observed at frequent intervals. These spikes are not due to crack initiation or propagation, since with the conical punch, no cracks were formed but the load spikes were still present. I believe that the load spikes are the result of shearing of the lateral surface of the specimen in contact with the punch; i.e., load increases until the lateral surface experiences a limiting shear stress, after which the load drops due to shearing failure of this surface. As the penetration increases, the lateral surface area increases; therefore, a larger amount of load can be withstood prior to slip. As a consequence, the amplitude of the spikes increase with increasing penetration. For the spherical punches, the spikes appear after the knee of the load-stroke diagram, but for conical punches these spikes are observed even before the knee. This is so because the spherical head can transmit more load than the conical head. As a result, the proportion of load supported by the lateral surface is more for the conical punch. Hence, the lateral surfaces start shearing at a lower value of total load. The ratio of the load carried by the head to that carried by the lateral surface can also be found from the slope of the load-stroke plot, since in the absence of lateral load, the slope should have been zero. It is surmised that the contact quasi-static friction coefficient can be calculated from this slope.

Spherical Punches Induce Earlier Fracture: In the unconfined tests, the spherical nosed punches penetrated less before fracture than did the conical punches. In all the tests, the spherical punches had a higher load-stroke slope, higher load at the knee, and higher peak load before

45

fracture as compared to the conical nosed punches. This behavior conforms to the effect of nose shape as discussed in Eqs. 2.6.3.2.

Suppression of Cracks in Confined Blocks with Conical Punch: In the confined tests, the acrylic blocks did not develop any crack under the conical punch. The punch was simply embedded in the block. In contrast, under a spherical punch, even though cracks were formed, the block did not fragment into pieces in the presence of lateral confinement.

2.6.3   Comparison of experimental data with CEA predictions

2.6.3.1   Unconfined tests

In the unconfined tests, propagation of cracks results in splitting of the specimen which renders comparison of experimental data with CEA predictions (where presence of a running crack is unaccounted for) difficult. On the other hand, confinement suppresses crack extension and the lateral surface of the penetrator does not loose contact with the specimen. Thus for unconfined tests, I simply compare the maximum experimental load with the prediction from the CEA, while for the confined tests, I compare the whole load-stroke·plot with the CEA prediction.

Taking into account the geometry of the nose, assuming tangential stress on the nose to be proportional to the normal stress and neglecting friction on the shank of the penetrator, Forrestal et al. (1988) showed that for a spherical nose, axial load is given by:

$$F_z = \pi a^2 P_c \left(1 + \frac{\mu_f \pi}{2} \right). \tag{2.86}$$

where μ_f is coefficient of sliding friction and P_c is the cavity expansion pressure. For a conical nose, the axial load is given by:

$$F_z = \pi a^2 P_c \left(1 + \frac{\mu_f}{\tan \phi} \right), \tag{2.87}$$

where ϕ is the semi included angle.

I assume a friction coefficient, μ_f of 0.15. Table 2.2 shows the experimental and theoretical values of the force on the tip of the punch. It is seen that the spherical cavity expansion solutions of Bishop, et al. (Eq. 2.40) and Hill (Eq. 2.44) yield the closest predicted load values for spherical and cylindrical punch tests, respectively.

2.6.3.2 Confined tests

Following Forrestal et al. (1988) I calculated the theoretical load-stroke curve as follows:

a) Spherical nosed penetrator

$$\text{For } z < a: \quad F_z(z) = \pi a^2 P_c \int_0^{\cos^{-1}(1-z/a)} (\sin 2\theta + 2\mu_f \sin^2\theta) d\theta. \tag{2.88}$$

$$\text{For } z > a: \quad F_z(z) = \pi a^2 P_c \left(1 + \frac{\mu_f \pi}{2}\right) + 2\pi \mu_f r P_c (z-a). \tag{2.89}$$

where z is the penetration depth, a is the penetrator radius and P_c is the cavity expansion pressure.

b) Conical nosed penetrator

$$\text{For } z < a/\tan\phi: \quad F_z(z) = \pi P_c \left(1 + \frac{\mu_f}{\tan\phi}\right) z^2 \tan^2\phi. \tag{2.90}$$

$$\text{For } z > a/\tan\phi: \quad F_z(z) = \pi a^2 P_c \left(1 + \frac{\mu_f}{\tan\phi} + \frac{2\mu_f}{a}\left(z - \frac{a}{\tan\phi}\right)\right). \tag{2.91}$$

Where F_z is the axial force exerted by the penetrator, z is the depth of penetration, a is the penetrator radius and ϕ is the penetrator cone angle.

Table 2.2. Comparison of Experimental Values of Maximum Axial Load with CEA Predictions for Unconfined Experiments

			P_c(CEA) (GPa)	Fz(CEA) (KN)	Fz(Exp.) (KN)
(a) Spherical Punch	Cylindrical Cavity	BHM	0.401	15.7	17.8-20
		Hill	0.368	14.4	17.8-20
		No. Vol. Change	0.389	15.22	17.8-20
	Spherical Cavity	BHM	0.479	18.74	17.8-20
		Hill	0.431	16.87	17.8-20
		No Vol. Change	0.465	18.2	17.8-20
(b) Conical Punch	Cylindrical Cavity	BHM	0.401	18.4	15
		Hill	0.368	16.9	15
		No. Vol. Change	0.389	17.86	15
	Spherical Cavity	BHM	0.479	15.7	15
		Hill	0.431	14.4	15
		No Vol. Change	0.465	15.22	15

The Eqs. (2.88) to (2.91) are plotted in Figure 2.13 for $P_c = 0.431$ GPa (spherical cavity expansion pressure from Eq. 2.44) and for $P_c = 0.368$ GPa (cylindrical cavity expansion pressure from Eq. 2.61). The experimental curves are also plotted in the same figure. It is found that the experimental curves lie within the predictions from spherical and cylindrical cavity expansion analyses for partial embedment of the punch. After the punch is fully embedded (i.e., after a penetration of 0.5D for spherical punch and 1.5D for conical punch), the experimental data conform to the cylindrical cavity expansion analysis. This is to be expected since after the head is fully embedded, the pressure on the lateral surface of the punch is due to walls of the cylindrical cavity. In addition, it is found that the correlation between the experimental and theoretical curves is excellent.
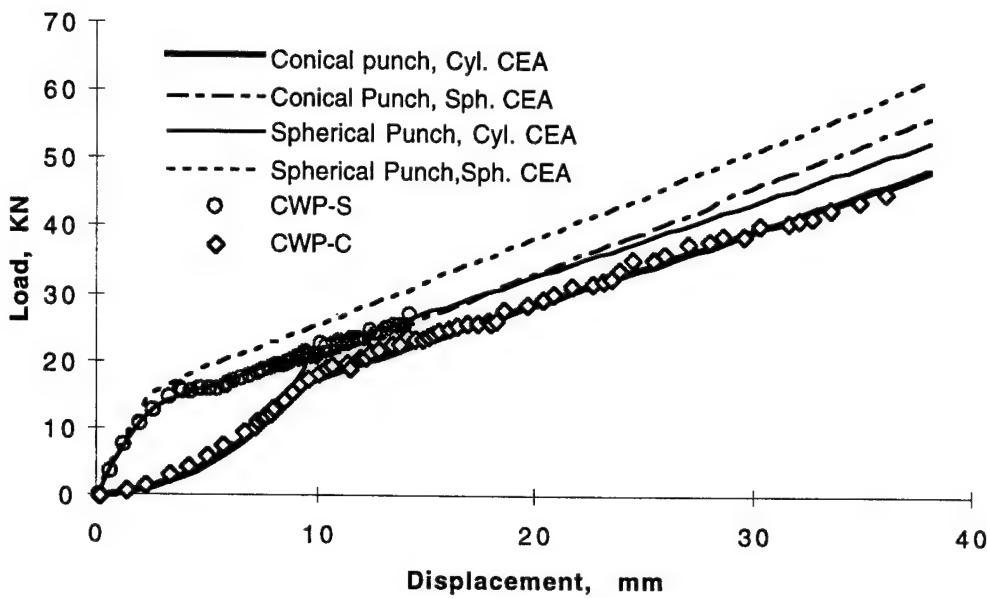
Figure 2.13. Comparison of data from confined experiments with CEA predictions.

2.6.3.3   Plastic zone

As mentioned earlier, for the spherical punch case with initial confinement pressure, a distinct plastic zone appeared (Figure 2.14). This zone is brought out clearly by using differential lighting and careful exposure. In this zone the lateral cracks are absent. At the punch tip, this region has a radius of about 2.4 X cavity radius (i.e., $c/a = 2.4$, where c is the plastic zone radius and a is the penetrator radius). Boussinesq's solution (Timoshenko and Goodier 1987) for contact stress correlates the contact pressure with stress at a given distance, and is given by

$$\frac{1}{2}(\sigma_\theta - \sigma_z) = \frac{q}{2}\left[\frac{1-2\nu}{2} + (1+\nu)\frac{z}{\sqrt{a^2+z^2}} - \frac{3}{2}\left(\frac{z}{\sqrt{a^2+z^2}}\right)\right], \qquad (2.92)$$

where σ_θ and σ_z are circumferential and radial stresses respectively, q is the pressure under the punch of radius a, z is the axial coordinate. Using the von Mises criterion for the plastic zone, the LHS of Eq. (2.92) is equal to the shear strength of the material, which is 83 MPa. a is 3.175 mm; q is approximated by the maximum load divided by the nose area (assuming that, due to shearing at

49

the lateral contact surface, at some point in time the total load is supported by the nose head). Its numerical value is 0.632 GPa. Use of a ν of 0.32 yields a z of 5.21 mm. Thus the plastic zone size is about c/a = 2.64.
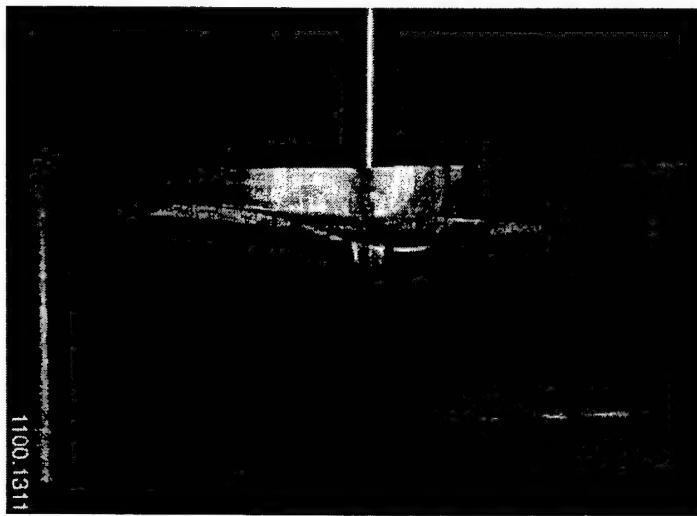
Figure 2.14. Plastic zone in PMMA.

Table 2.3. Comparison of plastic zone size

		c/a
Experimental	-	2.4
Boussinesq	-	2.64
BHM model	-	2.9
Hill	-	2.58
No Vol. Change	-	2.77

Similarly, cavity expansion solution Bishop et al. (Eq. 2.39) yields a value of 2.9 for c/a and Hill's formula (Eq. 2.43) yields a value of 2.58. Since the cavity expansion solutions assume expansion of a cavity in an infinite medium from zero radius, they provide an upper limit for c. Hill's (1950) compressible solution yields the closest value for c/a obtained from the experiment. Even though Eqs. (2.39) and (2.43) were derived for expansion of cavities in infinite media, Satapathy and Bless (1995) have shown that application of confinement pressure at a finite

50

boundary does not change the plastic zone size significantly. On the otherhand, I relied on the change of refractive index of the sample to give an indication of plastic zone. It is possible that the refractive index does not change much near the elastic-plastic interface, and hence experimental measurement may not yield an accurate value for the plastic zone size. Thus, in essence, the cavity expansion solutions give a reasonable prediction of the experimentally observed plastic zone size.

Chapter 3: Cavity Expansion Analysis of Brittle Ceramics

Brittle materials possess low tensile strength and low ductility. As a result, they readily fracture under tensile loading conditions and cannot withstand large strains without developing cracks. However, low density, high compressive strength and hardness, and good thermal properties make brittle ceramics like Al_2O_3, AlN, SiC, TiB_2 suitable for use as light weight armors and other protective structures. Various issues associated with the impact behavior of ceramic materials have been discussed by Bless and Lopatin (1988), Rajendran and Cook (1988) and Bless and Rajendran (1996). The dynamic properties of armor ceramics have been characterized by many researchers, e.g., Grady (1995), Raiser and Clifton (1993), Rosenberg, et al. (1991), Sairam and Clifton (1994), Subramanian and Bless (1995), Orphal et al. (1996), Klopp et al. (1994), Cagnoux and Langy (1987), Simha and Bless (1995). Research has been conducted to characterize dynamic properties of other brittle materials like glass (Bless and Brar 1993; Bless et al. 1990, 1992), concrete (Forrestal and Tzao 1997), and rock (Forrestal 1986).

The analysis of the penetration response of brittle materials is complicated due to the presence of cracking and comminution (breaking into a powder-like structure). As a result, various simplifying assumptions are necessary to make the analysis tractable. Attempts have been made to describe the constitutive behavior, i.e., strength, plasticity, porosity and fracture of the ceramics (Rajendran 1993; Johnson and Holmquist 1992; Partom 1993; Littlefield et al. 1994). The existing constitutive models have not reached a level where design of armors can be reliably carried out. In some cases, quantitative predictions are impossible, while in others, basic phenomenology cannot be duplicated. Bless et al. (1993) found that state-of-the-art constitutive models employed in finite difference and finite element codes could not predict penetration of very thick ceramic tile (T/d > 18) by long rod projectiles. Thus extensive research is being carried out to develop better constitutive models for ceramic materials.

Cavity expansion analysis presents an excellent tool to identify various important material parameters affecting the resistance of brittle materials to penetration. Implications of different constitutive assumptions are easy to investigate using this method, rather than performing extensive numerical modeling. This approach has been used to characterize the penetration

resistance of brittle ceramics by Sternberg (1989), Forrestal and Longcope (1990), Florence et al. (1992), Wright et al. (1992), Partom (1993), Satapathy and Bless (1996) and Bless et al. (1996).

Even though the mechanical behavior described in the following discussion may be applicable to many different brittle materials, attention is restricted to modeling of armor ceramics only. In this chapter, the qualitative constitutive behavior of brittle materials is first discussed. Existing work on the cavity expansion analysis of brittle materials is briefly reviewed. However, observations of ceramic targets suggests that the operating failure mechanisms are not those on which past analyses are based. Therefore, a new quasi-static cavity expansion pressure is derived under appropriate assumptions and compared with available experimental data. The dynamic cavity expansion problem for a constant expansion velocity is also solved assuming steady state wave propagation. Finally, a self-similar solution is presented for the dynamic case and the effect of a "shear cap" on the failed material behavior is discussed.

3.1   Constitutive behavior of brittle materials

Brittle materials usually possess very high compressive strength. Their shear strength increases with superimposed hydrostatic pressure. But they are extremely weak in tension and the spall strength[1] is about one order of magnitude smaller than the compressive strength. Hence these materials readily crack when subjected to relatively low tensile stress. Reflection of compressive elastic waves leads to failure in these materials, unlike metals. Experiments have shown that extensive tensile failure can be reduced or delayed by suitably confining the material. Material damage progresses due to the accumulation of micro-cracks initiated at the grain boundaries. Presence of glassy phases in the intergranular spaces aids in the "plastic" type flow of certain ceramic materials. Sternberg (1989) noted that since ceramic materials do not possess enough slip systems, "plasticity" observed in these materials is not similar to von Mises type plasticity in which five independent slip systems are required. The plastic-type behavior of ceramics at high pressures arises from micro-cracking and intergranular shear. The intact material slowly rubblizes and becomes comminuted as the induced damage increases. The presence of the Mescall zone[2] under high speed penetration is a result of this comminution. Oblique plate impact tests suggest that the shear stress in the failed material bears a constant ratio to the applied normal stress. Very-high

---

[1] defined as the tensile strength in one dimensional strain configuration, such as in a plate impact test

[2] defined as a region where material is comminuted or reduced to powder-like granular structure

54

pressure plate impact tests have shown that the shear strength of certain ceramics saturates at a level slightly higher than that experienced at the Hugoniot Elastic Limit[1] (HEL).

The above description leads to a two-curve behavior of brittle ceramics (Figure 3.1) in describing their pressure-shear relationship, as discussed by Bless and Lopatin (1988), Johnson and Holmquist (1992), Partom (1993), Cosculleula (1992). In this figure, P denotes the hydrostatic pressure and S denotes the maximum shear stress (i.e., one half the difference between maximum and minimum principal stresses). An "upper curve" is required to describe the pressure-dependent shear strength of the intact material, whereas, a "lower curve" is needed to describe such behavior in the failed material. These curves do not prescribe any general path for the material to follow; rather they impose a limiting material behavior. The upper curve serves as a failure criterion, since upon reaching this curve, the material fractures. The lower curve is like a flow curve for the failed material. The actual path followed should lay somewhere between these two curves, depending on the loading path imposed. If the material fails and drops to the lower curve, then it should stay on that curve.
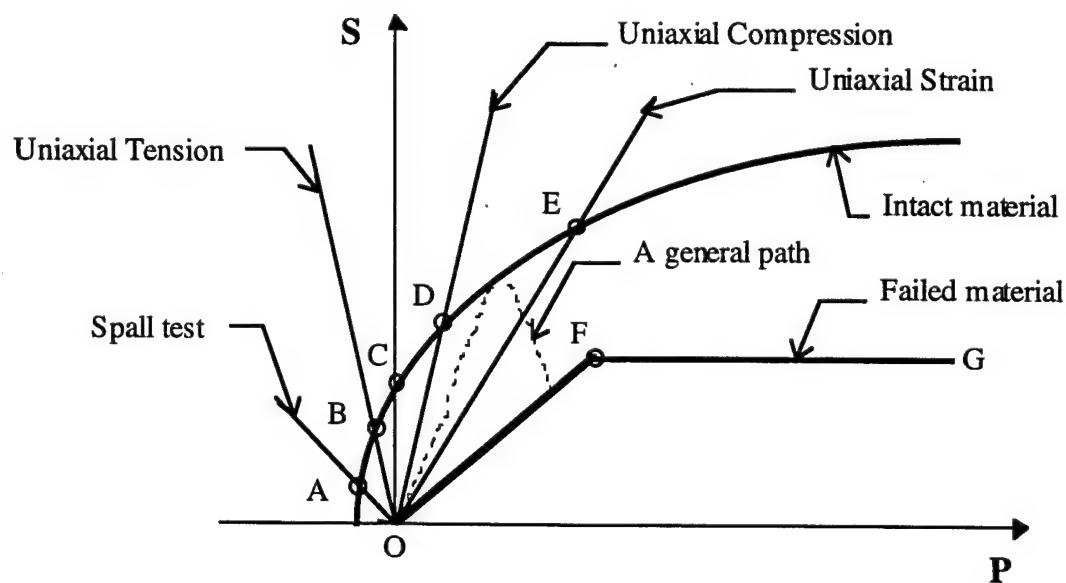
Figure 3.1. Qualitative Constitutive description of Brittle Materials

---

[1] defined as the level of axial stress at which transition from elastic to plastic behavior is observed in a one dimensional strain configuration, such as in a plate impact test

There is no single experimental technique which can be used to characterize more than a small region of the relevant stress state. However, several distinct points along the curves can be identified with standard experiments. Point "A" can be reached with a spall test (tensile test in 1-D strain mode), in which the shear strength and pressure are given by,

$$S = \frac{\sigma_x}{2} \frac{(1-2v)}{(1-v)} \qquad \text{and} \qquad P = -\frac{\sigma_x}{3} \frac{(1+v)}{(1-v)}, \qquad (3.1)$$

where σ_x is the axial stress. Point "B" is determined by uniaxial tensile tests, in which the shear strength and pressure are given by,

$$S = \frac{\sigma_x}{2} \qquad \text{and} \qquad P = -\frac{\sigma_x}{3}. \qquad (3.2)$$

Point "C" can be evaluated with simple shear experiment, in which pressure is zero. The points "D" and "E" are given by uniaxial compression stress tests (bar impact) and uniaxial compression strain tests (plate impact). The shear stress and the pressure for these two points are the same as those for points "A" and "B", respectively, with the difference that pressures are of opposite sign. The upper curve is thus constructed by interpolation and extrapolation of these few well-defined points. Theoretically, compression tests in a Hopkinson bar with a superposed confinement pressure can yield more points on this curve. However, significant excursion from point "D" has not been possible yet due to experimental difficulties. Other possible test configurations include expanding ring, cylindrical impact, plane stress impact, etc. Research is being conducted in these areas currently.

The failed material is assumed to possess no cohesive strength, i.e., it cannot support any shear stress in the absence of confining pressure. Therefore, the lower curve passes though the origin. Oblique plate impact experiments show that for low speed impacts, the pressure-shear relation of the comminuted material is linear. High speed plate impact experiments show that for certain ceramics, the shear strength of the failed material is saturated at high pressures. Thus interpolating for intermediate pressures, the lower curve is assumed to be bilinear. The slope of the segment O-F is obtained from oblique plate impact tests, whereas the segment F-G may be obtained from high speed normal plate impact tests.

3.2 Review of existing cavity expansion models for brittle materials

Sternberg (1989) discussed various material properties that determine the resistance of ceramics to high velocity penetration. Recognizing that the constitutive behavior of ceramics is not well defined above the elastic limit, he pointed out the difficulty in directly extending the ductile cavity expansion approach to brittle materials. Forrestal (1986) considered the cracking behavior of dry porous rocks in deriving a dynamic cavity expansion solution. Using a Mohr-Coulomb-type strength criterion and a linear hydrostat, he obtained good agreement with projectile deceleration data obtained from experiments. Adopting a similar approach, Forrestal and Longcope (1990) derived the static cavity expansion pressure for ceramic materials. The assumed Mohr-Coulomb-type material description was given by

$$\sigma_r - \sigma_\theta = \lambda P + \tau,$$ (3.3a)

where τ is cohesive strength ($=2$ X the value of S at point "C" in Figure 3.1, since the LHS of Eq. 3.3a is 2S), and λ is the slope of the assumed linear pressure-shear curve ($=2$ X linear slope of the upper curve in Figure 3.1). To conform to the uniaxial compression test, λ and τ are related by

$$\tau = [(3 - \lambda) / 3] \, Y,$$ (3.3b)

where Y is the compressive strength. They considered three different scenarios for the behavior of the material beyond the cavity: elastic-cracked problem, elastic-plastic problem and elastic-cracked-plastic problem. In the "plastic" region the material followed the upper curve of Figure 3.1. Their solutions showed that the elastic-cracked-plastic situation yields the smallest value for the cavity expansion pressure. For the elastic-cracked-plastic problem, the cavity expansion pressure was given by

$$P_c = \frac{Y}{\lambda} \left[\frac{2}{\lambda} \left(\frac{c}{a} \right)^{\alpha\lambda} - \frac{3-\lambda}{3} \right],$$ (3.3c)

where $\alpha = \dfrac{6}{3+2\lambda}$; $\left(\dfrac{c}{a}\right)^3 = \beta + \dfrac{\beta(1-2\nu)}{\lambda E}\left[3 - \lambda - (3+2\lambda)\beta^{-\alpha\lambda/3}\right]$; $\beta = \dfrac{9(1-\nu)}{2}\left(\dfrac{Y}{E}\right)\left(\dfrac{Y}{2\sigma_f}\right)^{1/2}$,

and σ_f is the tensile strength.

For AD995 alumina ceramic, bar impact tests (Simha and Bless, 1995) indicate a compressive strength, Y, of 3 GPa (Point "D" in Figure 3.1). Plate impact tests (Grady, 1995) give a value for HEL (point "E" in Figure 3.1) as 6.2 GPa. Eqs. (3.1) and (3.2) yield a slope of 0.322 for a linear fit between these two points. Since λ is twice this slope, $\lambda = 0.644$ and $\tau = 2.36$. Calculation of the S-intercept of the linear fit through points "D" and "E" gives an identical value for τ. The other constants for AD995 are: $E = 373$ GPa, $\nu = 0.22$ (from Grady, 1995), $\sigma_f = 0.262$ GPa (Coor's data). Evaluation of Eq. (3.3b) with the above constants results in 11.54 GPa for P_c. However, penetration experiments (Subramanian and Bless, 1995) indicate that the penetration strength of this ceramic varies from 7 GPa to 9 GPa, with an average value of 8.5 GPa. Thus the Forrestal and Longcope model overpredicts the target resistance for AD995 by about 35%. Evaluation of the elastic-plastic model and the elastic-cracked model of Forrestal and Longcope yield a cavity pressure of 15.3 GPa and 18.03 GPa, respectively.

I believe that the discrepancy between Forrestal and Longcope's prediction and the experimental value of the target resistance is due to the fact that the behavior of the failed material (lower curve in Figure 3.1) has not been considered. While their model was a step forward towards modeling the cracking behavior due to low tensile strength, it did not account for the complete failure and comminution of the ceramic material which is observed in the penetration event.

Florence et al. (1992) considered a failed-cracked-elastic model for ceramics. In their model, incompressibility was assumed for all the regions. The strength of the failed material was taken to be a constant, i.e., the saturation level of the lower curve. Thus they ignored the linear portion of the pressure-shear relation for the failed material. The cavity pressure was given by:

$$P_c = Y + \frac{2}{3}\sigma_0 \ln\left(\frac{2E}{3Y}\right) + \rho V^2 \left\{2\left[1-\left(\frac{3Y}{2E}\right)^{1/3}\right] - \frac{1}{2}\left[1-\left(\frac{3Y}{2E}\right)^{4/3}\right]\right\}$$
$$+ \rho V \dot{V}\left[1-\left(\frac{3Y}{2E}\right)^{1/3}\right], \qquad (3.4)$$

where $\sigma_0 = 2S_F = \sigma_r - \sigma_\theta$.

For AD995 ceramic, with representative values of $S_F = 1.5$ GPa and 2 GPa (values of S_F are discussed in section 4.3.1.9), the static cavity expansion pressures from Eq. (3.4) are 11.84 GPa and 14.78 GPa, respectively. These values are more than 40% above the average experimental penetration resistance value. I shall compare the full dynamic cavity expansion pressure in Eq. (3.4) with the current analysis later in this chapter.

Partom (1993) modeled the behavior of ceramic materials using the constitutive behavior as described in Figure 3.1. Bilinear representations for the pressure-shear behavior of both the intact and the failed material were considered. He derived the cylindrical cavity expansion pressure using an elastic-plastic-type material behavior, where a "plastic" behavior used for the failed material. The elastic zone extended from the point "O" to the S-intercept, point "C". The cavity expansion pressure was given by,

$$P_c = \frac{Y}{\sqrt{3}}\left(\frac{\sqrt{3}\mu}{Y}\right)^{m/(\sqrt{3}+m)}, \qquad (3.5)$$

where m is the pressure-shear slope of the lower curve, and Y is the strength of the material at zero pressure (point "C"). Evaluating this expression for AD995, with representative values for m of 0.2 and 1, P_c is 2.75 GPa and 8.9 GPa, respectively. Evaluation of the hoop stress at the inner boundary of the elastic zone yields $\sigma = -Y/\sqrt{3} = -1.73$ GPa, which is much smaller than the tensile strength of the material (~ -0.4 GPa). Partom's model is thus inconsistent with the tensile behavior.

Partom also considered the implications of the presence of a pressure field on the static cavity expansion solution. Instead of solving the full dynamic cavity expansion problem, for

59

simplicity he assumed that a uniform pressure field with pressure level equal to the inertial pressure $(=0.5\rho U_p^2)$ is present at the projectile-target interface. This constant inertial pressure was assumed to prevail throughout the target. Using this assumption, he derived the static cavity expansion pressure for different saturation values of the shear stress of the failed material. Since an inertial pressure field was superimposed, he had to simultaneously solve the Tate equation (Eq. 2.72) and the cavity expansion pressure equation. His results showed that penetration resistance of ceramics should increase with increasing penetration velocity for all values of pressure-shear slope.

Littlefield and Anderson (1994) also assumed a pressure dependent shear strength to derive the penetration resistance for ceramics. They used the Walker-Anderson model (1995) framework, where the target resistance was calculated using von Mises type plasticity. They did not consider any strength degradation due to cracking or comminution. Therefore, the material model used was elastic-plastic. Nevertheless, they found that the analytical prediction of position vs. time plots for penetration compared favorably with experimental results for an assumed pressure-shear coefficient of 0.75.

3.3   Quasi-static spherical cavity expansion analysis of brittle materials: A new approach

In the following, I will derive the cavity expansion pressure in a brittle material in which distinction is made between the strengths of intact and failed materials. First I derive the cavity expansion pressure for spherical symmetry. Then the solution for the cylindrical cavity expansion problem is presented. Using experimental values for various parameters, I will show that the resulting cavity expansion pressure indeed gives a reasonable prediction of the penetration resistance of typical ceramics materials used as armor.

3.3.1   Spherical cavity expansion

3.3.1.1   Response regions

In steady state penetration (after the initial shock phase is over), the penetrator erodes and decelerates due to the stress at the target-penetrator interface. The stress in the target that resists penetration consists of two parts: 1) the inertial stress required to accelerate target material out of the path of the penetrator; and 2) the stress required to deform the target around the cavity. This second term is identified with the target resistance R_t.

60

The stress field ahead of the penetrator-target interface can be approximated to have spherical symmetry. I model the alumina ceramic as an elastic-brittle material which cracks under tension and then pulverizes when the compressive stress exceeds the one-dimensional compressive failure strength. The implication of this assumption is depicted schematically in Figure 3.2, which shows three zones: the region near the cavity is comminuted; next to the comminuted zone (a.k.a. Mescall zone) there is a "radially cracked" zone (radial cracks are formed because the hoop stress exceeds the tensile strength); and beyond the "radially cracked" zone the material is elastic. This phenomenology is consistent with the observations by Collombet and Tranchet (1994) of explosive cavities in alumina (see Figure 3.3); they find "intergranular cracks" near the cavity, next to which "transgranular cracks" were found. The "transgranular cracks" are radially oriented, which implies that for spherical symmetry, the hoop stress is zero. In the "intergranular crack" region, the cracks are randomly oriented and are interconnected. Essentially, the material in this region is fragmented and comminuted. This sequence of failed regions around the cavity is generally consistent with measurements on aluminas penetrated by long rods (Shockey et al. 1990). Although there are some observations that the level of communition varies in the pulverized zone (Curran et al. 1993), I model the entire pulverized material as a Mohr-Coulomb material with a pressure dependent shear strength. The pressure-shear coefficient is derived from the uniaxial stress-shear coefficient experimentally obtained by Sairam and Clifton (1994).
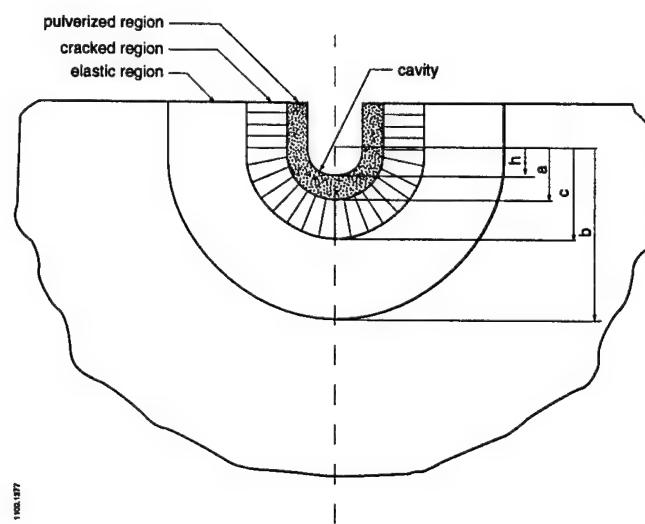
Figure 3.2. Response regions in the target.
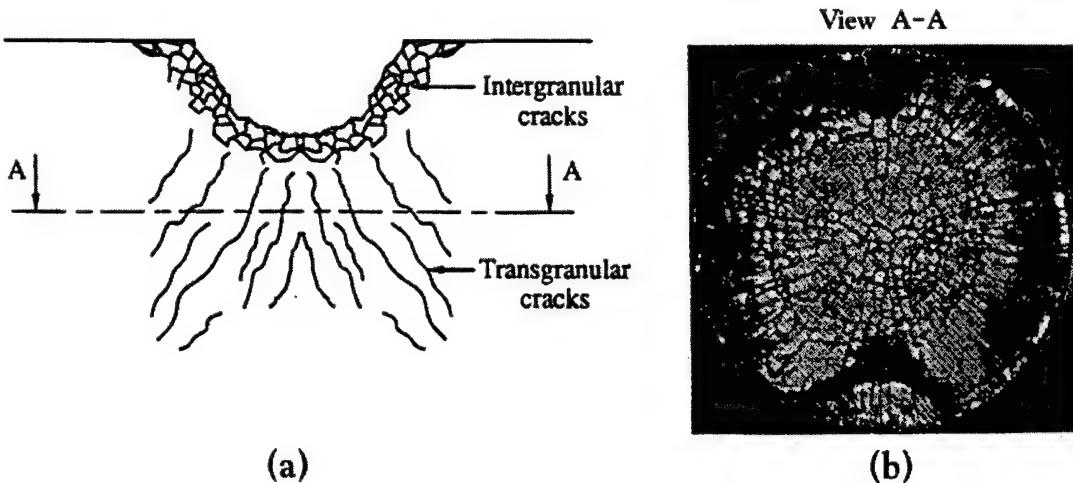
Figure 3.3 (a). Isotropic and anisotropic networks of cracks (b). Transgranular cracks in the soft recovered sample, Collombet and Tranchet (1994).

3.3.1.2   Elastic region

Referring to Figure 3.2, the elastic zone extends from $r = c$ to $r = b$ where b is the stress-free outer boundary of the target. At the cracked-elastic boundary the hoop stress equals the tensile strength of the material. Inertial terms are neglected, since R_t, by definition, does not include inertial effects. The stresses and strains are positive in tension. The field equations can be written as,

Equilibrium equation:
$$\frac{d\sigma_r}{dr} + 2\frac{\sigma_r - \sigma_\theta}{r} = 0, \tag{3.6}$$

Strain-displacement relation:
$$\varepsilon_r = \frac{du}{dr} \text{ and } \varepsilon_\theta = \varepsilon_\phi = \frac{u}{r}, \tag{3.7}$$

Constitutive relation for elastic region:
$$\varepsilon_r = \frac{1}{E}\left[\sigma_r - 2\nu\sigma_\theta\right] \tag{3.8}$$

$$\varepsilon_\theta = \varepsilon_\phi = \frac{1}{E}\left[(1-\nu)\sigma_\theta - \nu\sigma_r\right]. \tag{3.9}$$

Solving Eqs. (3.6) through (3.9), one obtains

$$u = c_1 r + \frac{c_2}{r^2}. \tag{3.10}$$

To evaluate c_1 and c_2, two boundary conditions are required, which are:

$$\sigma_r\big|_{r=b} = 0 \quad \text{and} \quad \sigma_\theta\big|_{r=c} = \sigma_f, \tag{3.11}$$

where σ_f is the tensile strength. Solving Eqs. (3.6) through (3.9) with Eq. (3.10) and the boundary conditions Eq. (3.11) yields

$$u = \frac{\sigma_f}{2E\left(1 + b^3/2c^3\right)}\left[(1 - 2v)r + (1 + v)b^3/r^2\right], \tag{3.12}$$

$$\sigma_r = \frac{\sigma_f}{\left(1 + b^3/2c^3\right)}\left[1 - b^3/r^3\right], \tag{3.13}$$

$$\sigma_\theta = \frac{\sigma_f}{\left(1 + b^3/2c^3\right)}\left[1 + b^3/2r^3\right]. \tag{3.14}$$

Evaluation of Eq. (3.7) along with Eq. (3.12) for b>>c yields the maximum strains in the elastic region as: $\varepsilon_r = 2\sigma_f(1+v)/E$ and $\varepsilon_\theta = \sigma_f(1+v)/E$. Since σ_f<<E for typical brittle materials, the use of small strain theory for the elastic region is justified. Expressions for the pressure (positive in compression) and the shear stress in this elastic region are given by:

$$P = -\frac{\sigma_f}{\left(1 + b^3/2c^3\right)}, \tag{3.15}$$

$$\frac{1}{2}\left|\sigma_r - \sigma_\theta\right| = \frac{3}{4}\frac{\sigma_f}{\left(1 + b^3/2c^3\right)}\frac{b^3}{r^3}. \tag{3.16}$$

3.3.1.3 Cracked region

As discussed before, the material will crack when the tensile hoop stress exceeds the tensile strength. Thus, the elastic region will be bounded inwardly by a radially cracked region $(a < r < c)$, within which the radial cracks are assumed to be of various sizes and spatially distributed in such a manner that the hoop stress in the whole region is zero. The inner boundary of this region is defined by the boundary condition that the material is pulverized. Since the stress state in the cracked region is uniaxial, pulverization occurs where the radial stress exceeds the uniaxial compressive strength, Y; i.e.,

$$\sigma_r\big|_{r=a} = -Y. \tag{3.17}$$

The stress and displacements are taken as volume-averaged quantities allowing for local variations. Since $\sigma_\theta = 0$, the equilibrium equation (3.6) reduces to,

$$\frac{d\sigma_r}{dr} + 2\frac{\sigma_r}{r} = 0, \tag{3.18}$$

which can be integrated with (3.17) to yield,

$$\sigma_r = -Y\frac{a^2}{r^2}. \tag{3.19}$$

Also, since the radial stress has to be continuous at the elastic-cracked boundary, $r = c$, then from (3.13) and (3.19),

$$\left(\frac{c}{a}\right)^2 = -\frac{Y}{\sigma_f}\frac{\left(1+\dfrac{b^3}{2c^3}\right)}{\left(1-\dfrac{b^3}{c^3}\right)}. \tag{3.20}$$

To evaluate displacement in the cracked region, Forrestal et al. (1990) used the equation of state with the bulk modulus of the intact material. But in fact, the presence of radial cracks will

render the material anisotropic. Thus, it is better not to use the isotropic elastic constants of the intact material to characterize the displacement of this anisotropic cracked region. However, absence of transverse cracks ensures no degradation of elastic moduli in the radial direction. Hence using (3.19) with the stress-strain relation in the radial direction, $\sigma_r = E\varepsilon_r = E\,du/dr$, displacement is given by,

$$u = \frac{Y}{E}\frac{a^2}{r} + A. \tag{3.21}$$

The constant A is evaluated by using continuity of displacement at $r = c$. Thus from (3.12) and (3.21), one obtains

$$u = \frac{\sigma_f}{2E\left(1 + \dfrac{b^3}{2c^3}\right)}\left[\frac{(1-2\nu)c^3 + (1+\nu)b^3}{c^2}\right] + \frac{Y}{E}\frac{a^2}{c}\left(\frac{c}{r}-1\right). \tag{3.22}$$

For b>>a, Eq. (3.22) gives the maximum strain in the cracked region as: $\varepsilon_r = -Y/E$. As before, since Y<<E, as well as σ_f<<E, use of small strain theory for the cracked region is justified. The pressure and shear stress in this region can be written as

$$P = \frac{Ya^2}{3r^2}, \tag{3.23}$$

$$\tau = \frac{1}{2}\left|\sigma_r - \sigma_\theta\right| = \frac{Ya^2}{2r^2}. \tag{3.24}$$

3.3.1.4 Comminuted region

I model the entire pulverized material as a Mohr-Coulomb material with a pressure dependent shear strength. The pressure-shear coefficient is derived from the uniaxial stress-shear coefficient experimentally obtained by Clifton et al. (1995) for AD995 alumina and by Curran et al. (1993) for AlN.

The shear stress in the comminuted region ($h < r < a$) is set equal to the "flow stress," which is taken as pressure dependent (linear portion, O-F, of the lower curve in Figure 3.1). Thus,

$$\frac{\sigma_r - \sigma_\theta}{2} = m\left(\frac{\sigma_r + 2\sigma_\theta}{3}\right). \tag{3.25}$$

The equilibrium equation (3.6) reduces to

$$\frac{d\sigma_r}{dr} + 2\bar{\alpha}\frac{\sigma_r}{r} = 0, \tag{3.26}$$

where $\bar{\alpha} = \dfrac{6m}{3 + 4m}$. \hfill (3.27)

With the boundary condition (3.17), (3.26) can be solved to yield

$$\sigma_r = -Y\left(\frac{a}{r}\right)^{2\bar{\alpha}}. \tag{3.28}$$

The target resistance, R_t, which is the negative of the radial stress at the cavity boundary, $r = h$, is thus found to be

$$R_t = Y\left(\frac{a}{h}\right)^{2\bar{\alpha}}. \tag{3.29}$$

Finally, the pressure and the shear stress in the comminuted region can be calculated as

$$P = Y\left(\frac{a}{r}\right)^{2\bar{\alpha}}\frac{3 - 2\bar{\alpha}}{3}, \tag{3.30}$$

$$\tau = \frac{1}{2}|\sigma_r - \sigma_\theta| = \frac{1}{2}\bar{\alpha}Y\left(\frac{a}{r}\right)^{2\bar{\alpha}}. \tag{3.31}$$

3.3.1.5 Calculation of h/a

From (3.29), note that to solve for R_t, one needs to evaluate the size of the pulverized zone relative to the cavity size. Even though this ratio turns out to be a constant, independent of geometry for an infinite target, I first derive its value for a finite target. Thus far I have avoided using any constitutive relation for the comminuted region. In the previous section, the equation of motion was integrated with the assumption that the shear stress varies linearly with pressure in this region (Mohr-Coulomb criterion). Even if statistical homogeneity is assumed, the elastic moduli may be different from those of the intact material. Presence of bulking due to comminution complicates the problem further, due to the competition between dilatancy and pore compaction. Curran et. al. (1993) observed that dilatancy occurs only after the large compressive stress has disappeared. In this work, I assume that the dilatancy and compaction cancel out at least to a first order approximation, and so there is no volume change in the comminuted region. From the conservation of mass, and ignoring higher order terms in $u(a)$,

$$\frac{1}{3}\left(\frac{h}{a}\right)^3 = \frac{u(a)}{a}.$$ (3.32)

Since the radial displacement has to be continuous at $r = a$, $u(a)$ is given by (3.22). Thus,

$$\frac{1}{3}\left(\frac{h}{a}\right)^3 = \frac{\sigma_f}{2E\left(1+\frac{b^3}{2c^3}\right)}\left[\frac{(1-2v)c^3+(1+v)b^3}{c^2a}\right]+\frac{Y}{E}\left(1-\frac{a}{c}\right)$$ (3.33)

Equations (3.33) and (3.20) have two unknowns, c and a. For a given geometry (h and b known), these two equations can be solved for "a", and the cavity expansion pressure, R_t, can be calculated.

3.3.1.6 Infinite target

For an infinite target (i.e., b is very large), the RHS of (3.33) is a function of only c/a which can be evaluated from (3.20). Thus, the ratio h/a and hence R_t is determined purely from the material constants. By letting $b \rightarrow \infty$, one derives:

67

$$R_t = Y \left[\frac{\left(\dfrac{E}{3Y}\right)}{1 - \sqrt{\dfrac{\sigma_f}{Y} \dfrac{(1-\nu)}{\sqrt{2}}}} \right]^{-\frac{2\overline{\alpha}}{3}}. \tag{3.34}$$

3.3.1.7 Material constants for Coors AD995 alumina and AlN

The elastic constants for Coors AD995 alumina are calculated from the longitudinal and transverse wave speeds reported by Grady (1995) as $E = 373.14$ GPa, $K = 231.8$ Gpa, $\rho = 3890$ kg/m^3. The quasi-static strength parameters as published by Coors are: compressive strength, $Y = 2.62$ GPa; and tensile strength $\sigma_f = 0.262$ GPa. Simha, et al. (1995) measured the compressive strength of AD995 alumina from bar impact tests; it varied from 2.6 GPa to 3 GPa. Bar impact tests of similar alumina give intermediate results, as shown by Brar, et al. (1988) and Cosculleula (1992). Dandekar and Bartkowski (1993) measured the spall strength of this alumina as 0.462 GPa. To bound results for R_t, I use two values for the compressive strength, Y: 2.6 GPa and 3 GPa. A tensile strength of 0.462 GPa is used. Finally, calculation of the pressure-shear coefficient, m, is based on Clifton's (1995) and Curran et al.'s (1993) experimental value of normal stress vs. shear stress coefficient, μ_s as follows.

Let $\quad \dfrac{1}{2}(\sigma_r - \sigma_\theta) = \mu_s \sigma_r.$ \hfill (3.35)

Therefore, m is given by:

$$m = \frac{(\sigma_r - \sigma_\theta)/2}{(\sigma_r + 2\sigma_\theta)/3} = \frac{3\mu_s}{3 - 4\mu_s}. \tag{3.36}$$

From Clifton's (1995) measured value of $\mu_s = 0.2$, one obtains, m = 0.273 for AD995 alumina.

The following properties are used for AlN. From Curran, et al.(1993): $K = 210$ GPa, $E = 315$ GPa, $Y = 3$ GPa, $\sigma_f = 1$ GPa, $\mu_s = 0.163$ and hence m = 0.208.

3.3.1.8   Conservation of mass

It must be shown that mass is conserved in the cracked region. The average density of the material in the cracked region is given by

$$\bar{\rho} = \left\{ \frac{4}{3}\pi\rho_o \left[[c - u(c)]^3 - [a - u(a)]^3 \right] \Big/ \left[\frac{4}{3}\pi(c^3 - a^3) \right] \right\},$$
(3.37)

where ρ_o is the initial density. $u(a)$, $u(c)$ and (c/a) are given by equations (3.22), (3.13) and (3.20), respectively. For an infinite target, evaluating these expressions for $b \rightarrow \infty$, and inserting them in (3.37) gives,

$$\bar{\rho} = \frac{\rho_o \left\{ \left[1 - \frac{\sigma_f}{E}(1+v) \right]^3 - \left[\sqrt{\frac{2\sigma_f}{Y}} - \frac{\sigma_f}{E}\left(\sqrt{\frac{Y}{2\sigma_f}} - 1 \right) \right]^3 \right\}}{1 - \left(\frac{2\sigma_f}{Y} \right)^{3/2}}.$$
(3.38)

Denoting ρ_c as the density of the ceramic material in the cracked region,

$$\frac{\rho_c}{\rho_o} = 1 + \frac{P}{K}.$$
(3.39)

Using the elastic relation in the radial direction, from (3.23) and (3.39),

$$\rho_c = \rho_o \left[1 + \frac{Y}{3K}\frac{a^2}{r^2} \right].$$
(3.40)

69

Evaluation of (3.38) and (3.39) for AD995 ceramic, gives $\bar{\rho} = 0.9977 \, \rho_o < \rho_c(c) = 1.0008 \, \rho_o$. Since ρ_c is a decreasing function of r, it follows that $\rho_c > \bar{\rho}$ for $a < r < c$, which is consistent with the assumption that the region is cracked. Similarly, for AlN, $\bar{\rho} = 0.9786 \, \rho_o < \rho_c(c) = 1.002 \, \rho_o$, which does not violate mass conservation.

3.3.1.9 Results

R_t for an infinite target of AD995 alumina is plotted as a function of the pressure shear coefficient, m, in Figure 3.4. For m = 0.273 (from Clifton's data), it turns out that $R_t = 7.7$ GPa for $Y = 2.62$ GPa, and $R_t = 8.6$ GPa for $Y = 3$ GPa. Subramanian and Bless (1994) conducted penetration experiments on AD995 targets with tungsten penetrators and found that R_t is scattered from 7 GPa to 9 GPa and that solution corresponding to a R_t of 8.5 GPa passes through almost all the error bars for the experimental values. Thus, the closed form solution has resulted in R_t values that tightly bracket the experimental observation. Similarly for AlN, Curran et al.'s (1993) material data imply that $R_t = 7$ GPa, which agrees with the average value of experimental data obtained by Orphal et al.(1996) (their experimental R_t value ranged from 5 GPa to 9 GPa, while most of the data points were clustered about an R_t of 7 GPa).
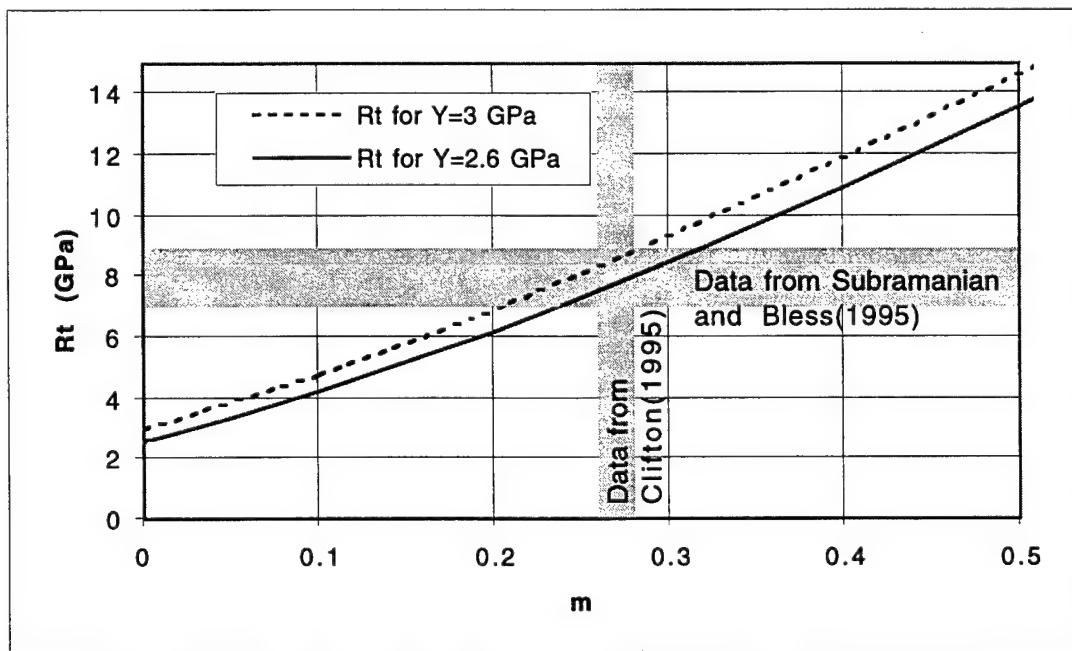
Figure 3.4. Variation of R_t with pressure-shear coefficient, m for AD995.

The radial stress and the hoop stress for AD995 alumina are plotted as functions of normalized radius (r/h) in Figure 3.5. It can be seen that the pulverized zone and the cracked zone extend to about 3.5 and 9 times the cavity size, respectively. The stresses fall off to zero asymptotically beyond r/h > 15. Thus the assumption of an infinite target is valid if the target to penetrator diameter ratio is at least 15. This is consistent with radial confinement effects as reported by Bless et al. (1995).
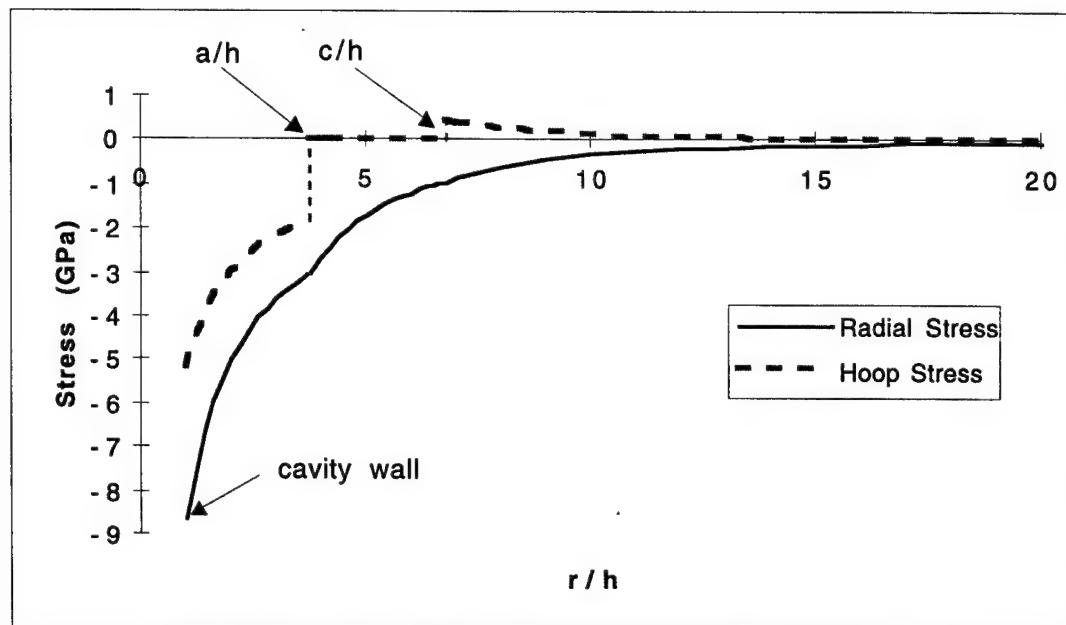
Figure 3.5. Variation of stresses with normalized radius, r/h.

In Figure 3.6 pressure vs. shear stress in the various regions is plotted. It depicts the path taken by a virgin material element as the penetrator approaches and the cavity pressure starts to build up. The following discussion compares the pressure-shear constitutive behavior (Figure 3.6) depicted by the above analysis with the general pressure-shear constitutive behavior described in Figure 3.1. Figure 3.6 indicates that the loading path of the material starts out at the origin in Figure 3.1. Since the pressure in the elastic region is zero, the material loads along "O-C". When the tensile strength is exceeded, radial cracks appear. Thus the material jumps to a point on the 1-D stress path "O-D". In the cracked region, radial cracks make the structure of the material needle-like which justifies the assumption of 1-D stress path. Along this path, the maximum stress occurs at point "D", where the material further fails and jumps to the failure (lower) curve, "O-F". Since the loading path has touched the upper curve only at one point, no assumption was required regarding the shape of the upper curve. This is an important result of this analysis, since it

indicates that high pressure dependence of the fracture strength (upper curve) of ceramics does not affect penetration resistance.
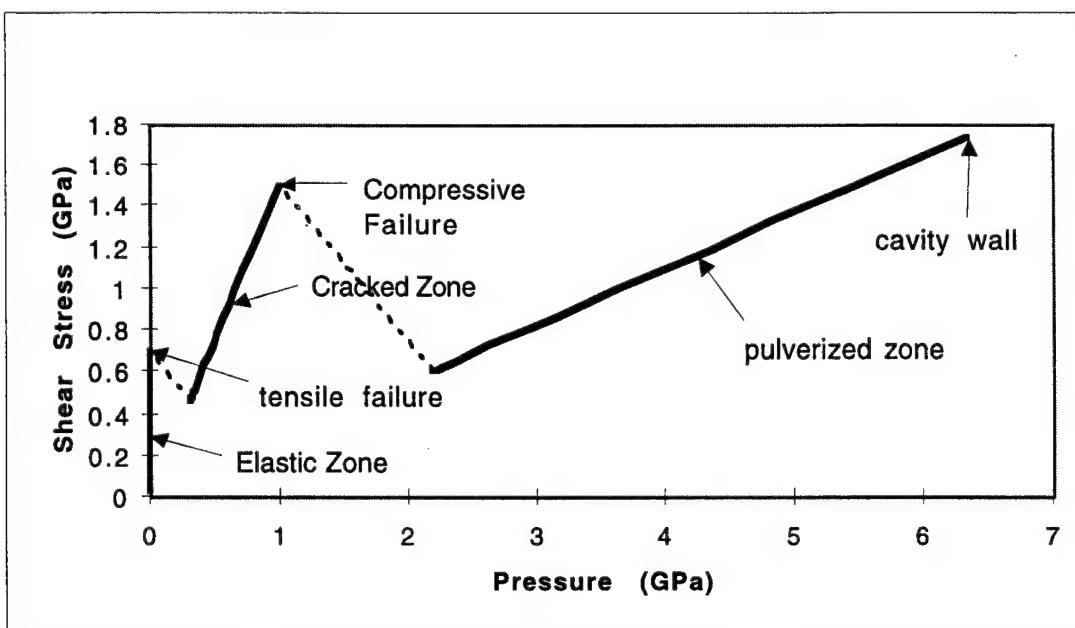
Figure 3.6. Shear stress vs. pressure in different zones.

After compressive fracture, the material follows the linear portion of the lower curve. In the above analysis, the shear saturation of the lower curve (F-G) was not considered. Neglect of the limiting shear strength of failed material is justified by the following argument. The maximum pressure and shear experienced by the failed material is at the cavity wall and is given by Eqs. (3.30) and (3.31) with $r = h$. Evaluation of these expressions for $Y = 3$ GPa yields $P_{max} = 6.3$ GPa and $\tau_{max} = 1.72$ GPa. From Figure 3.1 P(F) and S(F) are related by $P(F) = S(F)/\mu$. High pressure plate impact tests on AD85 ceramic (Rosenberg et al. 1987) suggests that the shear stress behind the shock wave saturates for a shock pressure which is slightly above the HEL. The saturated shear stress is reported as 2.7 GPa for this material. There are other tests (Cosculleula 1992) which show that the HEL of AD85 ceramic involves extensive microcracks, which begin at the glass inclusions. The shear strength of the material behind the shock wave is maintained at a constant level for other alumina ceramics as well (Arhens, 1968). Similar material behavior should hold for AD995 alumina ceramic. The state of the material immediately behind the shock wave may not be fully failed. Thus, this value is an overestimate of the saturated shear strength of the fully failed material. On the other hand, the shear stress at the HEL for AD995 is 2.23 GPa (HEL = 6.2 GPa). This should be a conservative estimate of the

72

shear strength of the failed material. Use of the above two representative values for the shear stress levels yield the pressure levels for P(F) of 13.5 GPa and 11.13 GPa respectively, for $\mu_s = 0.2$. Thus the maximum shear stress and maximum pressure experienced in the cavity expansion are well below the saturation levels. Thus ignoring the saturation limit in the analysis is justified.

In Figure 3.7, the pressure-shear plot of the present analysis is compared with those from Forrestal and Longcope (1990) and Partom (1993). The plots from Forrestal and Longcope and the current analysis are identical in the elastic and cracked regions. In the "plastic" region of Forrestal and Longcope's analysis, the pressure-shear plot follows the upper curve for the intact material. On the contrary, in the present analysis, the material follows the lower curve for the failed material in the comminuted region. The pressure-shear plot from Partom's analysis is plotted for a lower curve slope of 1, which gives a cavity expansion pressure comparable to experimental value for AD995. This model does not account for the excess of tensile hoop stress at the inner boundary of the elastic region, as discussed earlier. Thus, from this comparison it is evident that the present analysis alone accounts for both the upper curve for intact material and the lower curve for the failed material. The cavity expansion pressure derived in the present analysis shows much better agreement with the experimental value of penetration resistance than the other two models.
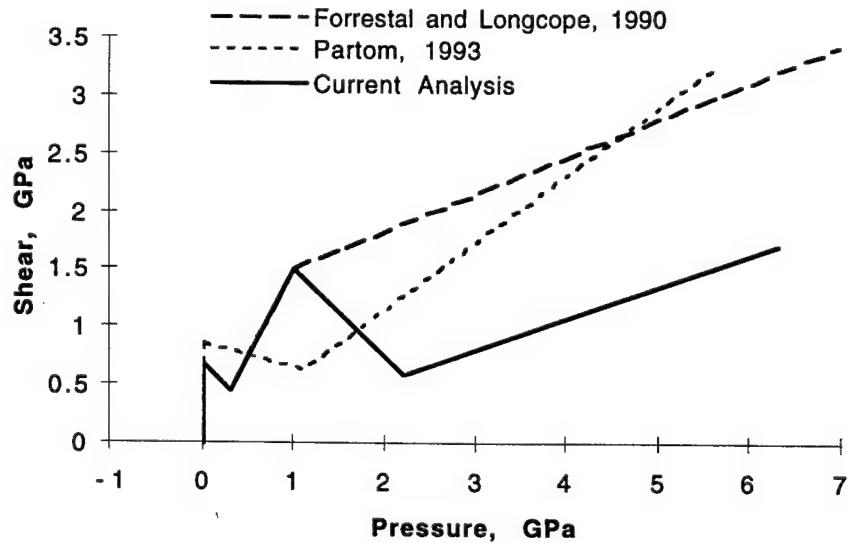
Figure 3.7. Comparison of different models.

73

3.3.1.10 Sensitivity Study

The solution procedure provides useful insight into the properties of ceramics that most influence the penetration resistance. It has succeeded in explaining the low value of target resistance, R_t for AD995 alumina and AlN. Even though there is an uncertainty of about 0.4 GPa in the compressive strength, this does not cause R_t to vary beyond the experimentally observed range. The analysis used an average value of the pressure-shear coefficient (m) in the comminuted zone equal to those measured by Clifton (1995) for AD995 alumina and by Curran et al. (1993) for AlN. It is not known whether or not m varies with the degree of comminution or even whether or not the degree of comminution is uniform in the Mescall zone. As seen in Figure 3.4, a plausible 10% perturbation in the experimentally measured value of m produces about 10% perturbation in the R_t value, which will still lie within the experimental scatter. R_t is found to be quite insensitive to variation in the tensile strength value near its experimentally measured value. For example a 100% change in the tensile strength value causes only about a 5% change in R_t .

For the pulverized zone, I assumed that to a first order approximation, the compression due to high pressure and the dilatancy due to comminution cancel out each other so that the density in this region remains constant. It is found that a net dilatancy due to comminution would raise the R_t value rapidly. However, plate impact experiments for Al_2O_3 ceramics (Arhens et al. 1968) show that above the HEL, when the material is microfractured, the shock Hugoniot is parallel to the extrapolated hydrostat, which strongly suggests negligible dilatancy. Shock data for AlN (Rosenberg et al. 1991) are difficult to interpret in this respect because of probable phase change(Kipp and Grady 1994). Curran et al. (1993) also found that dilatancy would occur only after unloading. Thus the presence of large scale bulking before passage of the penetrator can be ruled out. On the other hand, a decrease in volume would lower the R_t value. However, at the maximum possible compressibility (treating the material as an uncomminuted elastic ceramic), R_t values reduce by less than 10%, which is again within the experimental scatter of R_t. Therefore, I believe that the final density of the comminuted material must lie close to its original value, and hence the no-volume-change assumption holds good.

In summary, the model is found to explain the observed R_t values. The approximations that I made, should not affect this conclusion. The model demonstrates that the properties of the comminuted material (pressure-shear coefficient and its width, which is dependent on other material constants) are very important in determining the penetration resistance. The shape of the

upper curve in Figure 3.1 (the pressure dependence of fracture curve) does not affect the penetration resistance. Only the compressive strength (obtainable from bar impact tests) has a great bearing on R_t. Effects of tensile strength is minimal.

3.3.2 Cylindrical cavity expansion

The spherical cavity expansion solution described in the previous section identified the important material properties of brittle ceramics that affect penetration resistance. The excellent agreement of the spherical cavity expansion pressure with experimental values of R_t for long rod penetration suggests that a cylindrical cavity expansion solution can be used to derive the penetration resistance value for plane-strain penetration, as suggested by Bless (1995). The cylindrical cavity expansion solution may be used to indicate the lateral confinement required to minimize cracking in brittle ceramics.

The cavity expansion solution for cylindrical symmetry is similar to that for spherical symmetry. However, for cylindrical symmetry, some assumption needs to be introduced regarding the axial stress or axial strain. In the following, I show derivations for both plane stress ($\sigma_z = 0$) and plane strain ($\varepsilon_z = 0$) conditions for cavity expansion in an infinite material. The field equations for cylindrical symmetry are:

Equilibrium equation:
$$\frac{d\sigma_r}{dr} + \frac{\sigma_r - \sigma_\theta}{r} = 0 \qquad (3.41)$$

Strain-displacement relation:
$$\varepsilon_r = \frac{du}{dr} \text{ and } \varepsilon_\theta = \frac{u}{r} \qquad (3.42)$$

Constitutive relation for plane stress:
$$\varepsilon_r = \frac{1}{E}\left[\sigma_r - \nu\sigma_\theta\right] \qquad (3.43)$$

$$\varepsilon_\theta = \frac{1}{E}\left[\sigma_\theta - \nu\sigma_r\right] \qquad (3.44)$$

75

Constitutive relation for plane strain:
$$\varepsilon_r = \frac{(1+v)}{E}\left[\sigma_r(1-v)-v\sigma_\theta\right] \quad (3.45)$$

$$\varepsilon_\theta = \frac{(1+v)}{E}\left[\sigma_\theta(1-v)-v\sigma_r\right] \quad (3.46)$$

since $\sigma_z = v(\sigma_r + \sigma_\theta)$ for plane strain.

Substituting the constitutive relations and the strain-displacement relations into the equilibrium equation, for either plane stress or plane strain conditions one obtains:

$$u = c_1 r + \frac{c_2}{r}. \quad (3.47)$$

To evaluate c_1 and c_2 two boundary conditions are needed, which are

$$\sigma_r\big|_{r=\infty} = 0, \quad \text{and} \quad \sigma_\theta\big|_{r=c} = \sigma_f. \quad (3.48)$$

Solving Eqs. (3.41) through (3.46) with Eq. (3.47) and the boundary conditions Eq. (3.48) yields

$$u = \frac{\sigma_f(1+v)}{E}\frac{c^2}{r} \text{ for plane stress and } u = \frac{\sigma_f(1+v)}{2E}\frac{c^2}{r} \text{ for plane strain,} \quad (3.49)$$

$$\sigma_r = -\sigma_f\frac{c^2}{r^2} \text{ for plane stress and } \sigma_r = -\frac{\sigma_f}{2}\frac{c^2}{r^2} \text{ for plane strain.} \quad (3.50)$$

Since the stress state in the cracked region is uniaxial, pulverization occurs where the radial stress exceeds the uniaxial compressive strength, Y; i.e.,

$$\sigma_r\big|_{r=a} = -Y. \quad (3.51)$$

Since in the cracked region, $\sigma_\theta = 0$, the equilibrium equation (3.41) reduces to

$$\frac{d\sigma_r}{dr} + \frac{\sigma_r}{r} = 0, \quad (3.52)$$

76

which can be integrated with (3.42) to yield

$$\sigma_r = -Y\frac{a}{r}.$$ (3.53)

Also, since the radial stress has to be continuous at the elastic-cracked boundary, r = c, from (3.50) and (3.53),

$$\frac{c}{a} = \frac{Y}{\sigma_f} \text{ for plane stress and } \frac{c}{a} = \frac{2Y}{\sigma_f} \text{ for plane strain.}$$ (3.54)

Using continuity of displacement at r = c, the displacement can be expressed as

$$u = \frac{Y}{E}a\left(\ln\frac{c}{r} + 1 + v\right) \text{ for either plane stress or plane strain}$$ (3.55)

The shear stress in the comminuted region (h < r < a) is equal to the "flow stress," which is taken as pressure dependent. Thus, writing $\frac{\sigma_r - \sigma_\theta}{2} = m\left(\frac{\sigma_r + \sigma_\theta}{3}\right)$ for plane stress and $\frac{\sigma_r - \sigma_\theta}{2} = m(1+v)\left(\frac{\sigma_r + \sigma_\theta}{3}\right)$ for plane strain, the equilibrium equation (3.41) reduces to

$$\frac{d\sigma_r}{dr} + 2\overline{\alpha}\frac{\sigma_r}{r} = 0,$$ (3.56)

where: $\overline{\alpha} = \frac{4m}{3+2m}$ for plane stress and $\overline{\alpha} = \frac{4m(1+v)}{3+2m(1+v)}$ for plane strain. (3.57)

With the boundary condition (3.51), (3.56) can be solved to yield

$$\sigma_r = -Y\left(\frac{a}{r}\right)^{\overline{\alpha}}.$$ (3.58)

The cavity expansion pressure, P_c, which is the negative of the radial stress at the cavity boundary, $r = h$, is thus found to be

$$P_c = Y\left(\frac{a}{h}\right)^{\bar{\alpha}}. \qquad (3.59)$$

For an incompressible comminuted region, volume conservation yields

$$\frac{1}{2}\left(\frac{h}{a}\right)^2 = \frac{u(a)}{a}. \qquad (3.60)$$

Evaluating $u(a)/a$ from the cracked region solution, Eqs. (3.54) and (3.55), the cavity expansion pressure for an infinite target is given by

$$P_c = Y\left[\frac{(E/2Y)}{1+v+\ln(Y/\sigma_f)}\right]^{\frac{\bar{\alpha}}{2}} \text{ for plane stress and}$$

$$P_c = Y\left[\frac{(E/2Y)}{1+v+\ln(2Y/\sigma_f)}\right]^{\frac{\bar{\alpha}}{2}} \text{ for plane strain.} \qquad (3.61)$$

For AD995 with $\mu_s = 0.2$, the cavity expansion pressure for plane stress and plane strain conditions are 5.47 GPa and 5.25 GPa, respectively, which are about 35% less than the average experimental value of penetration resistance for long rod case. Thus the spherical cavity expansion pressure is a better approximation to the penetration resistance (for long rods) of ceramic materials than the cylindrical cavity expansion pressure. On the other hand, this calculation indicates that planar penetrators (Bless 1996) would penetrate better than long rods, since a cylindrical cavity expansion pressure is applicable for the former, whereas spherical cavity expansion pressure is applicable for the later.

3.4 Dynamic spherical cavity expansion in a brittle material

In the static analysis of the previous sections, it was assumed that the penetration resistance, R_t, is given by only the static-cavity expansion pressure. This assumption leads to a condition of no velocity dependence of the penetration resistance term. When using this derived value, the velocity dependence is described by the dynamic term in the Tate equation (Eq. 2.72). The Tate equation equates the stress in the penetrator and the stress in the target at the penetrator-target interface. Even though the Tate equation (Eq. 2.72) correctly models the one-dimensional stress state of the projectile, it does not consider the effect of the 3-D state of stress in the target since the inertial term (i.e., velocity dependence) is based on 1-D relationship. A more consistent approach would be to model dynamic effects in the target, which could allow calculation of the complete RHS of the Tate equation. Cavity expansion analysis presents a framework by which the effects of 3-D states of stress in the target can be incorporated into a pressure-balance approach as in the Tate equation. However, to adapt the cavity expansion solution for a linear penetration problem, the relationship between the cavity expansion speed and the linear penetration speed must be established.

In the following, I first solve the dynamic cavity expansion problem for a constant cavity expansion velocity using a steady-state elastic-wave propagation solution. This approximate solution considers only a linear behavior for the failed material (no shear saturation) and does not admit a jump in radial stress at the cracked-comminuted boundary. Subsequently, I solve the same problem using self-similarity transformations, where implications of shear saturation are considered and the necessary jump conditions are satisfied. The cavity expansion velocity is related to the linear penetration velocity, and the cavity expansion pressure is compared to experimental data for linear penetration.

3.4.1 Dynamic cavity expansion solution using elastic-wave theory

As detailed for the quasi-static analysis, the alumina ceramic is modeled as an elastic material that cracks under tension and then pulverizes when the compressive stress exceeds the one-dimensional compressive failure strength. The equation of motion in Eulerian spherical coordinates is written as

$$\frac{\partial \sigma_r}{\partial r} + \frac{2}{r}(\sigma_r - \sigma_\theta) = \rho\left(\frac{\partial v}{\partial t} + v\frac{\partial v}{\partial r}\right), \tag{3.62}$$

where v is the particle velocity. The mass conservation equation is written as

$$\frac{\partial \rho}{\partial t} + \frac{1}{r^2} \frac{\partial}{\partial r} \left(\rho r^2 v \right) = 0. \tag{3.63}$$

For steady-state motion, assuming no volume change in the comminuted region, and recognizing that $v = \dot{h}$ at $r = h$, Eq. (3.63) reduces to

$$v = \frac{h^2 \dot{h}}{r^2}. \tag{3.64}$$

Inserting the post-failure strength behavior, Eq. (3.25) and Eq. (3.64) into Eq. (3.62), one obtains,

$$\frac{\partial \sigma_r}{\partial r} + 2\overline{\alpha} \frac{\sigma_r}{r} = \rho \left(\frac{h^2 \ddot{h} + 2h\dot{h}^2}{r^2} - \frac{2h^4 \dot{h}^2}{r^5} \right). \tag{3.65}$$

Equation (3.65) is readily integrated to obtain the stress distribution in the comminuted region as

$$\sigma_r = -\rho \left[\frac{1}{1-2\overline{\alpha}} \frac{h^2 \ddot{h} + 2h\dot{h}^2}{r^2} - \frac{2h\dot{h}^2}{(2-\overline{\alpha})r^5} \right] + \frac{c_1}{r^{2\overline{\alpha}}}, \tag{3.66}$$

where c_1 is the integration constant. The cracked region begins at $r = a$. Since at the cracked-pulverized interface, $r = a$, pulverization occurs when $\sigma_r = - Y$, c_1 can be solved for. The radial stress distribution is thus given by

$$\sigma_r = -\rho \left[\frac{h^2 \ddot{h} - 2h\dot{h}^2}{(1-2\overline{\alpha})r} - \frac{2h^4 \dot{h}^2}{(2-\overline{\alpha})r^4} - Y \left(\frac{a}{h} \right)^{2\overline{\alpha}} \right] + \rho \left(\frac{a}{h} \right)^{2\overline{\alpha}} \left[\frac{2h^2(h/a)}{1-2\overline{\alpha}} - \frac{\dot{h}^2}{2-\overline{\alpha}} \left(\frac{h}{a} \right)^4 \right]. \tag{3.67}$$

In long rod penetration experiments (Subramanian and Bless 1995) $\dot{h}$ is essentially constant. Thus, $\ddot{h}$ can be neglected. By definition, $h/a < 1$; hence $(h/a)^4$ can be neglected too. Evaluation of Eq. (3.67) at $r = h$ yields the steady-state cavity expansion pressure as

$$P_c = Y\left(\frac{a}{h}\right)^{2\bar{\alpha}} + \rho\dot{h}^2\left[\frac{3}{(1-2\bar{\alpha})(2-\bar{\alpha})} - \frac{2}{1-2\bar{\alpha}}\left(\frac{a}{h}\right)^{2\bar{\alpha}-1}\right]. \tag{3.68}$$

Even without further analysis, it is evident that the steady-state cavity expansion pressure is determined by the Mescall zone size and the pressure-shear behavior of post-fractured material. Incidentally, Eq. (3.68) reduces to the static cavity expansion solution (3.29) when $\dot{h} = 0$. Obviously, the size of the Mescall zone depends on the mechanics of the "radially cracked" zone and the elastic region beyond it.

For the "radially cracked" region, the equation of motion reduces to

$$\frac{\partial\sigma_r}{\partial r} + \frac{2\sigma_r}{r} = \rho\frac{\partial^2 u}{\partial t^2}, \tag{3.69}$$

where $\partial u/\partial t$ is the particle velocity. The isotropic elastic constants are not applicable in this region due to the anisotropy introduced by the presence of radial cracks. However, as discussed in Section 3.3.1.3, absence of transverse cracks ensures no degradation of the elastic moduli in the radial direction. Hence, using $\sigma_r = E\,\partial u/\partial r$ in Eq. (3.69), one obtains,

$$\frac{\partial^2 u}{\partial r^2} + \frac{2}{r}\frac{\partial u}{\partial r} = \frac{1}{c_c^2}\frac{\partial^2 u}{\partial t^2}, \tag{3.70}$$

where $c_c = \sqrt{(E/\rho)}$. Equation (3.70) is a wave equation which has a solution of the form

$$u = \frac{1}{r}\left[f(r - c_c t) + g(r + c_c t)\right]. \tag{3.71}$$

The first term in Eq. (3.71) represents a divergent propagating wave and the second one is a convergent reflected wave. Since the acoustic impedance on either side of the elastic-radially cracked boundary is essentially the same, the reflected wave can be neglected. Thus, the displacement is propagated without any dispersion but attenuates as $1/r$. Introducing a variable change, displacement can be expressed as $u = F(\tau)/r$ where $\tau = t - (r - a)/c_c$. $\tau = 0$ at the wave front, i.e., at $r = a + c_c t$ and $\tau = t$ at the cracked-pulverized boundary. Using the inner boundary condition at $r = a$, $\sigma_r = E \, \partial u / \partial r = -Y$,

$$F'(t) + F(t) \frac{c_c}{a} = \frac{Y c_c a}{E}. \tag{3.72}$$

The solution of this equation is given by

$$F(t) = c_1 \exp(-c_c t / a) + Y a^2 / E. \tag{3.73}$$

For AD 995 alumina, $c_c \sim 9.5$ km/s, which is consistent with the experimentally measured speed of the failure front[1] in this material (Strassburger et al. 1994). Existence of a failure front has been established in glass[2] (Bless et al. 1992). These observations lend additional credence to the cracking behavior assumed in this analysis. The wave in the cracked front is highly over-damped because of a high value of wave speed compared to the time of penetration and the pulverized zone size. By simply replacing t by τ, an expression for displacement in the cracked region is,

$$u(\tau) = \frac{c_1}{r} \exp(-c_c \tau / a) + \frac{Y a^2}{Er}. \tag{3.74}$$

For the outer elastic region, $(r > c)$, using the elastic stress-strain relationship, the equation of motion, Eq. (3.62) reduces to

$$\frac{\partial^2 u}{dr^2} + \frac{2}{r} \frac{\partial u}{\partial r} - \frac{2u}{r^2} = \frac{1}{c_e^2} \frac{\partial^2 u}{\partial t^2}, \tag{3.75}$$

---

[1] A failure front in brittle materials like glass is a wave front behind which material is extensively damaged. Speed of a failure front in glass is about half the Raleigh wave speed (Bless et al. 1992). Strassburger et al. measured the speed of an extensively damaged zone by impacting ceramic plates edge-on. This is essentially a plane-stress condition; thus, this failure speed may not be similar to what has been observed in glass.

[2] Failure fronts in polycrystalline ceramics is a topic of current research (IAT-Russian project: Bless 1997).

where $c_e^2 = \dfrac{E(1-v)}{\rho(1+v)(1-2v)}$ is the elastic dilatational wave speed. Since for pressure loading in spherical symmetry the motion is irrotational, the displacement can be expressed in terms of a scalar potential gradient as

$$u = \frac{\partial \phi}{\partial r}.$$ (3.76)

Inserting Eq. (3.76) into Eq. (3.75), it can be shown that ϕ satisfies the one-dimensional spherical wave equation:

$$\left(\nabla^2 - \frac{1}{c_e^2} \frac{\partial}{\partial t^2} \right) \phi = 0,$$ (3.77)

where $\nabla^2 \equiv \dfrac{1}{r^2} \dfrac{\partial}{\partial r} \left(r^2 \dfrac{\partial}{\partial r} \right)$. Given a pressure boundary condition, Eq. (3.77) can be solved by transform methods as discussed by Hopkins (1960) and Graff (1975). For the case of constant radial stress at $r = a$ $(\sigma_r = -Y)$, the displacement, u, can be expressed as

$$u(r,t) = \frac{a^3 Y}{4\mu r^2} \left[1 - e^{-\varsigma \tau} \left\{ \left(\frac{2r}{a} - 1 \right) \frac{\varsigma}{\omega} \sin \omega \tau - \cos \omega \tau \right\} \right],$$ (3.78)

where $\varsigma = \dfrac{2c_s^2}{ac_e}$; $\omega = \varsigma \left\{ \left(c_s^2 / c_e^2 \right) - 1 \right\}^{1/2}$ with c_s and c_e being dilatational and shear wave speeds, respectively, in the medium and μ is the shear modulus.

Since the value of ς is high, the motion in the elastic region is almost deadbeat. For the purpose of calculating size of the pulverized zone, I assume a steady state value of u in the elastic region, namely,

$$u^{elastic} = \frac{a^3 Y}{4\mu r^2}.$$ (3.79)

Now to calculate the constant c_1 in Eq. (3.74), equate the particle displacements at $r = c$; thus using $\tau = 0$ (at the wave front), Eqs. (3.74) and (3.79) yield

$$u^{cracked} = \frac{Ya^3}{4\mu c} \frac{e^{-c_c\tau/a}}{r} - \frac{Ya^2}{Er}\left(e^{-c_c\tau/a} - 1\right).$$

(3.80)

The last step is to apply the incompressibility condition of the pulverized region along with the condition of expansion from zero radius to get

$$\frac{1}{3}\left(\frac{h}{a}\right)^3 = \frac{u^{cracked}(a)}{a}$$

(3.81)

Therefore, from Eqs. (3.80) and (3.81), neglecting the over-damped time-dependent part (i.e., considering the steady state value),

$$\frac{1}{3}\left(\frac{h}{a}\right)^3 = \frac{Y}{E}$$

(3.82)

Thus, inserting Eq. (3.82) into Eq. (3.68), the steady-state cavity expansion pressure becomes

$$P_c = Y\left(\frac{E}{3Y}\right)^{2\bar{\alpha}/3} + \rho\dot{h}^2\left[\frac{3}{(1-2\bar{\alpha})(2-\bar{\alpha})} - \frac{2}{1-2\bar{\alpha}}\left(\frac{E}{3Y}\right)^{\frac{2\bar{\alpha}-1}{3}}\right].$$

(3.83)

Equation (3.83) is in form of $P_c = A + BV^2$. This is a Poncelet type equation discussed in Chapter 2. P_c should be used to give the total pressure at the penetrator-target interface. The terms in the square bracket in the RHS should give the coefficient of the dynamic term (which is 0.5 in Tate equation). Eq. (3.83) suggests that the important material parameters that determine the penetration resistance are: Y, E and α.

3.4.1.1 Comparison with data

As discussed earlier, the Tate equation does not account for the 3-D state of stress in the target. To adapt the dynamic cavity expansion pressure for modeling linear penetration, the dynamic term must be suitably modified. To account for a non-uniform radial pressure distribution in the cavity wall, Goodier (1965) assumed a factor of $\cos\theta$ for the dynamic pressure variation and during linear penetration equated the average radial pressure prevailing in the penetration process to the cavity expansion pressure (θ is the angle from the axis of penetration). Forrestal et al. (1995) adapted the dynamic spherical cavity expansion solution for metals by assuming a cosine variation in the normal component of the cavity expansion velocity, thus introducing a factor of 1/2 in the dynamic term of the equation of motion. Thus, one must be cautious in directly applying the cavity expansion solution to a Tate framework.

To relate the cavity expansion pressure P_c and steady-state velocity (V_c) to those of a linear penetration process (P_t and U, respectively), I suggest the following procedure. Consider a linear penetration event. Let the cavity in the target grow from x to x + Ut during time t, the steady state constant pressure is P_t during this time. Assume that using the same amount of energy, a spherical cavity would have grown from radius r to radius r + V_ct, with a constant cavity pressure P_c.

Now equating energy absorbed in both the processes,

$$P_t\pi r^2 U\Delta t = P_c \frac{2}{3}\pi\left[(r + V_c\Delta t)^3 - r^3\right] = P_c \frac{2}{3}\pi\left[3r^2 V_c\Delta t\right], \tag{3.84}$$

neglecting higher order terms in Δt. Thus, $P_t U = 2P_c V_c$.

Hence, in order to compare (equate) cavity expansion pressure with the average penetration pressure, one must use a cavity expansion velocity that is half the steady-state penetration velocity. This also corresponds to the average value of a $\cos\theta$ dependence of the normal components of penetration velocity (i.e., ranging from U at $\theta = 0$ to zero at $\theta = \pi/2$). This is also consistent with the assumption of Forrestal et al. (1995).

Figure 3.8 compares P_t for penetration velocities in AD995 alumina up to 3 km/s with experimental data (Subramanian and Bless). Evaluation of Eq. (3.83) was done using the values of elastic constants for alumina given in Section 3.3, with Y= 3 GPa and the velocity equivalence discussed above. The agreement is excellent despite the simplifying assumptions introduced. The good agreement substantiates both the analytical model and the framework for the description of failure in this ceramic.
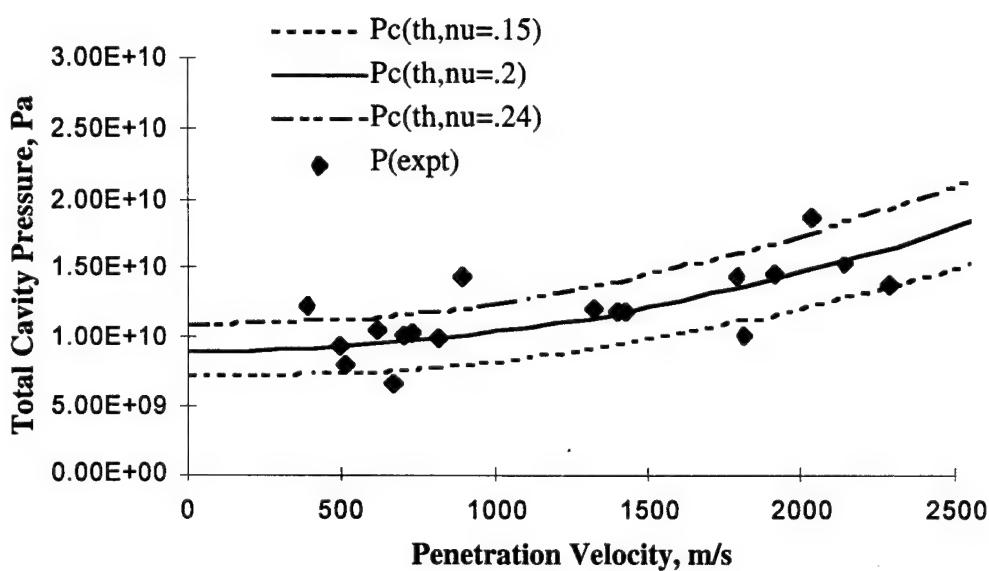
Figure 3.8. Comparison of computed and measured value of P_t for alumina (in the above figure, th ≡ theoretical; nu ≡ ν).

3.4.2 Self-similar solution for dynamic cavity expansion problem

In the previous section I derived the expression for dynamic cavity expansion with a constant cavity expansion speed using certain approximations. Here I present a solution to the field equations using a similarity transformation. Use of the similarity transformation technique enables the incorporation of a jump condition at the elastic-pulverized boundary and the shear-saturation behavior of the failed material. For constant expansion velocity, the cavity expansion problem admits a self-similar solution. Hunter and Crozier (1967) and Forrestal and Luk (1988) presented self-similar solutions for cavity expansion in ductile materials. Recently, Forrestal et al. (1997) have solved the dynamic cavity expansion problem in brittle-plastic materials like concrete.

The pressure-shear behavior of concrete follows the upper curve of Figure 3.1, and there is no need to consider a failure behavior of the type observed in brittle ceramics (lower curve of Figure 3.1). Forrestal et al. model concrete response as elastic-cracked-plastic. Here I present a solution for an elastic-brittle material which exhibits the cracking and comminution behavior described in the last two sections. Use of a similarity transformation in the steady-state cavity expansion problem is particularly attractive for penetration problems, since for high velocity penetration it is known that the steady state-regime dominates the penetration process.
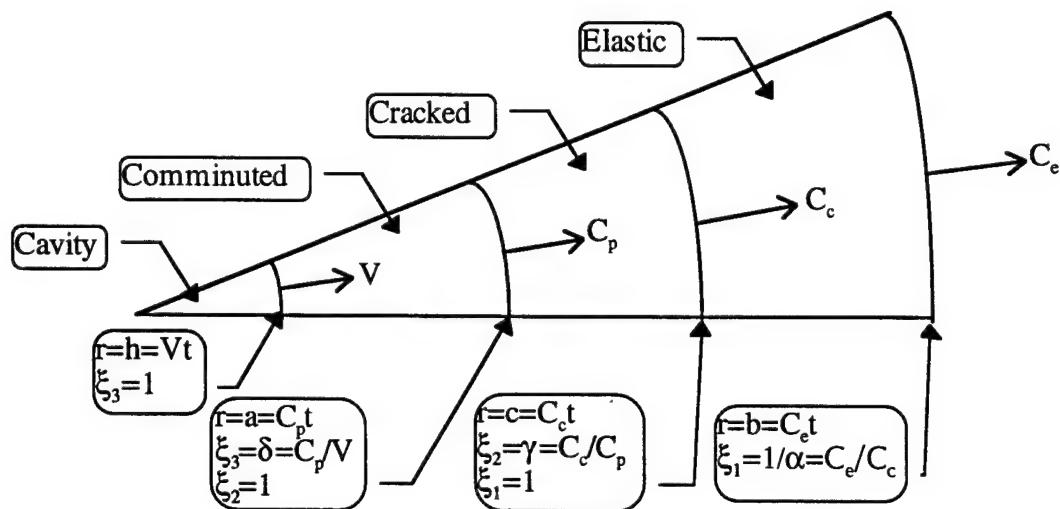
Figure 3.9. Dynamic response regions in a spherical cavity.

3.4.2.1 Elastic region

The stress-displacement relations for spherical symmetry can be written as

$$\sigma_r = -\frac{E}{(1+v)(1-2v)}\left[(1-v)\frac{\partial u}{\partial r} + 2v\frac{u}{r}\right], \tag{3.85}$$

$$\sigma_\theta = -\frac{E}{(1+v)(1-2v)}\left[v\frac{\partial u}{\partial r} + \frac{u}{r}\right], \tag{3.86}$$

87

where stresses are taken positive in compression. Ignoring the convective terms in Eqs. (3.62) and (3.63) and combining these equations with Eqs. (3.85) and (3.86) yields

$$\frac{\partial^2 u}{\partial r^2} + \frac{2}{r}\frac{\partial u}{\partial r} - \frac{2u}{r^2} = \frac{1}{C_e^2}\frac{\partial^2 u}{\partial t^2}, \tag{3.87}$$

where C_e is the dilatational elastic wave speed. Now introducing a similarity transformation

$$\xi_1 = \frac{r}{C_c t} \quad \text{and} \quad \bar{u}_1 = \frac{u}{C_c t}, \tag{3.88}$$

Equation (3.87) transforms to

$$\frac{d^2\bar{u}}{d\xi_1^2} + \frac{2}{\xi_1}\frac{d\bar{u}}{d\xi_1} - \frac{2\bar{u}}{\xi_1^2} = \alpha^2\xi^2\frac{d^2\bar{u}}{d\xi_1^2}, \tag{3.89}$$

where $\alpha \equiv C_c/C_e$.

Forrestal and Luk (1988) have shown that Eq. (3.89) has a solution of the form,

$$\bar{u} = A\alpha\xi_1 - B\frac{1 - 3\alpha^2\xi_1^2}{3\alpha^2\xi_1^2}, \tag{3.90}$$

where A and B are constants of integration to be evaluated from the boundary conditions. Denoting jump in any quantity by double square brackets,

$$\left[\!\left[\bar{u}\right]\!\right]_{\xi=1/\alpha} = 0, \tag{3.91}$$

since displacement has to be continuous at the elastic-undisturbed boundary. The other boundary condition is given by the fact that the elastic material cracks when the tensile hoop stress equals the tensile strength of the material, i.e.,

$$\sigma_\theta(\xi_1 = 1) = -\sigma_f. \tag{3.92}$$

Using the boundary conditions (3.91) and (3.92),

$$B = -\frac{3}{2}A \quad \text{and} \quad A = \left(\frac{\sigma_f}{\frac{1}{2}\rho_0 C_e^2}\right) \frac{\alpha^2(1-\nu)}{2\nu(\alpha^3-1)+(2\alpha^3-3\alpha^2+1)} \quad . \tag{3.93}$$

3.4.2.2 Cracked region

In this region the hoop stresses are zero due to the presence of radial cracks. For spherical symmetry, the two hoop directions perpendicular to the radial direction are equivalent. The material in this region is assumed to be in the form of needles. Alternatively, it is possible that the cracks are distributed in an incoherent and discontinuous manner in such a way that the material cannot support hoop stress and yet is not needle like. In either case, the material in the cracked region is capable of transmitting only radial stress. Since the hoop stress is zero, Eq. (3.62) reduces to,

$$\frac{\partial \sigma_r}{\partial r} + \frac{2\sigma_r}{r} = -\rho \ddot{u}. \tag{3.94}$$

As before, the stress and displacements are related by

$$\sigma_r = -E \frac{\partial u}{\partial r}. \tag{3.95}$$

For the cracked region, I introduce the following similarity transforms:

$$\xi_2 = \frac{r}{C_p t} \quad \text{and} \quad \bar{u}_2 = \frac{u}{C_p t}. \tag{3.96}$$

Using Eqs. (3.95) and (3.96) in (3.94), one obtains

$$\frac{d^2 \bar{u}_2}{d\xi_2^2} + \frac{2}{\xi_2} \frac{d\bar{u}_2}{d\xi_2} = \beta^2 \xi_2^2 \frac{d^2 \bar{u}_2}{d\xi_2^2}, \tag{3.97}$$

89

where $\beta \equiv C_p/C_{cr}$; $C_{cr} = \sqrt{E/\rho}$ is the bar wave speed. Integration of Eq. (3.97) results in the following expression for the dimensionless displacement in the cracked region.

$$\bar{u}_2 = -c_1 \frac{1 + \beta^2 \xi_2^2}{\xi_2} + c_2, \tag{3.98}$$

where c_1 and c_2 are constants of integration. The inner boundary of the cracked region is defined by the condition that the cracked material pulverizes when the compressive radial stress exceeds the compressive strength of the material. Thus,

$$\sigma_r(\xi_2 = 1) = -E \frac{d\bar{u}_2}{d\xi_2}\bigg|_{\xi_2 = 1} = Y. \tag{3.99}$$

Since no transverse crack is envisaged at the elastic-cracked boundary, the displacement should be continuous there. As a result, the second boundary condition for displacement is as follows.

$$\bar{u}_2\big|_{\xi_2 = \gamma} = \gamma \, \bar{u}_1\big|_{\xi_1 = 1}, \tag{3.100}$$

where $\gamma = C_c/C_p$. Substitution of the boundary conditions, Eqs. (3.99) and (3.100), into Eqs. (3.95) and (3.98) yields,

$$c_1 = \frac{Y}{E(\beta^2 - 1)} \text{ and } c_2 = \frac{Y}{\gamma E} \frac{(\beta^2 \gamma^2 + 1)}{(\beta^2 - 1)} + \left(\frac{\sigma_f \gamma}{\rho_0 C_e^2}\right)\left[\frac{(1 - \nu)(2\alpha^3 - 3\alpha^2 + 1)}{2\nu(\alpha^3 - 1) + (2\alpha^3 - 3\alpha^2 + 1)}\right]. \tag{3.101}$$

3.4.2.3 Hugoniot jump conditions

For the dynamic cavity expansion involving propagation of comminuted, cracked and elastic waves into the undisturbed material, Hugoniot jump conditions have to be satisfied at the propagation fronts. Denoting quantities on either side of the disturbance by subscripts + and -, Hugoniot jump conditions for mass and momentum can be written as (Courant and Friedrichs 1948):

$$\rho_-(v_- - C) = \rho_+(v_+ - C), \tag{3.102}$$

90

$$\sigma_+ - \sigma_- = \rho_-(C - v_-)(v_+ - v_-), \tag{3.103}$$

where v, C and σ are particle velocity, disturbance velocity and normal stress respectively. Denoting the volumetric strain by η, i.e.,

$$\eta = \frac{P}{K} = 1 - \frac{\rho_0}{\rho}, \tag{3.104}$$

Equations (3.102) and (3.103) can be combined to yield

$$\sigma_+ - \sigma_- = -\frac{\rho_0(C - v_-)^2}{(1 - \eta_-)^2}(\eta_+ - \eta_-). \tag{3.105}$$

For applying Eq. (3.105) to the elastic-cracked interface, I denote the quantities on the elastic and cracked sides of the interface by subscripts 1 and 2, respectively. The particle velocity and the radial stress on the elastic side of the interface are given by following equations:

$$v_1 = \frac{\partial u}{\partial t} = C_c\left[\bar{u}_1 - \xi_1 \frac{d\bar{u}_1}{d\xi_1}\right]_{\xi_1 = 1} = 3C_c A\frac{(1 - \alpha^2)}{2\alpha^2}, \tag{3.106}$$

$$\sigma_1 = -\frac{A\rho C_e^2}{(1 - v)}\left[\frac{\alpha^3(1 + 2v) - 3v\alpha^2 - (1 - 2v)}{\alpha^2}\right]. \tag{3.107}$$

The volumetric strain on the elastic side of the interface can be calculated from Eqs. (3.85), (3.86), (3.88), (3.90) and (3.104) as follows.

$$\eta_1 = -\left(\frac{3\sigma_f}{\frac{1}{2}\rho C_e^2}\right)\frac{\alpha^2(\alpha - 1)(1 - v)}{\left[2\alpha^3(1 + v) - 3\alpha^2 + (1 - 2v)\right]} \tag{3.108}$$

91

Similarly, the volumetric strain on the cracked side of the interface can be calculated from Eq. (3.95), (3.96), (3.98) and (3.104) as follows.

$$\eta_2 = \frac{Y}{3K} \frac{\left(1 - \beta^2 \gamma^2\right)}{\left(1 - \beta^2\right)\gamma^2} \tag{3.109}$$

Now using Eqs. (3.85), (3.95) and (3.109) in Eq. (3.105), the following relation between α and β is obtained.

$$\gamma^2 = \left(\frac{\alpha}{\beta}\frac{C_e}{C_{cr}}\right) = \frac{Y\left(\beta^2\gamma^2 - 1\right)\left[1 + \frac{\rho_0}{3K}\left(\frac{C_{cr} - V_1}{1 - \eta_1}\right)^2\right] - \sigma_1\beta^2\gamma^2 - \eta_1\beta^2\gamma^2\rho_0\left(\frac{C_{cr} - V_1}{1 - \eta_1}\right)^2}{-\left[\sigma_1 + \eta_1\rho_0\left(\frac{C_{cr} - V_1}{1 - \eta_1}\right)^2\right]} \tag{3.110}$$

3.4.2.4 Comminuted region

When the radial compressive stress in the cracked region, where the material has already failed in two orthogonal hoop directions, increases to the compressive strength of the material, it becomes granular or pulverized. The Mohr-Coulomb material model is employed to define the material behavior of the granular material. The granular material cannot support any shear in the absence of pressure, as observed by Rosenberg et al. (1988). Thus the cohesive strength is taken as zero. There is a possibility that the level of comminution will vary with varying pressure, resulting in a non-linear pressure-shear behavior. I ignore this possible non-linearity, and assume that the shear strength increases linearly with the confining pressure. Denoting the constant of proportionality between pressure and shear by m, for spherical symmetry,

$$\frac{\sigma_r - \sigma_\theta}{2} = m\frac{\sigma_r + 2\sigma_\theta}{3}. \tag{3.111}$$

Using Eq. (3.111), the equation of motion, Eq. (3.62) reduces to,

$$\frac{\partial\sigma_r}{\partial r} + 2\bar{\alpha}\frac{\sigma_r}{r} = -\rho\left(\frac{\partial v}{\partial t} + v\frac{\partial v}{\partial r}\right), \tag{3.112}$$

92

where $\overline{\alpha} = 6m/(3+4m)$. Employing the similarity transformations

$$\xi_3 = \frac{r}{Vt}, \quad \overline{u}_3 = \frac{u}{Vt} \text{ and } U = \frac{v}{V},$$ (3.113)

Eq. (3.112) becomes

$$\frac{d\sigma_r}{d\xi_3} + 2\overline{\alpha}\frac{\sigma_r}{\xi_3} = -\rho V^2 \frac{dU}{d\xi_3}(U-\xi_3).$$ (3.114)

Ignoring dilatancy in the comminuted region, Eq. (3.63) reduces to,

$$v = \frac{D_1}{r^2},$$ (3.115)

where D_1 is the constant of integration. For a cavity being created in a continuous medium, with a constant cavity expansion velocity, $v(r=h) = V$. Thus, in terms of non-dimensional quantities, Eq. (3.115) becomes

$$U = \frac{1}{\xi_3^{\,2}}.$$ (3.116)

Inserting Eq. (3.116) into Eq. (3.114) and integrating once yields

$$\sigma_r = -\left(\frac{\rho V^2}{\xi_3^{\,2\overline{\alpha}}}\right)\left(-\frac{2}{2\overline{\alpha}-4}\xi_3^{\,2\overline{\alpha}-4} + \frac{2}{2\overline{\alpha}-1}\xi_3^{\,2\overline{\alpha}-1}\right) + \frac{D_2}{\xi_3^{\,2\overline{\alpha}}},$$ (3.117)

where D_2 is the integration constant. The Hugoniot jump condition is invoked at the comminuted-cracked interface to evaluate D_2. By assumption, there is no dilatancy across the cracked-comminuted interface. Hence from Eq. (3.102) and (3.103), there will be no jump in particle velocity or radial stress at this interface. But the density for this region is the same as that at the

93

cracked-comminuted boundary. From Eqs. (3.99) and (3.104), the density is given by $\rho = \rho_0/(1-Y/3K)$. Since $Y \ll K$, $\rho \sim \rho_0$. Now using the condition that the cracked material pulverizes when the radial stress equals the compressive strength, i.e., $\sigma_r|_{\xi_3=\delta} = Y$ (where $\delta \equiv C_p/V$), and continuity of radial stress from the Hugoniot jump condition,

$$D_2 = Y\delta^{2\bar{\alpha}} + 2\rho_0 V^2 \left(-\frac{1}{2(\bar{\alpha}-2)}\delta^{2\bar{\alpha}-4} + \frac{1}{2\bar{\alpha}-1}\delta^{2\bar{\alpha}-1} \right). \tag{3.118}$$

Finally, denoting the pressure at the cavity surface by P_c, the stress required to maintain the constant cavity expansion velocity for opening up a spherical cavity in a continuous ceramic media is given by the following expression.

$$P_c \equiv \sigma_r|_{\xi_3=1} = Y\delta^{2\bar{\alpha}} + \rho_0 V^2 \left(\frac{\delta^{2\bar{\alpha}-4}}{2-\alpha} - \frac{2\delta^{2\bar{\alpha}-1}}{1-2\alpha} + \frac{3}{(1-2\alpha)(2-\alpha)} \right). \tag{3.119}$$

δ needs to be related to α and β. Volume conservation in the incompressible comminuted zone, in terms of the non-dimensional quantities, is given by

$$(\xi_3 - \bar{u}_3)^3 = \xi_3^3 - 1. \tag{3.120}$$

Evaluating Eq. (3.120) at $\xi_3 = \delta$ and assuming that $\bar{u}_3(\xi_3 = \delta)$ is small,

$$\bar{u}_3(\xi_3 = \delta) = \frac{1}{3\delta^2}. \tag{3.121}$$

Continuity of displacement at the cracked-comminuted boundary is enforced by requiring that

$$\bar{u}_3(\xi_3 = \delta) = \delta \, \bar{u}_2(\xi_2 = 1). \tag{3.122}$$

94

Thus, from Eqs. (3.98), (3.121) and (3.122), the following relation between α, β and δ is obtained.

$$\delta^3 = \frac{1}{3\left[c_2 - c_1(1+\beta^2)\right]} \tag{3.123}$$

To compute R_t as a function of the cavity expansion velocity, I adopt the following procedure. Starting with a given α, v_1 and η_1 are calculated from Eqs. (3.106) and (3.108), respectively. Then Eq. (3.110) is employed to compute β. Subsequently, the constants c_1 and c_2 are calculated from Eq. (3.101). Finally, δ is calculated from Eq. (3.123), from which R_t is calculated from Eq. (3.119).

3.4.2.5 Elastic-comminuted response

Numerical evaluations (shown later) indicate that the cracked zone disappears when the cavity expansion velocity increases beyond a certain value. Thereafter the material response is elastic-comminuted. In such a situation, the constant A in Eq. (3.90) needs to be reevaluated using the boundary condition $\sigma_r(\xi_1 = 1) = Y$. Evaluation of Eq. (3.85) with Eqs. (3.88) and (3.90), along with the above boundary condition, yields

$$A = -\frac{Y(1-v)}{\rho_0 C_e^2}\left[\frac{\beta^2}{\beta^3(1+2v) - 3v\beta^2 - (1-2v)}\right] \tag{3.124}$$

Also to evaluate δ, the boundary condition Eq. (3.122) must be replaced by

$$\bar{u}_3(\xi_3 = \delta) = \delta\,\bar{u}_1(\xi_1 = 1). \tag{3.125}$$

Evaluating Eqs. (3.125), (3.124), (3.121) and (3.90), the following relationship between β and δ is obtained.

95

$$\delta^3 = \frac{2\beta^2}{3A\left(2\beta^3 - 3\beta^2 + 1\right)} \tag{3.126}$$

The cavity expansion pressure is still given by Eq. (3.119).

3.4.2.6   Shear saturation in the failed material

Experiments (Rosenberg et al. 1987) suggest that the shear strength of the material immediately behind the shock wave in plate impact experiments saturates for shock pressures above the HEL. This issue was discussed at length, at the end of Section 3.3.1.9. So far, I have modeled the comminuted material as a linear Mohr-Coulomb-type material. If the failed material saturates at a level $\sigma_r - \sigma_\theta = 2\tau$, the comminuted region can be divided into two sub-regions: a saturated region ($a < r < b$) and a linear region ($b < r < c$). From Eq. (3.111),

$$\sigma_r = \frac{2\tau}{\overline{\alpha}}. \tag{3.127}$$

The equation of motion for the saturated region becomes

$$\frac{d\sigma_r}{d\xi_3} + \frac{4\tau}{\xi_3} = -\rho V^2 \frac{dU}{d\xi_3}(U - \xi_3). \tag{3.128}$$

Integrating Eq. (3.128) with Eq. (3.115) from $r = a$ ($\xi_3 = 1$) to $r = b$ ($\xi_3 = \delta_1$),

$$P_c = \frac{2\tau}{\overline{\alpha}} + 4\tau \ln\delta_1 + \frac{\rho V^2}{2}\left[-\frac{1}{\delta_1^4} + \frac{4}{\delta_1} - 3\right]. \tag{3.129}$$

The equation of motion for the linear failed region is given by Eq. (3.113). Integrating this equation with the velocity distribution given by Eq. (3.115), from $r = b$ ($\xi_3 = \delta_1$) to $r = c$ ($\xi_3 = \delta$) and recognizing that $\sigma_r(\xi_3 = \delta_1) = 2\tau/\overline{\alpha}$ and $\sigma_r(\xi_3 = \delta) = Y$, one obtains

$$Y\delta^{2\bar{\alpha}} - \frac{2\tau}{\bar{\alpha}}\delta_1^{2\bar{\alpha}} = 2\rho_0 V^2 \left[\frac{\delta^{2\bar{\alpha}-4} - \delta_1^{2\bar{\alpha}-4}}{2\bar{\alpha} - 4} - \frac{\delta^{2\bar{\alpha}-1} - \delta_1^{2\bar{\alpha}-1}}{2\bar{\alpha} - 1} \right].$$

(3.130)

Thus for a given β, Eq. (3.126) is solved for δ. Eq. (3.130) is then iteratively solved to obtain δ_1, which is used in Eq. (3.129) to yield the cavity expansion pressure.

3.4.2.7 Results

Figure 3.10 shows the expansion velocities of cracked and comminuted fronts for different cavity expansion velocities in AD995 ceramic. The material constants used are the same as those presented in Section 3.3.1.7. For a cavity expansion velocity of 980 m/s the cracked region disappears, i.e., $C_c = C_p = 4.9$ km/s. Thereafter the material response is elastic-comminuted. Similar observations were made by Forrestal et al. (1997) for dynamic cavity expansion in concrete. The speed of the comminuted zone becomes saturated at a level of 9.5 km/s, after a cavity expansion speed of about 1.5 km/s. Strassburger et al. (1994) had observed a saturation speed of about 9.5 km/s in end-on impact of alumina plates by cylindrical projectiles whose diameter was greater than the thickness of the target plates. Even though this experimental geometry was a plane stress configuration, the saturation limit speed of the failed zone seems to be similar to that found for spherical cavity expansion.
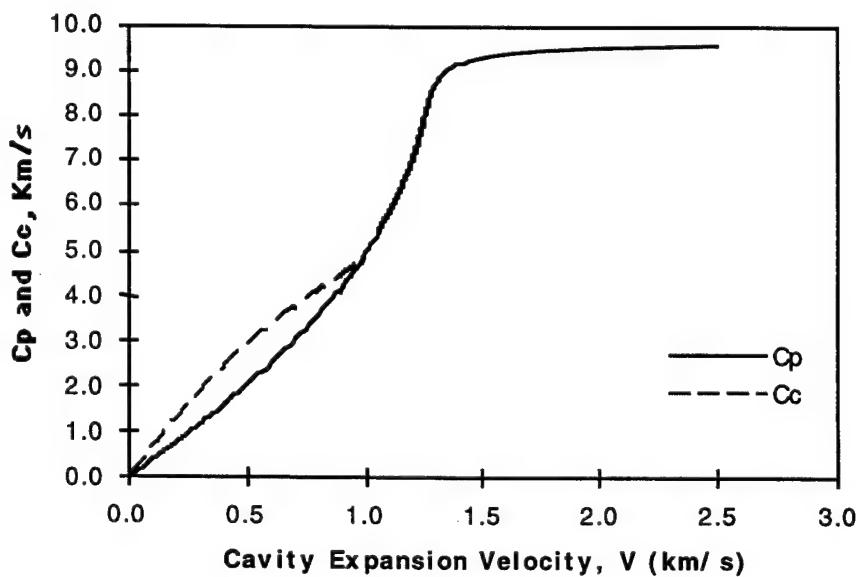
Figure 3.10. Speeds of the comminuted and cracked zones.

To relate the dynamic cavity expansion pressure to the projectile-target interface pressure prevalent in a penetration situation, the velocity equivalence discussed in Section 3.4.1.1. is adopted. Thus the cavity expansion speed, V, is equivalent to half the steady state penetration velocity, U_p. The cavity expansion pressure for AD995 alumina ceramic is plotted in Figure 3.11 (a) for cases of shear saturation and no shear saturation in the comminuted region. The curves yield the value of quasi-static cavity expansion pressure (Eq. 3.34) at zero cavity expansion velocity, as a check for the numerical solution. Rosenberg et al.'s (1987) plate impact experiments suggested that the shear stress behind the shock wave saturates at about 2.7 GPa for AD85 ceramic. The material immediately behind the shock wave is unlikely to be totally damaged. Thus, the saturation level of the lower curve should be less than this value. In Figure 3.11 (a), the cavity expansion pressure is plotted for four different levels of saturation value and for $\mu = 0.2$. Experimental values of the interface pressure from Subramanian and Bless (1995) are also plotted in the same figure. Assuming that the specimen's finite size has not affected the experimental data, the data exhibits closer agreement with the analytical solution for a saturation stress of 1.5 GPa.

Traditionally, penetration resistance of target materials is measured in terms of the target resistance, R_t in the Tate equation, where the inertial term is $0.5\rho U_p^2$. Figure 3.11 (b) shows the equivalent R_t (equivalent R_t = cavity expansion pressure with cavity expansion velocity equal to half the penetration velocity - $0.5\rho U_p^2$) along with the experimental values obtained by Subramanian and Bless (1995). While the model with saturation stress of 1.5 GPa shows best agreement with the trend of the experimental data, all the curves are within the experimental scatter.
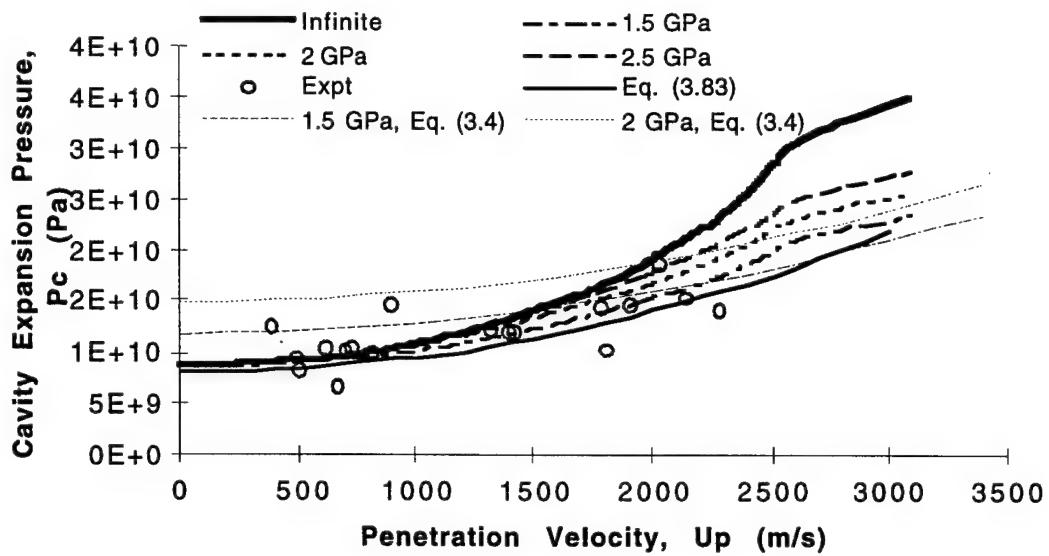
(a)
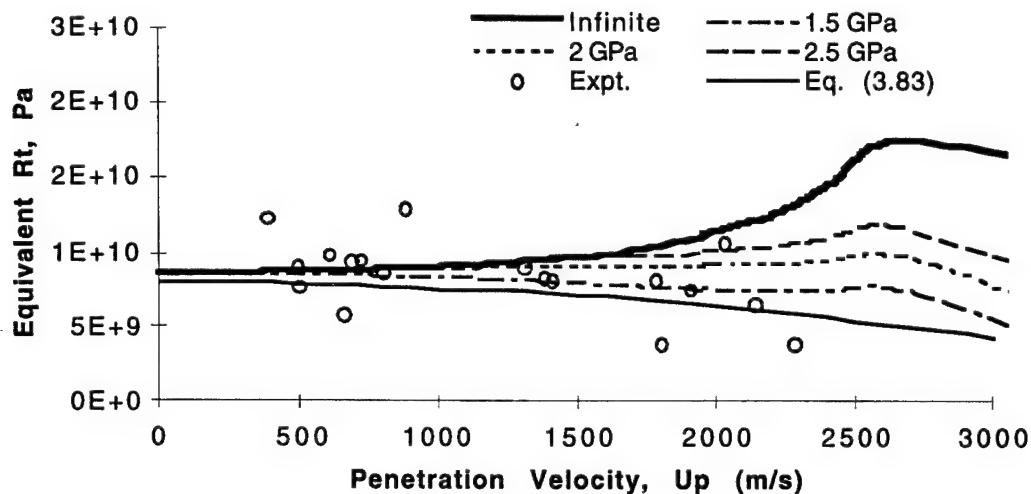
(b)

Figure 3.11. (a) Cavity expansion pressure vs. penetration velocity for different shear-saturation levels. **(b)** Equivalent Rt vs. penetration velocity for different shear-saturation levels.

The model suggests that the quasi-static spherical cavity expansion pressure is a good approximation for the constant R_t term in the Tate equation until a penetration velocity of about 2.5 km/s. Beyond this speed, the penetration resistance starts to decrease sharply. Comparison of

99

Figure 3.11(a) with the penetration resistance curve for RHA steel (Figure 4.5) suggests that, while penetration resistance of RHA drops significantly with velocity (becomes negative beyond a penetration speed of 2.3 km/s), AD995 ceramic retains its resistance at a nearly constant level until a penetration speed of about 2.5 km/s. Thus ceramics like AD995 alumina are much better materials for use as protective structures compared to RHA.

3.5   Penetration resistance of ceramic/ metal laminate targets

A semi-infinite target has no outer boundary by definition. It was found in the previous sections that the cavity expansion pressure for this case is purely determined by the material properties. However, practical applications involve protective structures with finite geometrical dimensions. Also, for performance evaluation of different ceramic materials, finite ceramic tiles backed by thick metal substrates are used. By measuring the residual penetration (DOP)[1] into the metallic substrate, the effectiveness of the overlaying ceramic material is measured (Woolsey 1992). Thus, for these cases, the effective penetration resistance of the finite ceramic tile may be strongly affected by the presence of finite boundaries.

In the following, I consider the case where a ceramic tile lays over a semi-infinite metallic substrate. The effects of the finite lateral boundary are ignored by assuming that the lateral dimension is infinite. In practice this condition may also be achieved if the ceramic is suitably confined so that the effects of the free-lateral surfaces are eliminated. The finite dimension of the metal substrate may also affect the performance grading results. However, that consideration will be deferred for future work.

Depending on the proximity of the penetrator-target interface to the ceramic-metal interface, four distinct possibilities arise (see Figure 3.12). It shall be shown that no other possibility can exist.

---

[1] DOP was defined by Woolsey as the depth of (residual) penetration into the substrate over which the ceramic tile lays.

(a)

$$R_t = Y\left\{\frac{3Y}{E}\left[1-\left(\frac{a}{c}\right)(1-\nu)+\left(\frac{c}{a}\right)\frac{3\sigma_f}{E}(1-\nu)\right]\right\}^{\frac{2\bar{\alpha}}{3}}$$

$$\left(\frac{b}{c}\right)^3 = \frac{6K(\mu_m/\mu-1)}{4\mu_m+3K}\left[\frac{(a/c)^2+\sigma_f/Y}{(a/c)^2-2\sigma_f/Y}\right]$$

$$\left(\frac{h}{a}\right)^3 = \frac{3Y}{E}\left[1-\left(\frac{a}{c}\right)(1-\nu)+\left(\frac{c}{a}\right)\frac{3\sigma_f}{E}(1-\nu)\right]$$

(b)

$$R_t = Y\left\{\frac{3Y}{E}\left[1-\left(\frac{a}{b}\right)\right]+\frac{Y}{4\mu_m}\left(\frac{a}{b}\right)\right\}^{-2\bar{\alpha}/3}$$

$$\left(\frac{h}{a}\right)^3 = \frac{3Y}{E}\left[1-\left(\frac{a}{b}\right)\right]+\frac{Y}{4\mu_m}\left[\frac{a}{b}\right]$$

(c)

$$R_t = Y\left\{\frac{3Y}{E}+\frac{3Y_m}{6\mu_m}\left(\frac{d}{b}\right)^3\left(\frac{b}{a}\right)-\frac{Y}{E}\left(\frac{a}{b}\right)\right\}^{-2\bar{\alpha}/3}$$

$$\left(\frac{d}{b}\right) = \exp\left\{\frac{1}{2Y_m}\left[Y\left(\frac{a}{b}\right)^2-\frac{2Y_m}{3}\right]\right\}$$

$$\left(\frac{h}{a}\right)^3 = \frac{3Y}{E}+\frac{3Y_m}{6\mu_m}\left(\frac{d}{b}\right)^3\left(\frac{b}{a}\right)-\frac{Y}{E}\left(\frac{a}{b}\right)$$

(d)

$$R_t = Y_m\left\{2\ln\left(\frac{b}{d}\right)+\frac{2}{3}\right\}\left(\frac{b}{h}\right)^{2\bar{\alpha}}$$

$$\left(\frac{h}{b}\right)^3 = \frac{Y_m}{2\mu_m}\left(\frac{d}{b}\right)^3$$
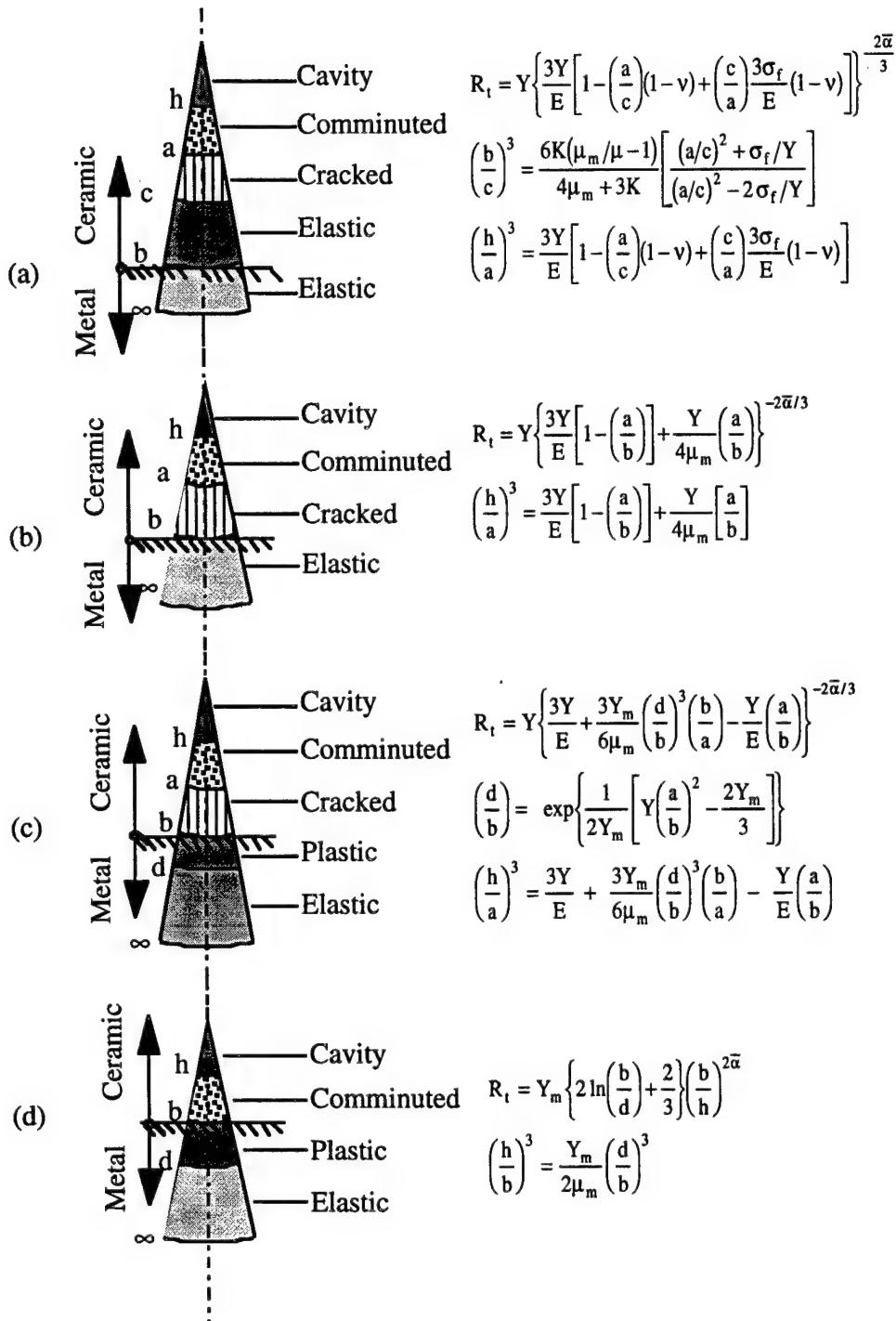
Figure 3.12. Schematic of cavity profiles for four different possible scenarios, in ceramic targets backed by semi-infinite metal.

<u>Case (a)</u>

When the tip of the penetrator is far away from the ceramic-metal interface (henceforth called "the interface"), the ceramic material has four zones: cavity, comminuted, cracked and elastic. The metallic substrate is elastic. The solutions to the field equations for spherical cavity expansion in metal were presented in Chapter 2 and those for ceramics were presented in this chapter. These solutions for different regions in Figure 3.12(a) are as follows.

$$
\left.
\begin{aligned}
u &= \frac{c_1}{r^2} \\
\sigma_r &= -4\mu_m \frac{c_1}{r^3} \\
\sigma_\theta &= 2\mu_m \frac{c_1}{r^3}
\end{aligned}
\right\} \qquad \text{for } b < r < \infty. \tag{3.131}
$$

$$
\left.
\begin{aligned}
u &= c_2 r + \frac{c_3}{r^2} \\
\sigma_r &= c_2(3\lambda + 2\mu) - 4\mu \frac{c_3}{r^3} \\
\sigma_\theta &= c_2(3\lambda + 2\mu) + 2\mu \frac{c_3}{r^3}
\end{aligned}
\right\} \qquad \text{for } c < r < b. \tag{3.132}
$$

$$
\left.
\begin{aligned}
u &= \frac{Y}{E}\frac{a^2}{r} + c_4 \\
\sigma_r &= -Y\left(\frac{a}{r}\right)^2
\end{aligned}
\right\} \qquad \text{for } a < r < c. \tag{3.133}
$$

$$
\left.
\begin{aligned}
\frac{u(a)}{a} &= \frac{1}{3}\left(\frac{h}{a}\right)^3 \\
\sigma_r &= -Y\left(\frac{a}{r}\right)^{2\bar{\alpha}}
\end{aligned}
\right\} \qquad \text{for } h < r < a. \tag{3.134}
$$

Here μ and λ are the Lamé constants for the ceramic and μ_m is the elastic shear modulus for the metal. c_1 through c_4 are constants to be evaluated from the boundary conditions. The boundary conditions are that the radial stresses and the displacements are continuous at $r = a$, c and b. Using these boundary conditions in Eqs. (3.131) to (3.134), the following relations between the constants are obtained.

$$\left.\begin{aligned}
\frac{c_1}{b^2} &= c_2 b + \frac{c_3}{b^2} \\[2mm]
-4\mu_m \frac{c_1}{b^3} &= c_2(3\lambda + 2\mu) - 4\mu \frac{c_3}{b^3} \\[2mm]
c_2(3\lambda + 2\mu) - 4\mu \frac{c_3}{c^3} &= -Y\left(\frac{a}{c}\right)^2 \\[2mm]
c_2(3\lambda + 2\mu) + 2\mu \frac{c_3}{c^3} &= \sigma_f \\[2mm]
c_2 c + \frac{c_3}{c} &= \frac{Y}{E}\frac{a^2}{c} + c_4 \\[2mm]
\frac{1}{3}\left(\frac{h}{a}\right)^3 &= \frac{Y}{E} + \frac{c_4}{a}
\end{aligned}\right\} \qquad (3.135)$$

In Eq. (3.135), there are six relations involving four unknown constants, c_1, c_2, c_3, c_4, and two unknown boundaries, a and c; h (cavity radius) and b (proximity to the interface) are known. With some algebra, solution of these relations yields expressions for the unknowns, which are then substituted into Eq. (3.134) to yield

$$\left.\begin{aligned}
P_c &= Y\left\{\frac{3Y}{E}\left[1-\left(\frac{a}{c}\right)(1-v)+\left(\frac{c}{a}\right)\frac{3\sigma_f}{E}(1-v)\right]\right\}^{-2\bar{\alpha}/3} \\[2mm]
\left(\frac{b}{c}\right)^3 &= \frac{6K(\mu_m/\mu - 1)}{4\mu_m + 3K}\left[\frac{(a/c)^2 + \sigma_f/Y}{(a/c)^2 - 2\sigma_f/Y}\right] \\[2mm]
\left(\frac{h}{a}\right)^3 &= \frac{3Y}{E}\left[1-\left(\frac{a}{c}\right)(1-v)+\left(\frac{c}{a}\right)\frac{3\sigma_f}{E}(1-v)\right]
\end{aligned}\right\}, \qquad (3.136)$$

where P_c is the cavity expansion pressure, equal to the negative of the radial stress at the cavity boundary, $r = h$. Additionally, the equivalent stress at the interface is given by

$$\left(\sigma_\theta - \sigma_r\right)\Big|_{r=b} = 3\mu_m\sigma_f\left[\frac{4\mu + 3K}{\beta^3\mu(4\mu_m + 3K) - 6K(\mu_m - \mu)}\right],\tag{3.137}$$

where $\beta = b/c$. The maximum value of β is 1, corresponding to the situation where the cracked front reaches the interface. Evaluating Eq. (3.137) for $\beta = 1$ and with $\mu = 152$ GPa, $K = 222$ GPa (for AD995) and $\mu_m = 80$ GPa (for RHA), the maximum equivalent stress is 0.5 GPa. Since this is smaller than the yield strength of the steel, it is concluded that the metal has not yielded for this case.

Case (b)

When the tip of the penetrator draws closer to the interface, the cracked front will reach the interface, as shown in Figure 3.12(b). The solutions for different regions are as follows.

$$\left.\begin{aligned}u &= \frac{c_1}{r^2}\\[2mm]\sigma_r &= -4\mu_m\frac{c_1}{r^3}\\[2mm]\sigma_\theta &= 2\mu_m\frac{c_1}{r^3}\end{aligned}\right\} \qquad \text{for } b < r < \infty.\tag{3.138}$$

$$u = \frac{Y}{E}\frac{a^2}{r} + c_2 \Bigg\rbrace$$
$$\sigma_r = -Y\left(\frac{a}{r}\right)^2 \Bigg]$$

for $a < r < b$.

(3.139)

$$\frac{u(a)}{a} = \frac{1}{3}\left(\frac{h}{a}\right)^3 \Bigg\rbrace$$
$$\sigma_r = -Y\left(\frac{a}{r}\right)^{2\bar{\alpha}} \Bigg]$$

for $h < r < a$.

(3.140)

The constants c_1 and c_2 will be evaluated from the boundary conditions that the radial stresses and displacements are continuous at $r = a$ and c. Thus the following relations among the constants are obtained.

$$-4\mu_m \frac{c_1}{b^3} = -Y\left(\frac{a}{b}\right)^2 \Bigg]$$
$$\frac{c_2}{b^2} = \frac{Y}{E}\frac{a^2}{b} + c_2 \Bigg\rbrace$$
$$\frac{1}{3}\left(\frac{h}{a}\right)^3 = \frac{Y}{E} + \frac{c_2}{a} \Bigg]$$

(3.141)

In Eq. (3.141), there are three relations involving constants c_1, c_2 and the unknown boundary a, for given h and b. Solution of these relations yields

$$P_c = Y\left\{ \frac{3Y}{E}\left[1 - \left(\frac{a}{b}\right)\right] + \frac{Y}{4\mu_m}\left(\frac{a}{b}\right) \right\}^{-2\bar{\alpha}/3}$$
$$\left(\frac{h}{a}\right)^3 = \frac{3Y}{E}\left[1 - \left(\frac{a}{b}\right)\right] + \frac{Y}{4\mu_m}\left[\frac{a}{b}\right]$$

(3.142)

From Eqs. (3.139) and (3.141), the equivalent stress in the metal at the interface is given by

$$\left(\sigma_\theta - \sigma_r\right)\big|_{r=b} = \frac{3Y}{2}\left(\frac{a}{b}\right)^2.$$

(3.143)

Thus the metal will yield when

$$\frac{a}{b} = \sqrt{\frac{2Y_m}{3Y}},$$

(3.144)

where Y_m is the yield strength of the metal. For AD995 ceramic/ RHA steel composite ($Y_m = 1$ GPa), $a/b = 0.47$. After this point, a plastic zone will appear in the metal, which is case (c).

Case (c)

When the penetrator tip is sufficiently close to the interface so that the response of the metal is plastic-elastic, the following equations are the solutions to the field equations in different regions.

$$\left. \begin{array}{l} u = \dfrac{c_1}{r^2} \\[2mm] \sigma_r = -4\mu_m \dfrac{c_1}{r^3} \\[2mm] \sigma_\theta = 2\mu_m \dfrac{c_1}{r^3} \end{array} \right\} \qquad \text{for } d < r < \infty.$$

(3.145)

$$u(b) = u(d)\left(\dfrac{d}{b}\right)^2$$

$$\sigma_r = 2Y_m \ln r + c_2$$
for b < r < d. (3.146)

$$u = \dfrac{Y}{E}\dfrac{a^2}{r} + c_3$$

$$\sigma_r = -Y\left(\dfrac{a}{r}\right)^2$$
for a < r < b. (3.147)

$$\dfrac{u(a)}{a} = \dfrac{1}{3}\left(\dfrac{h}{a}\right)^3$$

$$\sigma_r = -Y\left(\dfrac{a}{r}\right)^{2\bar{a}}$$
for h < r < a. (3.148)

The constants c_1, c_2 and c_3 are obtained from the continuity of radial stresses and displacements at $r = a$, b and d and the yield condition at $r = d$. Thus the following equations relate the constants c_1, c_2, c_3 and the unknown boundaries a and d.

$$6\mu_m \dfrac{c_1}{d^3} = Y_m$$

$$-4\mu_m \dfrac{c_1}{d^3} = 2Y_m \ln d + c_2$$

$$\dfrac{c_1}{b^2} = \dfrac{Y}{E}\dfrac{a^2}{b} + c_3$$

$$2Y_m \ln b + c_2 = -Y\left(\dfrac{a}{b}\right)^2$$

$$\dfrac{1}{3}\left(\dfrac{h}{a}\right)^3 = \dfrac{Y}{E} + \dfrac{c_3}{a}$$
(3.149)

Solving the above equations yields

$$
\left.\begin{aligned}
P_c &= Y \left\{ \frac{3Y}{E} + \frac{3Y_m}{6\mu_m} \left(\frac{d}{b}\right)^3 \left(\frac{b}{a}\right) - \frac{Y}{E}\left(\frac{a}{b}\right) \right\}^{-2\bar{\alpha}/3} \\
\left(\frac{d}{b}\right) &= \exp\left\{ \frac{1}{2Y_m}\left[Y\left(\frac{a}{b}\right)^2 - \frac{2Y_m}{3} \right] \right\} \\
\left(\frac{h}{a}\right)^3 &= \frac{3Y}{E} + \frac{3Y_m}{6\mu_m} \left(\frac{d}{b}\right)^3 \left(\frac{b}{a}\right) - \frac{Y}{E}\left(\frac{a}{b}\right)
\end{aligned}\right\}. \qquad (3.150)
$$

Case (d)

Finally, after the cracked zone has disappeared, the comminuted zone of the ceramic material will be in contact with the metal, whose response is plastic-elastic, as shown in Figure 3.12(d). The solutions to the field equations for this case are

$$
\left.\begin{aligned}
u &= \frac{c_1}{r^2} \\
\sigma_r &= -4\mu_m \frac{c_1}{r^3} \\
\sigma_\theta &= 2\mu_m \frac{c_1}{r^3}
\end{aligned}\right\} \qquad \text{for } d < r < \infty, \qquad (3.151)
$$

$$
\left.\begin{aligned}
u(b) &= u(d)\left(\frac{d}{b}\right)^2 \\
\sigma_r &= 2Y_m \ln r + c_2
\end{aligned}\right\} \qquad \text{for } b < r < d, \qquad (3.152)
$$

$$
\left.\begin{aligned}
\frac{u(a)}{a} &= \frac{1}{3}\left(\frac{h}{a}\right)^3 \\
\sigma_r &= \frac{c_3}{r^{2\bar{\alpha}}}
\end{aligned}\right\} \qquad \text{for } h < r < b. \qquad (3.153)
$$

Solving these equations with the boundary conditions that the radial stresses and displacements are continuous at $r = b$ and d and the yield condition at $r = d$, one obtains

$$
\left.\begin{aligned}
6\mu_m \frac{c_1}{d^3} &= Y_m \\
-4\mu_m \frac{c_1}{d^3} &= 2Y_m \ln d + c_2 \\
2Y_m \ln b + c_2 &= \frac{c_3}{b^{2\alpha}} \\
\frac{1}{3}\left(\frac{h}{a}\right)^3 &= \frac{Y_m}{6\mu_m}\left(\frac{d}{b}\right)^3
\end{aligned}\right\}.
\tag{3.154}
$$

Solution of these equations results

$$
\begin{aligned}
P_c &= Y_m\left\{2\ln\left(\frac{b}{d}\right)+\frac{2}{3}\right\}\left(\frac{b}{h}\right)^{2\bar{\alpha}} \\
\left(\frac{h}{b}\right)^3 &= \frac{Y_m}{2\mu_m}\left(\frac{d}{b}\right)^3
\end{aligned}.
\tag{3.155}
$$

It is noted that when $b/h = 1$ (i.e., when the penetrator hits the metallic substrate), P_c in Eq. (3.155) reduces to the cavity expansion pressure for the metal.

3.5.1 Results

Eqs. (3.136), (3.142), (3.50) and (3.155) can be solved to obtain the cavity expansion pressure and the size of the different zones for given values of h (cavity size) and b (interface distance from the penetrator tip). In Figure 3.13 the relative sizes of different zones are plotted for different values of b/h. Figure 3.14 shows the variation of the cavity pressure with b/h ratio. It is seen that the penetration resistance is not affected for $b/h > 15$, where the ceramic behaves as an infinite target. Once the

110

boundary is sensed, slow and gradual strength reduction occurs until the cracked region reaches the interface (at about a distance of 11 penetrator radii from the interface). An immediate reduction occurs, followed by a near constant strength which falls rapidly as the cracked/ comminuted interface approaches the ceramic/ metal interface. The comminuted region reaches the interface at about 2 penetrator radii, at which point the strength degrades towards a lower bound equal to the cavity expansion pressure in the metal.

Thus, this analysis shows that the effect of the finite boundary on the ceramic must be considered for cases in which the penetrator reaches about 10 X diameter from the ceramic boundary. DOP tests with thin tiles (thickness ~ 5 X penetrator diameter) do not indicate the inherent penetration resistance of semi-infinite ceramics. The average resistance encountered will depend on the thickness in addition to the material constants of the ceramic and the metallic substrate.
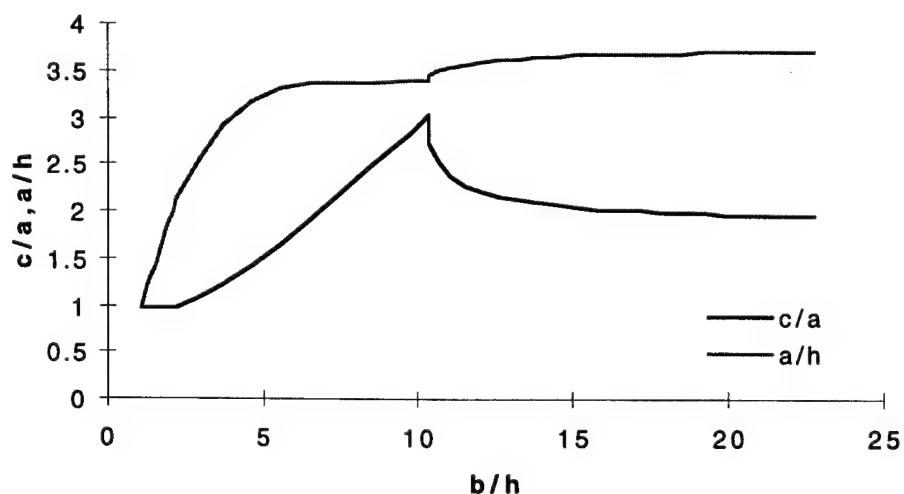
Figure 3.13. Variation of relative size of different zones with proximity to interface.
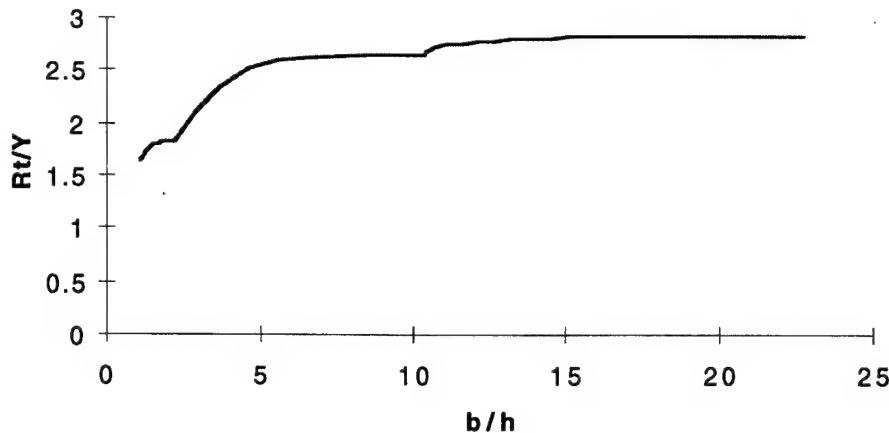
Figure 3.14. **Variation of cavity expansion pressure with proximity to the interface.**

Anderson et al. (1995) presented data for 2.586 cm thick alumina targets backed by semi-infinite RHA substrates, and impacted by tungsten alloy penetrators. The alumina thickness was about 3.5 times the penetrator diameter. The following table compares the penetration data with the predictions from the model described above. The second and third columns show the experimental impact velocities and the measured residual penetration into the RHA block, respectively. The fourth column shows the predictions of the CTH hydrocode for the residual penetration. The fifth and sixth columns shows the depth of penetration obtained by using Tate equation along with the degrading R_t model described in the previous section, and a constant R_t equal to the spherical cavity expansion pressure. Good agreement is observed using the analysis described here. Note also that the calculated residuals based upon full strength values are far less than those observed in the experiments.

Table 3.1. Comparison of the effect of inclusion (variable R_t) and exclusion (constant R_t) of boundary effects in Cavity Expansion Analysis with experimental data and CTH for unconfined (UC) and radial confined (RC) alumina tiles, 2.586 cm thick backed by semi-infinite RHA, per Anderson et al. (1995)

Shot No.	Impact Velocity km/s	Residual Penetration, cm	CTH Calculated Residual, cm	Calculated Residual (varying R_t), cm	Calculated Residual (R_t = 8.5 GPa), cm
150UC-1	1.5	4.65	4.48	4.19	2.98
150UC-2	1.48	4.36	4.34	4.05	2.80
170UC-1	1.78	6.18	5.98	5.73	4.92
170UC-2	1.79	6.30	6.02	5.77	4.97
150RC-1	1.55	4.32	4.51	4.52	3.40
150RC-2	1.52	4.32	4.30	4.32	3.14
170RC-1	1.78	6.06	5.84	5.73	4.92
170RC-2	1.79	6.20	5.90	5.77	4.97

3.5.2 Discussion

In the above analysis, it was assumed that the ceramic tile was in perfect contact with the substrate. The acoustic impedances of AD995 alumina (41.1×10^6 $kgs^{-1}m^{-2}$) and steel (46.6×10^6 $kgs^{-1}m^{-2}$) are close. Thus, the reflected wave from the interface can be ignored. Often, a low impedance material (e.g., epoxy with acoustic impedance of 3.12×10^6 $kgs^{-1}m^{-2}$; Marsh 1980) is used as a bonding agent between the laminates. Presence of such a low impedance material would cause the compressive wave to reflect as a tensile wave from the interface. This would result in the appearance of cracked and comminuted zones ("reverse fracture") at the interface, which would propagate back towards the penetrator. If the thickness of the ceramic tile is sufficient, these "reverse fracture" zones will coalesce with the forward-moving cracked and comminuted zones. This phenomenology would certainly degrade the penetration resistance of the ceramic material. Such effects in thick ceramic tiles have been reported by Bless et al. (1995) and Hauver et al. (1992). Analysis of the phenomenology of "reverse fracture" would require

113

inclusion of the travel time of waves in the analysis. Hence, the penetration resistance model would have to be solved simultaneously with a penetration equation (e.g., the Tate equation) to obtain a time-dependent penetration resistance degradation. Such considerations were avoided in the above analysis and can be pursued in future work.

In summary, the model developed in this section shows the importance of interface effects in layered targets. Its predictions are in quantitative agreement with experiments. This analysis should be a valuable aid in designing ceramic armor and in interpreting DOP tests. However, it does not yet explain the experimental observation that in very thick tiles, average resistance is lower than predicted levels.

Chapter 4: Cavity Expansion Analysis and Penetration Models

There exists a number of models that, with varying degrees of success, are used to analyze penetration of solids by projectiles (Recht and Ipson 1963; Tate 1969; Donaldson and McDonough, 1973; Awerbuch and Bodner 1974; Walker and Anderson 1995; Forrestal 1995). The approaches in these models range from simple empiricism (Lanz and Odermatt 1992; Silby et al. 1989) to extremely complicated micro-mechanical hypotheses (Curran et al. 1990). While the more "first-principle" models attempt to capture the detailed mechanics, they require calibration and evaluation of a large set of parameters. Computational methods are required to solve their lengthy sets of non-linear equations. Often this is time consuming and expensive. It is not only difficult to identify the physics of the problem, but also use of numerical techniques may introduce other sources of non-physical errors. An alternative is to utilize analytic models arising out of simplified continuum mechanics principles and based on experimental observations, simulation results and experience. Such an approach can deliver a convenient tool for rapid estimation of complicated physical problems, although at the expense of some accuracy. It provides valuable insight into the role of individual parameters. The models discussed in this chapter belong to this second category.

The problems dealt herein are associated with semi-infinite target penetration (where the boundaries do not exert any significant influence). The thin plate perforation problem having typical application in space debris shielding, body armor design, etc., is excluded from the current analysis. The projectiles considered in this discussion are long rods, that are typical of military applications. No attempt has been made to explain the impact and cratering associated with short (small aspect ratio) or spherical projectiles.

In this Chapter, penetration phenomenology associated with high impact velocity is described first. Then the existing penetration models for both rigid and eroding penetrators, that use cavity expansion analyses, are discussed. Strengths and shortcomings of these models are pointed out. Subsequently, I introduce a hypothesis for ductile material behavior which leads to a new approach for modeling penetration. Cavity expansion solutions are used to describe the response of the target material. Several examples are shown to demonstrate the utility of this approach. The hypothesis introduced needs experimental verification.

4.1   Penetration phenomenology

A variety of phenomena exist in impact and penetration mechanics problems, e.g., shock formation, elastic-plastic wave propagation, fracture and fragmentation, thermal effects. This precludes a closed form analysis of the complete scenario. As a result, attempts have been made to identify different penetration regimes based on the dominant physical processes involved. Then simplifying assumptions are made in each regime so that analytical solution is possible. The solution, however, usually works only in the intended region of applicability.

Wierauch (1970) used a simple velocity scale to divide the regimes of impact and penetration phenomena where different mechanics of penetration predominates. Johnson (1972) used the non-dimensional number, $\rho V^2/Y$, where V is the relative speed at normal impact, ρ is the density and Y is the flow stress, as a damage number to delineate different penetration regimes ranging from quasi-static punching to hypervelocity penetration. This number, which is suggested by dimensional analysis (Shanbing et al. 1994), is the ratio of the inertial force to the mechanical strength and can be thought of as a measure of the order of strain imposed in the region where severe plastic deformation occurs (Zukas 1990). In this dissertation, attention has been given mainly to high velocity penetration problems, where the penetration velocity ranges from a few hundred m/s to a few km/s. In this regime, the Johnson's damage number is about 1 to 100, so the mechanical strength of the material can not be ignored compared to the inertial effects.

In the absence of a comprehensive mathematical model for high velocity penetration, phenomenological stages have been identified. The interface pressure history can be divided into four distinct regimes (Gehring et al. 1965). In the *transient shock regime*, at the instant of impact, spherical shock waves are formed. The pressure can be found from the Hugoniot relation as $P = \rho u_s u_p$, where u_s is the impact shock velocity, and u_p is the particle velocity. During this phase, a momentum field is established in the target. The duration of this transient shock regime is the time required for the rarefaction waves generated at the free surface to relieve the high shock pressure. If the projectile is long enough, in the *steady state regime* the kinetic energy in the projectile is dissipated under steady state penetration. The penetration behavior is similar to fluid flow, and hence Bernoulli's relation can be used to predict the interfacial pressure as, $P = \frac{1}{2}\rho u_p^2$. In the *cavitation phase,* the momentum transferred from the projectile to the target causes the crater to expand under inertia until the energy density falls below the material resistance level. Finally in

the *recovery regime,* after momentum in the target has been dissipated, the crater dimension reduces due to elastic rebound. This rebound may produce tensile stresses that may cause spallation failure. The high temperature to which the crater material has been subjected, can cause recrystallization beneath the crater.

Most of the penetration takes place in the steady-state regime under high-velocity impact of long rods, as has been observed in experiments and in numerical simulations. Thus, a great deal of attention has been focused on correctly modeling the mechanics of this regime. The widely used modified hydrodynamic models described below belong to this category.

4.2   Rigid body penetration

For low speed penetration of hard projectiles into relatively soft targets, the interaction stresses are not sufficient to deform the projectile which can be considered rigid. Historically, the resistive force in penetration of soft materials like sand and clay has been assumed to be a function of velocity. Work of Robins (1742), Euler (1750), Poncelet (1835) and Resal (1895) are noteworthy (see Johnson 1972). In Poncelet's equation the target resistance was taken to be of the form $A + BV^2$, which in conjunction with Newton's second law yielded the depth of penetration. The constants A and B were of empirical nature and were determined from the experimental data. It was not until the middle of this century that Hill (1948) derived essentially the same equation based on sound theoretical principles. Derivation of Hill's equation (Eq. 2.52) was presented in Chapter 2, which was based on the analysis of expansion of a spherical cavity from zero radius in an incompressible target continuum.

Goodier (1965) used the incompressible cavity expansion solution to predict the deep penetration of spherical steel projectiles into aluminum targets. While adapting Hill's dynamic cavity expansion solution to the penetration problem, Goodier scaled the dynamic term by $\cos(\theta)$ as a simple representation of the fact that the dynamic term should fall off to zero at the edge of the projectile. As a result, the axial force on the nose of the rigid sphere is given by

$$F_z = \pi a^2 \left\{ \frac{2Y}{3} \left[1 + \ln\left(\frac{2E}{3Y}\right) \right] + \rho_t \left[\frac{2}{3} a \frac{dv_z}{dt} + v_z^2 \right] \right\}. \tag{4.1}$$

117

Forrestal et al. (1995), on the other hand, argued that since the rigid projectile is in contact with the target material (found from posttest radiographs), the cavity expansion velocity, not the dynamic cavity pressure, should have a cosine variation so that the velocity is zero at the edge. Thus, for a long rod, the resistive force during penetration is given by

$$F_z = \pi a^2 \left\{ \frac{2Y}{3} \left[1 + \ln\left(\frac{2E}{3Y}\right) \right] + \frac{3}{4}\rho_t v_z^2 \right\}. \tag{4.2}$$

They then used a compressible cavity expansion model to show that compressibility cannot be ignored in modeling penetration of rigid long rods into aluminum targets. The agreement of their model with experimental data was very good. Forrestal et al. (1986, 1997) have also applied cavity expansion models to predict penetration into concrete and rock. Their results are in excellent agreement with experiments.

It should be noted that dependence of target resistance on acceleration, if any (e.g., in RHS of Eq. 4.1), can be recast into an apparent mass and included in the force term. Thus, for incompressible materials, the penetration resistance is essentially of the form $A + BV^2$. Cavity expansion analyses provide analytical expressions for the constants, A and B, that satisfactorily predict penetration by rigid projectiles (Forrestal et al. 1986, 1988, 1995).

For eroding projectiles, however, the connection between cavity expansion analysis and linear penetration is not obvious, since the projectile is not rigid, nor is it in contact with the target except at the tip. It shall be shown in the following that cavity expansion analysis can form an integral part of the penetration equation for such cases as well.

4.3   Eroding penetrator and modified hydrodynamic theory

At high impact velocities, the stress generated at the penetrator-target interface is sufficient to yield both the target and projectile. At a slightly higher velocity, the penetrator starts to erode during penetration. Hohler and Stilp (1990) summarize theoretical models for eroding rod penetration. They observed that it is very difficult or probably impossible to develop a physical model of general validity. Thus, there exists no analytical solution based on fundamental mechanics that models the entire erosion regime correctly. Most treatments make use of the modified hydrodynamic theory, which is based on some physics and some intuition. If the impact velocity is high enough, the material strength terms can be ignored compared to the inertial term (in

the regime of Johnson's damage number of 100, the strength is only one percent of the inertial term). Drawing upon experience with shaped charge jet penetration, it was assumed that, to first order, the long rod projectile can be thought of as a liquid jet penetrating another liquid medium. Then assuming one dimensional (along the streamline) steady state incompressible flow, ensuing Bernoulli's equation can be used to relate the stagnation pressures at the projectile-target interface as

$$P = \frac{1}{2}\rho_P(v-u)^2 = \frac{1}{2}\rho_t u^2,$$

(4.3)

where v and u are tail and tip velocities of the projectile respectively, ρ_p is the density of the projectile, and ρ_t is the density of the target. If the velocity at the tail and tip of the projectile are different, the projectile must shorten at the rate

$$\dot{l} = -(v-u),$$

(4.4)

where l is the current length of the projectile. Thus, integration of u dt from l = L to 0 yields the penetration depth, P which is given by

$$\frac{P}{L} = \sqrt{\frac{\rho_p}{\rho_t}},$$

(4.5)

where L is the initial length. This equation predicts that the penetration depth is proportional to the initial length of the projectile, irrespective of the impact velocity. Experiments show that this is unrealistic. This fixed ratio may be obtained only as a limit for very high velocities, where the strength can be ignored compared to the hydrodynamic inertial term; thus this limit was termed the "hydrodynamic limit."

In the 1960's, it was realized that for penetration of most structural materials by gun-launched projectiles, strength effects can not be ignored. Alekseevskii (1966) and Tate (1967, 1969) independently suggested that strength terms be added to both sides of Eq. (4.3). Thus,

$$Y_p + \frac{1}{2}\rho_P(v-u)^2 = \frac{1}{2}\rho_T u^2 + R_t,$$

(4.6)

119

where Y_p is the dynamic strength term of the penetrator and R_t is the strength of the target, should more accurately predict the penetration below the hydrodynamic limit. Initially, it was Tate's recommendation that R_t be the cavity expansion pressure for the target as calculated from Bishop, Hill and Mott's (1945) formula. Subsequently, in a recent paper, Tate (1986) used a solenoid model for incompressible fluid and derived a new estimate of R_t, which was somewhat higher than the cavity expansion pressure. In fact the experimental values of R_t lay between the above two values. Rosenberg et al. (1990) contended that cylindrical cavity expansion pressure can be used to estimate R_t. Anderson and Walker (1991) discuss various points of view associated with the estimation of R_t. The fact remains that in absence of an *ab-initio* approach, the static cavity expansion pressure gives a close estimation of R_t. Arguing that the penetrator is essentially decelerated by the dynamic strength, Y_p, Tate estimated the deceleration to be

$$\dot{v} = -\frac{Y_p}{\rho_p l}.$$ (4.7)

Thus, Eqs. (4.4), (4.6) and (4.7) can be integrated to obtain the penetration depth for given initial conditions.

This simple model captures most of the trends observed in penetration experiments. For $u = 0$, Eq. (4.6) indicates that there exists an impact velocity, v^*, below which no penetration is possible. For $u = v$, the rod can be considered to be rigid, since from Eq. (4.4), $\dot{l} = 0$, i.e. the penetrator does not erode. In this case, from Eq. (4.6), Y_p must be greater than R_t in order to achieve any penetration. For high enough impact velocity, this model indicates the existence of a hydrodynamic limit given by Eq. (4.5). The net result is, for cases where $R_t > Y_p$, an "s" shaped curve is obtained for the behavior of penetration to length ratio (P/L) with impact velocity, similar to experimental observations. Even though the experimentally observed trends are matched, for calculation of actual penetration, values of Y_p and R_t have to be varied with velocity. If suitable values of these constants are selected to match penetration at low velocity, penetration at high velocity is underpredicted. Later, Tate (1986) suggested that contributions from the initial transient phase and the final cavitation phase should be added to the steady state penetration to match the total penetration. However, this modification does not always give satisfactory agreement with experiments.

There have been several criticisms of Tate's approach (Wright 1981; Anderson and Walker 1991). First of all, the model is based on the assumption that a one dimensional (along the streamline aligned with the centerline) steady state incompressible flow pertains and thus the ensuing Bernoulli's equation can be used. Integrating the linear momentum equation along the centerline (z-direction), (initially shown by Wright 1981) Anderson and Walker (1991) derived the following equation.

$$\frac{1}{2}\rho_p(v-u)^2+\left\{-\sigma_{zz}(z_p)+2\int_{z_p}^{0}\frac{\partial\sigma_{zr}}{\partial r}dz\right\}=\frac{1}{2}\rho_t u^2+\left\{-\sigma_{zz}(z_t)-2\int_{0}^{z_t}\frac{\partial\sigma_{zr}}{\partial r}dz\right\} \qquad (4.8)$$

Here z_p and z_t are any two points on the centerline in the penetrator and the target, respectively, and r is the radial coordinate. Wright (1981) argued that even though the shear stress is zero along the centerline for normal penetration, its radial gradient is not zero. Thus to be able to reduce Eq. (4.8) to the Bernoulli's equation of the form given by Eq. (4.6), where Y_p and R_t are considered to be material constants, it must be demonstrated that the terms inside the curly brackets in Eq. (4.8) add up to constants.

Secondly, the value of R_t in Tate's equation is arbitrary. Even though the cavity expansion analysis gives a close enough estimation of R_t (at least for low penetration velocities), no rigorous connection between them has been worked out. To match the experimental data, R_t needs to be varied with velocity. Partom (1993) and Anderson et al. (1993) observed that R_t has to be reduced drastically for high velocity penetration to match the experimental data. In Partom's formula for R_t reduction, R_t can even become negative at high velocities. Tate (1986) suggested that the apparent discrepancy between the experimental data and the steady-state model can be accounted for by taking into consideration the initial transient phase and the final after-flow (cavitation) effects. Even with such modifications, Tate was unable to match the penetration data at both low and high velocities. In fact, Tate's secondary penetration formula is a function of velocity raised to the 2/3 power. Bless and Anderson (1993) pointed out that for long rods, the experiments clearly show that at high velocities, P/L ratios do not follow this afterflow trend described by Tate.

121

Thirdly, since the rod is in a one dimensional stress state, the coefficient of 1/2 appearing before the rod's inertia term seems to be appropriate. Since the target does not behave in a one dimensional fashion, but rather has a spherical quality associated with the stress behavior and the velocity distribution, the coefficient appearing in front of the target's inertial term should be somewhat less than 1/2 to reflect the confinement effect. Thus far, it has been tacitly assumed that the three dimensional confinement effect can be taken into account by suitably modifying the R_t value only. The possible confinement effect on the inertia term has not been considered. The velocity dependence of R_t camouflages the confinement effect on the one dimensional inertial term. Evaluation of Tate's model results in an "s" shaped penetration curve which is somewhat different from the "s" shaped curve obtained experimentally. No matter how Y_p and R_t are varied, it is impossible to match the experimental "s" shaped curve at both the lower and upper ends with the same set of Y_p and R_t. This points to the conclusion that the confinement effect on the inertial term must be explicitly taken into account.

Finally, the form of Bernoulli's equation used, applies only for incompressible flow. For high impact velocities, the pressure generated at the projectile-target interface can be very high (more than 10 GPa). At such high pressures, compressibility effects may not be negligible. Figure 4.1 shows how the relative density (ρ/ρ_0) changes with pressure for steel and tungsten. Two curves are plotted for each material: a linear hydrostat (for a constant bulk modulus) and the shock Hugoniot (the pressure-density relationship from plate-impact experiments, in which a shock is driven into the material). The shock equation and the constants used are from Asay and Shahinpoor (1993). It is seen that the density changes by more than 5% for pressures exceeding 10 GPa for steel and for pressure exceeding 20 GPa for Tungsten. However, since the densities of both the penetrator and the target increase with pressure (and hence with penetration velocity), it is possible that the net effect on penetration might cancel. Further study is required to quantify the effect of compressibility.
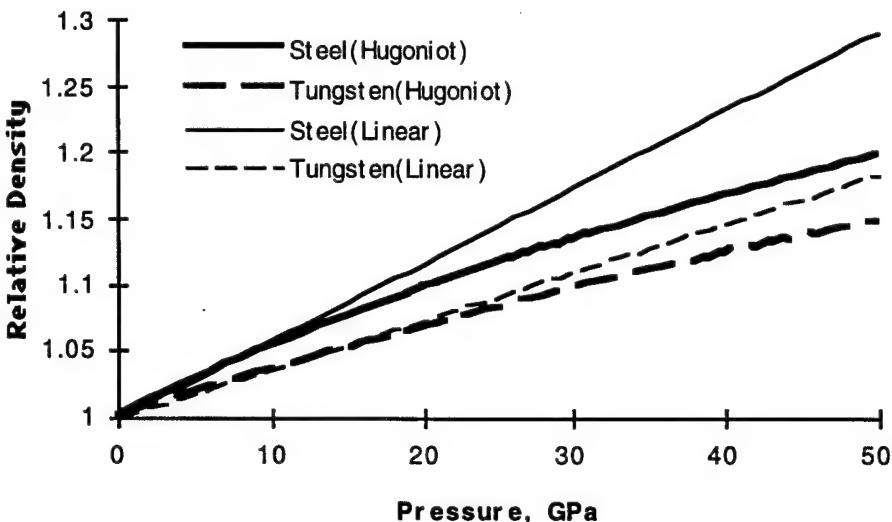
Figure 4.1. Pressure-density relation for Stainless Steel and Tungsten.

Other criticisms arise out of the steady-state assumption and use of elastic-perfectly plastic material behavior (Wright, 1983, 1988). However, numerical simulations and experimental evidence show that most of the high velocity penetration is in fact due to the steady-state phase. The analyses of the Taylor impact tests by Recht (1978) and Wilkins and Guinnan (1972) show that the work hardening effect in the typical armor materials at high strain rates is rather small. Bless (private communication) also points out similar experience with Hopkins pressure bar experiments. Cazamias and Bless (1997) conducted Taylor tests on armor steel and found that the strain rate effect on the flow stress can at best be logarithmic. They point out that logarithmic dependence of the flow stress would result in barely perceptible changes in penetration.

In spite of the above limitations, Tate's approach appears to be a good baseline penetration model in the eroding rod regime, since it provides the correct trend with experimental data even though quantitative predictions are often unsatisfactory.

4.4 Walker-Anderson model

Recently, Walker and Anderson (1995) have developed a more fundamental approach to deriving a penetration model. Figure 4.2 shows the assumed penetrator and target response regions. z_p and z_i locate the tail and the tip of the penetrator at all times, where the velocities are v and u, respectively. The penetrator has a plastic zone of size S that grows with time. The target

has a plastic zone surrounding the penetration cavity; this plastic zone bears a ratio, α, with the cavity radius, R. The target was considered to be semi-infinite.
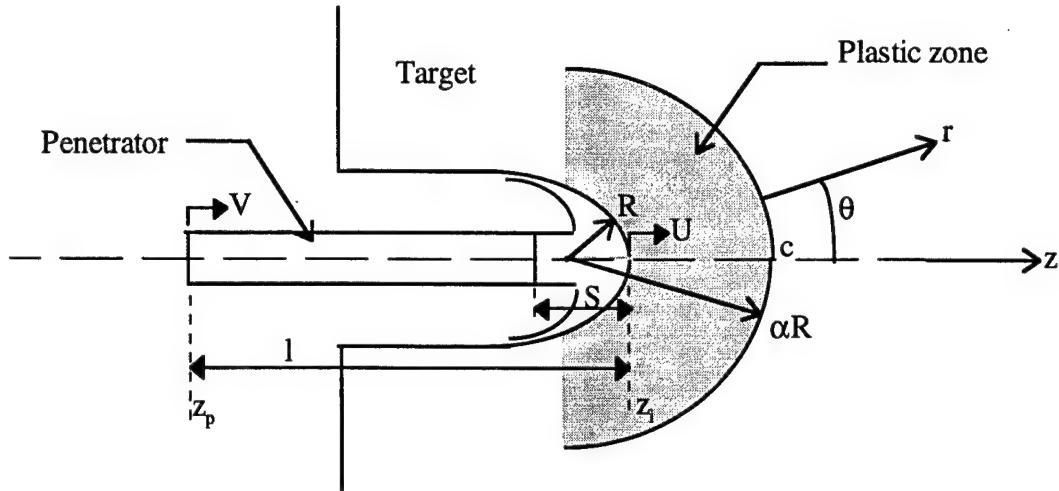
Figure 4.2. Response regions in the Walker-Anderson Model

Using the axi-symmetry condition, they wrote the Eulerian momentum equation along the center-line (z-direction), as follows.

$$\rho\frac{\partial u_z}{\partial t} + \frac{1}{2}\rho\frac{\partial u_z^2}{\partial z} - \frac{\partial \sigma_{zz}}{\partial z} - 2\frac{\partial \sigma_{xz}}{\partial x} = 0 \tag{4.9}$$

Integrating the above equation from z_p to ∞ with the assumption that density changes are sufficiently small, to justify the extraction of density terms from the integrals, they obtained,

$$\rho_p\int_{z_p}^{z_i}\frac{\partial u_z}{\partial t}dz + \rho_t\int_{z_i}^{\infty}\frac{\partial u_z}{\partial t}dz + \frac{1}{2}\rho_p\left(u^2 - v^2\right) - \frac{1}{2}\rho_t u^2 - 2\int_{z_p}^{\infty}\frac{\partial \sigma_{xz}}{\partial x}dz = 0. \tag{4.10}$$

To evaluate the integrals in the above equation, velocity and stress distributions were required. They assumed the following velocity distribution for the penetrator.

$$u_z(z) = \begin{cases} u - \dfrac{v - u}{s}(z - z_i) & (z_i - s) \le z < z_i \\ v & z_p \le z < (z_i - s) \end{cases} \tag{4.11}$$

124

The portion of the rod beyond the plastic zone, S, was considered to be elastic. The elastic wave (with a stress amplitude equal to Y_p, the flow stress of the rod) that was generated at the instant of impact, bounces back and forth between the elastic-plastic front and the rear of the rod. Each reflection at the rear of the rod reduces the projectile velocity. Dividing the step change of velocity associated with elastic wave reflection at the rear boundary by the transit time for each reflection, they derived the following equation for projectile deceleration.

$$\frac{dv}{dt} = -\frac{Y_p}{\rho_p(1-s)}\left[1 + \frac{v-u}{c_e} + \frac{\dot{s}}{c_e}\right].$$

(4.12)

Here c_e is the elastic bar wave speed for the rod. Furthermore, since the tail and the tip of the penetrator have different velocities, the erosion rate is given by

$$\dot{l} = -(v-u).$$

(4.13)

They considered the target material to be incompressible. Numerical simulations showed that the flow in the target material had a spherical quality associated with it. Consequently assuming incompressibility, they showed that the velocity in the flow region that best describes the numerical result is the curl of a velocity potential (whose divergence is zero to automatically satisfy the incompressibility condition) of the form

$$\vec{A} = f(r)\sin(\theta)\hat{e}_\phi \, ,$$

(4.14)

where $f(r)$ is a suitable function describing r-dependence. Taking the curl of this vector in spherical coordinates, one obtains the following expressions for radial and azimuthal velocities in the target:

$$u_r(r,\theta) = \frac{2f}{r}\cos(\theta),$$

(4.15)

$$u_\theta(r,\theta) = -\frac{1}{r}\frac{d(rf)}{dr}\sin(\theta).$$

(4.16)

The function, $f(r)$ was taken to be of the form

$$f(r) = \frac{ur\left[\left(\frac{\alpha R}{r}\right)^2 - 1\right]}{2(\alpha^2 - 1)},$$

(4.17)

where α is the extent of plastic zone in the target. They further showed that for a perfectly plastic material having a velocity distribution derivable from a potential of the form given in Eq. (4.14), use of the von Mises yield criterion results in the following.

$$\int_R^{\alpha R} \frac{\partial \sigma_{xz}}{\partial x} dz = -\frac{7}{6} \ln(\alpha) Y.$$

(4.18)

Y is the flow stress. Here the integration is performed along the center-line. This result is independent of the form of the function f(r). Inserting Eqs. (4.11), (4.12), (4.15) and (4.18) into Eq. (4.10), they obtained

$$\rho_p \dot{v}(L-s) + \dot{u}\left\{\rho_p s + \rho_t R \frac{\alpha - 1}{\alpha + 1}\right\} + \rho_p \left(\frac{v-u}{s}\right)\frac{s^2}{2} + \rho_t \dot{\alpha}\frac{2Ru}{(\alpha + 1)^2}$$
$$= \frac{1}{2}\rho_p(v-u)^2 - \left\{\frac{1}{2}\rho_t u^2 + \frac{7Y_t}{3}\ln(\alpha)\right\}$$

(4.19)

Moreover, for incompressible materials, the condition that the derivative of the velocity normal to the contact surface is continuous gives an additional equation for s. These form a complete set of differential and algebraic equations that can be integrated for given initial conditions. They derived the initial value of u from shock equations. An equation for R is required, which they obtained from the experimental data for the given pair of penetrator and target. They plotted their result for constant values of α derived from spherical and cylindrical cavity expansion analyses. Recognizing that a constant α does not result in good agreement with the experimental data for different velocities, they used the compressible dynamic cylindrical cavity expansion solution to derive a velocity-dependent α. Using a heuristic expression for stiffening of bulk modulus with velocity, they obtained good agreement with experimental data.

The Walker-Anderson model is a more fundamental approach to a penetration model than the modified hydrodynamic theories discussed in the previous section. Many trends observed in experiments and numerical simulations were incorporated into this model. This time-dependent model captured the initial unsteady behavior in the penetration velocity. However, the solutions' showed that the bulk of the penetration is due to the steady-state. They showed that under certain restrictive conditions, Eq. (4.16) reduces to a Tate-like penetration equation. Additionally, their result for the integral of the shear stress gradient, Eq. (4.18) seems to be a fundamental solution and addresses one of the concerns of Wright (1981) regarding inclusion of such an integral in the momentum balance equation.

There are a few limitations of this model. Firstly, the cavity radius, R, needs to be known *a priori* for the given pair of materials. This restricts the predictive capability of the model. Secondly, even though the integral of shear stress gradient was calculated for an incompressible condition, they had to use a heuristic compressible solution for α. This seems inconsistent, since the solution of the form given by Eq. (4.18) may not be valid for compressible material. Additionally, the use of a cylindrical cavity expansion solution for a region having spherical quality for flow seems unreasonable. Use of a spherical cavity expansion solution instead seems preferable. Thirdly, their assumed velocity distribution in the target was scaled in such a way that the radial velocity became zero at $r = \alpha R$, whereas for spherical symmetry, the velocity should drop of as $1/r^2$ throughout the target. This scaling results in an unusual feature in the distribution of u_θ as well. From Eqs. (4.16) and (4.17), u_θ is given by, $u_\theta = u\sin(\theta)/(\alpha^2 - 1)$. This implies that at $\theta=\pi/2$, the target material flows back at the constant speed $u_\theta = u/(\alpha^2 - 1)$ throughout the plastic region, which extends for about 5 times the cavity radius ($\alpha\cong5$) at low speeds and for about 2 times the cavity radius ($\alpha\cong2$) at high speeds. This behavior seems somewhat nonphysical.

4.5   Eroding penetrator: A new approach based on cavity expansion theory

Based on the results of the models for eroding rod penetration described above, a new approach is presented below. Figure 4.3 shows different response regions.
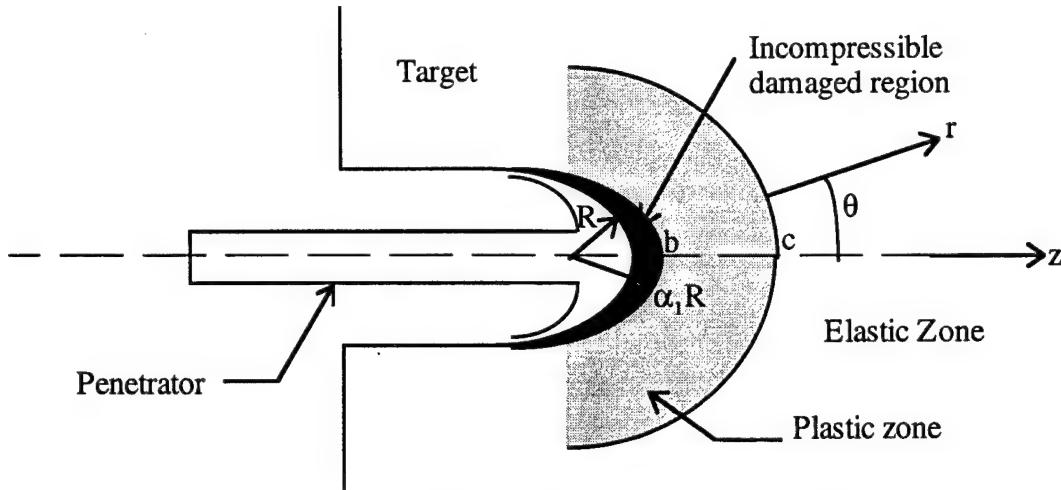
Figure 4.3. Different zones in the target.

The following assumptions are made:

1. The state of stress in the penetrator is one-dimensional.
2. The stress and velocity distributions in the target have spherical quality.
3. In the target, there exists a small "damaged zone" surrounding the cavity ($z = a$ to $z = b$) where material is extremely deformed. Extensive shear-flow is limited to this zone. The density in this region stays constant and is equal to the density (higher than the original density) at the damaged-plastic zone boundary, $z = b$.
4. Response of the target material is elastic-perfectly plastic. The plastic and elastic regions are compressible with a linear compression behavior.

Discussion of the assumptions:

Since in the following analysis penetration by long rods with large aspect ratios are considered, assumption (1) seems reasonable. Numerical simulations by Walker and Anderson (1995) show that the stress and velocity distributions in the target have spherical qualities. Thus the assumption (2) seems reasonable too.

Assumption (3) hypothesizes existence of a small "damaged zone" surrounding the penetration cavity. As the rod penetrates at high velocity, it erodes. The eroded rod material flows out of the path of the rod. This flow exerts a high shear stress on the wall of the cavity in the target. Additionally, the target material in the immediate vicinity of the interface experiences very

128

high pressure. As one proceeds from the elastic-plastic boundary towards the penetration cavity, the amount of plastic strain experienced by the target material increases. Plastic strain is mainly associated with dislocation motion, climbing of dislocations and twinning. During severe dislocation motion, if one dislocation stops at a micro-stress concentration such as micro defects or grain boundaries, other dislocations pile up, creating a micro crack and thus debonding (Lemaitre 1992). This process is called ductile damage evolution. The amount of ductile damage depends on the amount of plastic strain present. As the damage process continues, a critical stage is reached at which the material experiences an unstable state. Further shear deformation is possible only in a compression state, since under tensile conditions, void nucleation and linkup will cause macro-scale fracture and structural failure. Under compression conditions, upon attainment of some critical damage condition, localization phenomena may occur in the micro-scale, depending on the constitution of the material. Possible examples could be plastic instability resulting in extensive shear flow in the form of deformation bands or shear bands, change of phase due to very high pressure and temperature experienced, inter and intra-granular fracture and flow due to saturation of dislocation motion, recrystallization, etc. In a penetration situation, this would lead to a small process-zone in the target, in which the target material is severely strained and flows out of the way of the penetrator. I denote this region as the "damaged region."

Tham et al. (1980) observed such a small region below the crater in mild steel in high velocity impact tests (see Figure 4.4). In addition to gradation of grain size due to recrystallization, they found distinctly different behavior of hardness in the inner region (process-zone) and the outer zone. The hardness increased from the crater-wall in the direction of penetration in the inner region. At the boundary between the inner and outer regions, it dropped down suddenly and continued to decrease away from the boundary. Huang et al. (1996) found that near the penetration channel in RHA, severe micro-structural distortions existed in a region of size of about one penetrator radius. Of course, these observations are not conclusive, and further experimental studies are required to establish the existence of a process zone. Lemaitre (1992) suggested several testing methods to measure damage in ductile materials, such as micrography, micro-hardness testing, electrical resistance measurement, measurements of ultrasonic waves, etc. Such tests should help to characterize the damaged region.
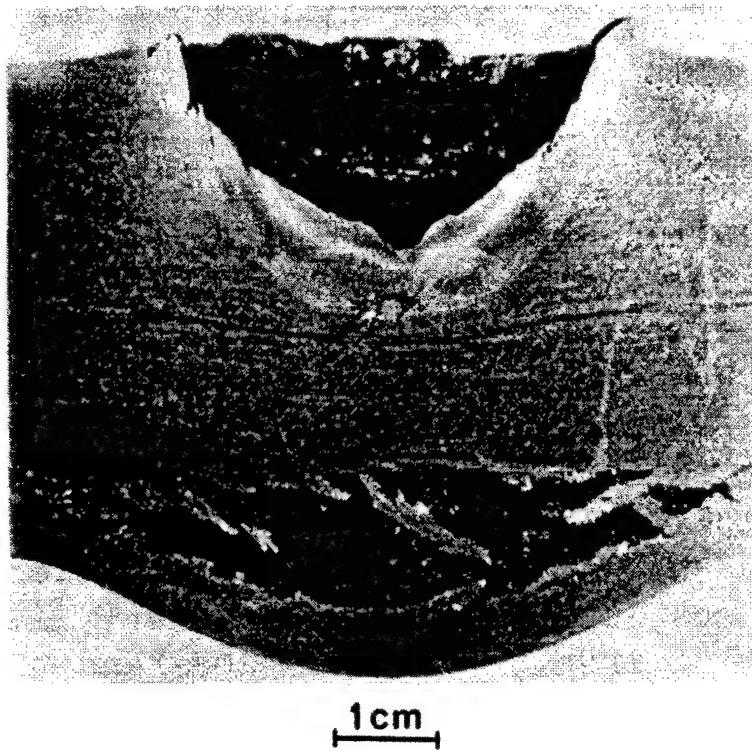
Figure 4.4. Sectioned target in Tham et al.'s (1980) experiment.

If the energy associated with hydrostatic compression is neglected compared to the energy required for extensive microstructural distortion and deformation flow in the damaged region, the change in density should be negligible. This assumption enables us to use the shear gradient integral derived by Walker and Anderson (1995) for incompressible material. Additionally, since shearing is assumed to be restricted to this region, the surrounding region can be modeled by a compressible cavity expansion solution for which the shear stress in the inner boundary is assumed to be zero.

By virtue of the fourth assumption, the dynamic cavity expansion solution of Forrestal and Luk (1988) for a compressible elastic-plastic material with a linear compression behavior can be utilized.

4.5.1 Model for the rod

Consider a long rod penetrator (with a high aspect ratio) penetrating a semi-infinite target. Let the impact velocity be high enough that the pressure existing at the penetrator/ target interface

130

exceeds the yield strength of both the projectile and target materials. Upon impact, an elastic and a plastic wave will propagate into both the rod and the target. In the rod, the elastic wave will travel at the bar wave speed [$= \sqrt{(E/\rho_p)}$]. If the material work hardens, the plastic wave speed is the square root of the ratio of tangent plastic modulus and the density. For metals, the plastic wave speed is more than one order of magnitude smaller than the elastic wave speed. Models of Taylor impact test (Zukas 1990) serve as useful guides in modeling the wave interaction in the rod. Wilkins and Guinan (1972) found that for typical metals, the extent of plastic zone for any impact velocity and any initial length of the rod is a fixed fraction ($= 0.12$) of the initial rod length. Even though there exists no mathematical explanation for this ratio, its existence points to the fact that the plastic zone front is stationary with respect to the stagnation point. Tate (1986) argues that during penetration, if the erosion rate is higher than the plastic wave speed, a shock will stand at the interface (i.e., s in the Walker-Anderson model is zero), while the rest of the rod is elastic. Thus, if one assumes that the stress that decelerates the elastic part of the rod is the yield strength, Y_p, application of Newton's second law yields

$$\frac{dv}{dt} = -\frac{Y_p}{\rho_p l}. \tag{4.20}$$

Since the projectile has different velocities at its tip (u) and tail (v), it must erode at a rate

$$\dot{l} = -(v - u). \tag{4.21}$$

From the Walker-Anderson model, for s = 0, the stress at the penetrator-target interface is given by,

$$\sigma_z(a) = -\frac{dv}{dt}\rho_p l + \frac{1}{2}\rho_p(v - u)^2, \tag{4.22}$$

where stress is taken to be positive in compression. From Eqs. (4.20) and (4.22), the axial stress at the interface is given by

$$\sigma_z(a) = Y_p + \frac{1}{2}\rho_p(v - u)^2. \tag{4.23}$$

This equation can also be derived by attaching a moving coordinate system to the interface and integrating the linear momentum equation.

4.5.2 Target model

If the interaction stress is greater than the yield strength of the target material, the target will deform plastically. The flowing eroded rod material applies shear stress in the hoop direction to the cavity in the target, in addition to the radial stress induced by the interfacial pressure. The target material exhibits three distinct zones: an elastic zone spreading out at the longitudinal sound speed, followed by a plastic zone, where the material has yielded, propagating at a speed lower than bulk sound speed, and finally a zone of incompressible damaged material, in which shear-flow in the hoop direction is restricted. The damaged zone may be thought of as zone of extensive shear, in which the target material is pushed aside to create an instantaneous penetration cavity. This cavity is subsequently expanded by inertia and momentum of the failed rod and target materials to attain the final cavity size. There are a few models that attempt to calculate the cavity diameter (Tate 1986; Bless and Lee 1995; Scott 1984). Recently, Raftenberg (1994) presented experimental and numerical studies of holes formed by shaped charge jets. The present analysis is not concerned with predicting the cavity diameter, since this should be an outcome of a penetration model in association with either energy balance (Tate) or with dynamic equilibrium (Bless and Lee). In passing, it may be noted that at the velocities considered here (2 to 3 km/s), the cavity diameter in RHA steel is of the order of twice the tungsten penetrator diameter (Raftenberg and Kennedy, 1995). This could be due to the fact that the rod turns inside out during complete erosion. But if one recognizes the facts that: a) the eroded rod material can either travel forward or backward with respect to the interface, depending on the penetration velocity, and b) the momentum imparted to the wall of the penetration channel causes subsequent hole growth, this factor can be substantially different from 2.

Following Walker and Anderson (1995), a velocity potential of the form given by Eq. (4.14) is assumed for the incompressible damaged zone. The resulting velocities are given by Eqs. (4.15) and (4.16). It was shown in the last section that Walker and Anderson's assumed function, f(r) resulted in unsatisfactory behavior of the target material velocities. To avoid these difficulties, I assume that the function f(r) has the following representation.

$$f(r) = \frac{uR^2}{2r} \tag{4.24}$$

Substitution of Eq. (4.22) into Eqs. (4.16) and (4.17) result in the velocities,

$$u_\theta = 0 \text{ and } u_r = u \cos(\theta)(R/r)^2. \tag{4.25}$$

This means that the material only flows in the radial direction and does not flow back. Viewed from a moving coordinate system attached to the interface, the target material flows sideways and backwards, as observed in numerical simulation of Batra and Wright (1986). Additionally, this radial velocity is consistent with Forrestal et al.'s (1995) velocity distribution for a rigid rod penetration model and satisfies the desired conditions that radial velocity should be maximum at the center line and should drop to zero at the edge. This velocity distribution is applicable in the incompressible damaged region and serves as the inner boundary condition for the compressible plastic region, which I shall model using compressible cavity expansion theory.

Taking stresses positive in compression, the equation of motion along the center line can be written in Eulerian form as

$$\frac{\partial \sigma_z}{\partial z} + 2 \frac{\partial \sigma_{xz}}{\partial x} = -\rho \left(\frac{\partial u_z}{\partial t} + u_z \frac{\partial u_z}{\partial z} \right). \tag{4.26}$$

The density in the damaged region is assumed to be constant at a level attained at the damaged-plastic zone interface, $z = b$. Along the center line of penetration, the axial coordinate z is equivalent to the spherical coordinate r. Integrating the above equation from a ($r = R$) to b ($r = \alpha_1 R$), one obtains

$$\sigma_z(b) - \sigma_z(a) + 2 \int_R^{\alpha_1 R} \frac{\partial \sigma_{xz}}{\partial x} dz = -\rho_b \int_R^{\alpha_1 R} \left(\frac{\partial u_r}{\partial t} + u_r \frac{\partial u_r}{\partial r} \right) dr, \tag{4.27}$$

where ρ_b is the density at the damaged-plastic interface, $z = b$. Walker and Anderson (1995) have shown that for a perfectly plastic material obeying the von Mises yield criteria with a velocity

distribution derivable from any potential of the form Eq. (4.14), the integral of the shear stress gradient in Eq. (4.27) takes the elegant form

$$\int_{R}^{\alpha_1 R} \frac{\partial \sigma_{xz}}{\partial x} dz = -\frac{7}{6} \ln(\alpha_1) Y_t.$$ (4.28)

What is remarkable about this solution is that the result is independent of the function f(r) in Eq. (4.14) and depends only on the extent of the zone where the integration is carried out. Inserting the velocity distribution arising out of Eqs. (4.14) and (4.24) into the right hand side of Eq. (4.27), one obtains

$$\int_{R}^{\alpha_1 R} \left(\frac{\partial u_r}{\partial t} + u_r \frac{\partial u_r}{\partial r} \right) dr = \int_{R}^{\alpha_1 R} \left(\frac{2uR\dot{R}}{r^2} - \frac{2uR^4}{r^5} \right) dr$$

$$= \frac{1}{2} u^2 \left[3 + \frac{1}{\alpha_1^4} - \frac{4}{\alpha_1} \right],$$ (4.29)

where the fact that $\dot{R} = u$ has been used. Now, insertion of Eqs. (4.28) and (4.29) into Eq. (4.27) yields

$$\sigma_z(a) = \sigma_z(b) + \frac{7}{3} \ln(\alpha_1) Y + \frac{1}{2} \rho_b u^2 \left[3 + \frac{1}{\alpha_1^4} - \frac{4}{\alpha_1} \right].$$ (4.30)

$\sigma_z(b)$ is the stress required to push the plastic front at the average velocity, $u_b = u/2\alpha_1^2$ (average of $u \cos(\theta)/\alpha^2$ on a spherical surface), given by the assumed velocity distribution. It was shown in Section 3.4.1.1 that taking this average velocity as the cavity expansion velocity implies that the work required for a given penetration is the same for linear penetration and spherical cavity expansion. Forrestal and Luk (1988) have shown that for spherical symmetry, the cavity expansion pressure, σ_{cav}, for an elastic-perfectly plastic material is a function of cavity expansion velocity and the material parameters, i.e., $\sigma_{cav} = \sigma_{cav}(u, M)$ where M denotes the material constants. The equations required to derive this dynamic cavity expansion pressure were presented in Chapter 2 (Eqs. 2.53 to 2.56). Since, a linear pressure-volume relation is assumed for the plastic region, the density at the damaged-plastic zone is given by

134

$$\rho_b = \frac{\rho_0}{1 - P/K}$$

$$= \frac{\rho_0}{1 - (\sigma_r + 2\sigma_\theta)\big|_{z=b}/3K}$$

$$= \frac{\rho_0}{1 - (3\sigma_{cav} - 2Y_t)/3K}. \tag{4.31}$$

since $\sigma_r - \sigma_\theta = Y_t$. Here ρ_0 is the initial density, P is the hydrostatic pressure at z = b, and K is the bulk modulus.

Now since the axial stress must be continuous at the penetrator-target interface, z = a, from Eqs. (4.23) and (4.31) I obtain,

$$Y_p + \frac{1}{2}\rho_p(v - u)^2 = \sigma_{cav}(u/2\alpha_1^2) + \frac{7}{3}\ln(\alpha_1)Y_t + \frac{\frac{1}{2}\rho_0 u^2}{1 - (3\sigma_{cav} - 2Y_t)/3K}\left[3 + \frac{1}{\alpha_1^4} - \frac{4}{\alpha_1}\right]. \tag{4.32}$$

Solution of Eqs. (4.17), (4.18) and (4.32) along with the cavity expansion solution contained in Eqs. (2.53) through (2.56) results in the depth of penetration for given initial conditions and a given value for α_1. To give a physical interpretation to α_1, it can be related to the strain at $\alpha_1 R$. From Eqs. (2.20) and (2.22), α_1 can be related to the radial strain at r = $\alpha_1 R$, defined as $\varepsilon_{\alpha 1}$, as follows:

$$\alpha_1 = \left[1 - e^{(-3\varepsilon_{\alpha_1}/2)}\right]^{-\frac{1}{3}}. \tag{4.33}$$

For $\varepsilon_{\alpha 1}$ = 0.2 and 0.3, evaluating Eq. (4.33) one obtains α_1 = 1.57 and 1.4, respectively. These strain values are typical failure strains for armor materials obtained from one-dimensional compression tests (Recht 1978). For these values of α_1 the damaged region is about one penetrator radius deep since the cavity radius, R, is about twice the penetrator radius. Thus $\varepsilon_{\alpha 1}$ may be used to denote the critical damage strain, since it defines the extent of the damaged region.

In Figure 4.5, the equivalent R_t term in Eq. (4.29) (equivalent R_t is the RHS of Eq. (4.30) minus $\rho_0 u^2/2$) is plotted for two cases: (a) $u_b = u/\alpha_1^2$ (cavity expansion velocity = centerline velocity of damaged/ plastic zone interface) and (b) $u_b = u/2\alpha_1^2$ (cavity expansion velocity =, average velocity of damaged/ plastic zone interface). The critical damage strain, $\varepsilon_{\alpha 1}$ is taken to be 0.2. In the same figure, Partom's (1993) velocity-dependent R_t that matches Silsby's (1989) experimental data, is also plotted. Partom's formula, which was based on impact velocity, was modified by using Eq. (4.6) to make it a function of penetration velocity, u. Case (a) is strictly true along the center-line, where $u_b = u/\alpha_1^2$. Radial confinement effect on the inertial term has not been accounted for. As a result, this case yields a nearly constant R_t, as assumed in Tate's one dimensional modified Bernoulli's equation. Case (b) shows a close match with Partom's formula and thus with experimental data. Thus it appears that the analysis described in this chapter is able to model the inertial effects in the target correctly.
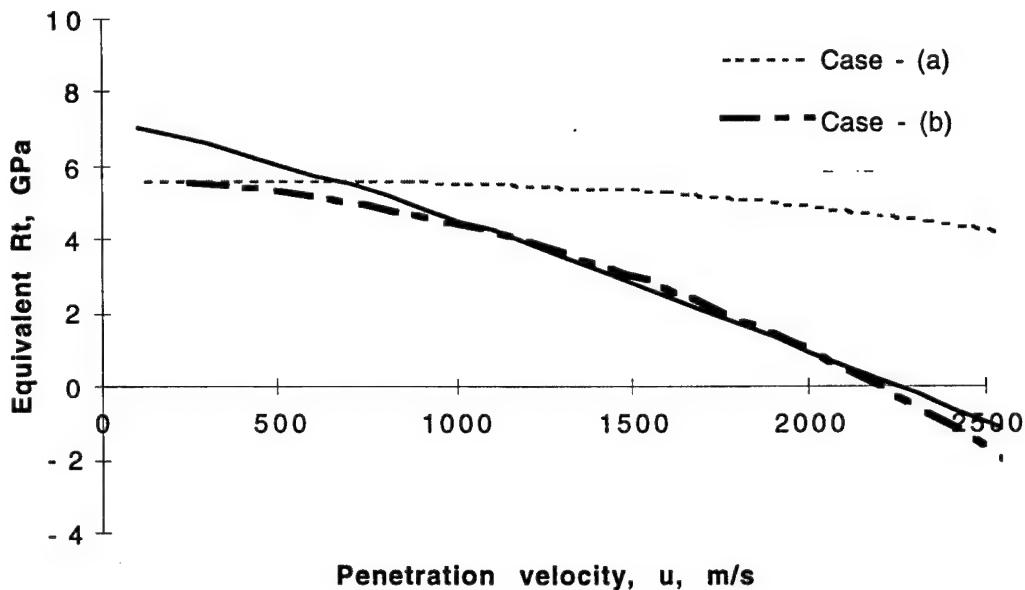
**Figure 4.5.** Comparison of equivalent Rt predicted from the penetration theory with observed trend based on experiments.

4.5.3 Comparison with experiments

I now proceed to compare the prediction from the above penetration analysis based on cavity expansion theory, with the experimental data of various researchers. In evaluating Eqs. (4.17) and (4.32), the dynamic flow stress of the materials needs to be established. Recht's

(1978) formula shall be used to determine these terms for high strain rate conditions. He plotted the dynamic yield strength data for several metals versus their Brinnel Hardness Number for experiments at a strain rate of about 1000/s and for 4340 steel at strain rates varying from 500/s to 10,000/s . By curve fitting, he found that the following correlation represents the dynamic yield· strength, σ_{dyn}, accurately enough.

$$\sigma_{dyn} = 3.92 \times BHN + 4.55 \times BHN \times \varepsilon_p \qquad (4.34)$$

Here ε_p is the plastic strain and BHN is the Brinnel Hardness Number. Eq. (4.34) can be used to evaluate the dynamic yield strength of the target and projectile material for a given ε_p. Recht's results showed that hard metals like 4340 steel typically failed at a strain of about 0.2. This value of strain is used in the following examples to calculate the dynamic flow stress of steels. A strain value of 0.1 is assumed for tungsten.

In Figure 4.6, Hohler and Stilp's (1992) experimental data are compared with the predictions from the penetration theory. The experiments were performed using L/D = 10 tungsten penetrators and St52 steel targets. The BHN for the penetrator and target materials were 294 and 180, respectively. The theoretical curve for $\varepsilon_{\alpha 1} = 0.3$ for the target material matches the experimental data reasonably well. Since softer material are tougher and more ductile, strain at failure should be higher compared to the harder materials (0.2 for 4340 steel with BHN~250). Thus the optimum value for $\varepsilon_{\alpha 1}$ follows the reasonable trend of increasing with decreasing hardness.
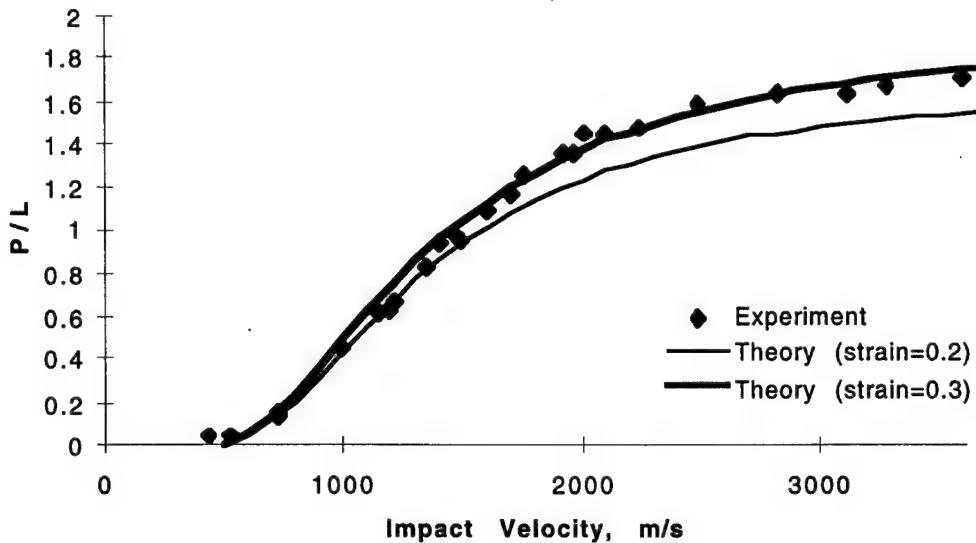
Figure 4.6. Comparison between penetration theory and experimental data for St52 from Hohler and Stilp (1992).

In Figure 4.7, the theoretical curves are plotted along with data from Silsby (1984) and Hohler and Stilp (1992) for penetration by tungsten alloy (BHN~352) into hard steel (BHN~230–300). For steel, BHN = 250 is used. As expected, a lower $\varepsilon_{\alpha1} = 0.2$ compared to that for the softer steel in the previous example agrees with the experimental data.

Finally the predictions from the theory are compared with the experimental data from the IAT (Institute for Advanced Technology) data base (Bless 1997) for long rods (L/D~20 to 30). This comparison is of greater significance, since for high L/D ratios, the end effects should be minimal. In the calculations, target hardness of 250 BHN and projectile hardness of 350 BHN were used. As seen in Figure 4.8, the theoretical curves with $\varepsilon_{\alpha1} = 0.2$ and $\varepsilon_{\alpha1} = 0.3$ reasonably agree with the wide variety of experimental data. Considering the experimental scatter of the data (due to the variation in BHN of target and projectile materials), the agreement is rather good.
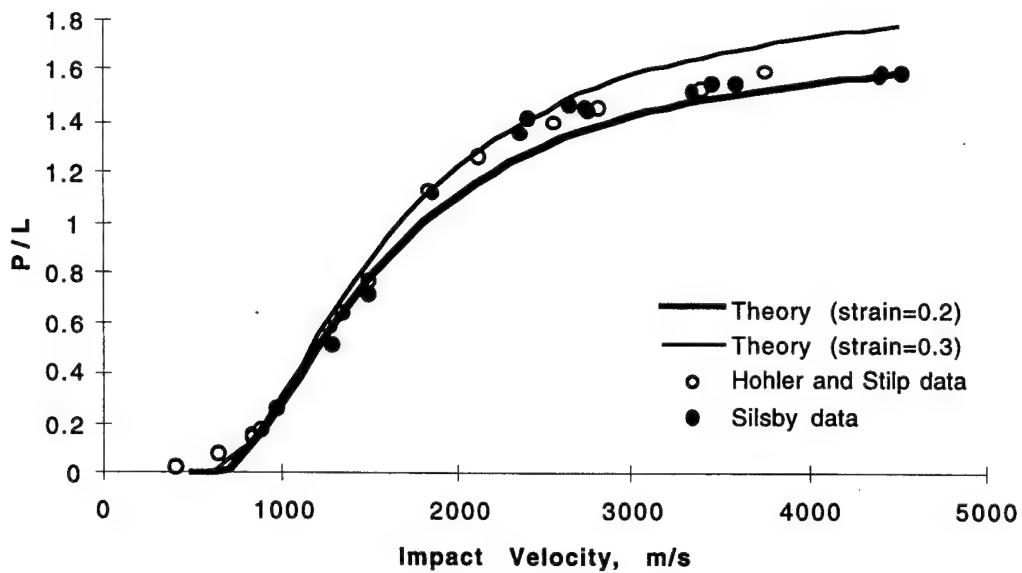
Figure 4.7. Comparison between penetration theory and data from Silsby (1984) and Hohler and Stilp (1992).
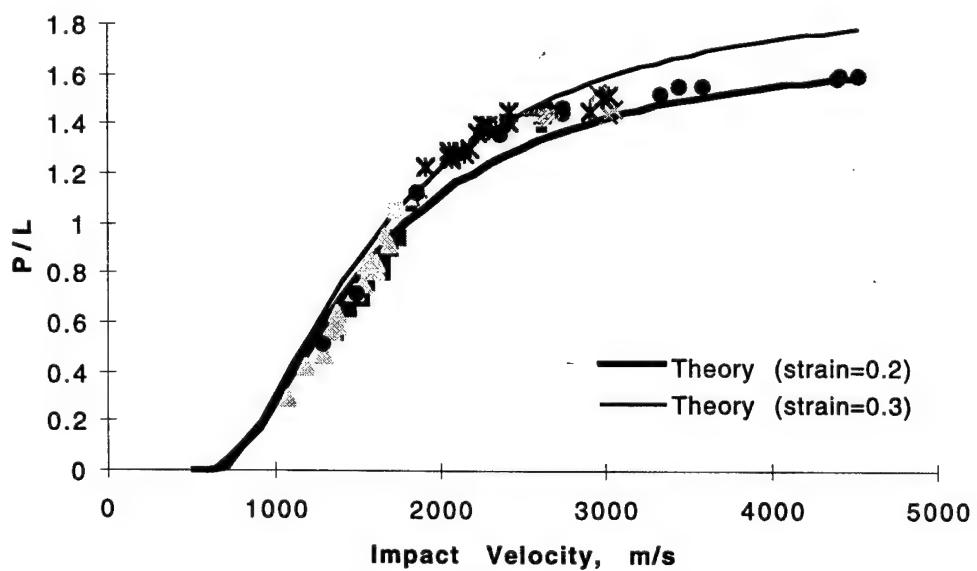
Figure 4.8. Comparison between penetration theory with IAT's long rod data base.

The examples cited above indicate that penetration continues to increase with velocity and has not reached "hydrodynamic limit," as suggested by the existing models. This is due to the fact that the inertial term in the RHS of Eq. (4.32) does not have a velocity squared dependence. The suggested theory agrees reasonably with a wide variety of experimental data both at the low and

139

high velocity regimes. This is achieved at the expense of introducing a new parameter, α_1 (equivalently $\varepsilon_{\alpha 1}$). Reasonable values for $\varepsilon_{\alpha 1}$, those comparable to the failure strains in one-dimensional compression tests, are used. At the low velocity end, the result is not very sensitive to $\varepsilon_{\alpha 1}$. At higher velocities, where high levels of stresses are prevalent, the values of $\varepsilon_{\alpha 1}$ used indicate acceptable sizes for the damaged region. Furthermore, a constant value for α_1 is used for all velocities. It is likely that critical damage strain, $\varepsilon_{\alpha 1}$, will change with impact velocity due to effects of high compressive hydrostatic pressure. The trends observed in the above examples support a variation in $\varepsilon_{\alpha 1}$.

Chapter 5: Summary, Conclusions, and
Future Work

5.1 Summary of work completed

The historical and theoretical backgrounds of cavity expansion analyses as a means to model projectile penetrations have been thoroughly reviewed. In the last few decades, solutions have become available for elastic plastic targets and simple brittle materials penetrated by rigid projectiles. However, the steps to model more realistic material behavior, consistent with contemporary understanding, as well as the consequences of projectile erosion, were yet to be made. These considerations provided a motivation and a framework for the current work.

Phenomenology of "classical" cavity expansion was experimentally examined by quasi-static punch tests on PMMA. A cavity expansion solution was worked out using published theories, and it was found that using a single value for the friction coefficient, the experimental data for spherical and conical punches were accurately predicted both before and after the embedment of the tip. The measured size of the plastic zone was reasonably predicted by the cavity expansion solution. Thus confidence was established in traditional solutions for plastic targets.

Conventional elastic-plastic solutions were extended to quantitatively determine the effects of a finite boundary on the penetration resistance of metallic targets. The solution successfully explained the experimentally observed degradation of the penetration resistance in small samples.

Cavity expansion analysis for metals was extended to include a new brittle behavior not previously considered—cracking due to tensile strain. Titanium, an important current target material, exhibited this behavior. Experiments conducted at IAT were modeled. The size of the cracked region and the penetration resistance value were well explained by the theory.

In recent years, new ideas have emerged about the nature of the failed region during penetration of brittle materials. Based on these concepts, the quasi-static cavity expansion problem for brittle materials was solved for both spherical and cylindrical symmetries, assuming a Mohr-Coulomb-type failure behavior. Material parameters, evaluated by other researchers from different experiments, were used. Excellent agreement was found between the spherical cavity expansion

solution and experimental values of penetration resistance. A low value of cylindrical cavity expansion pressure relative to that for spherical cavity expansion pressure indicates that plane strain penetrators should be superior to long rod penetrators.

The dynamic cavity expansion problem with spherical symmetry was solved using two different methods. The solution using elastic wave propagation theory yielded trends in the penetration resistance of AD995 alumina that are in agreement with experiments. Effects of shear saturation in the failed material was studied using a self similarity transformation. This solution agreed and showed correct trends with the experimental data. The dynamic solution showed that the penetration resistance (Tate resistance) of AD995 alumina ceramic remains at a nearly constant level (equal to static cavity expansion pressure) until a penetration velocity of 2.5 km/s.

Cavity expansion analysis was also employed to model the effects of finite boundaries of ceramic tiles in ceramic/ metal layered targets. Superior agreement was obtained with experimental data compared to that obtained by the traditional approach of using a constant resistance value.

A new model for linear penetration of metal targets was hypothesized, that relates spherical cavity expansion pressure to the pressure on the projectile nose. For tenable values of the failure strain, excellent agreement was achieved for a variety of experimental data sets for both low speed and high speed penetrations. This model showed superior prediction of penetration depth compared to existing penetration models.

5.2   Conclusions

A single value of friction coefficient results in excellent agreement between experimental data and theoretical predictions for spherical and conical punches and before and after the embedment of the tip. Thus punch tests can be used to determine the friction coefficient. Spherical cavity expansion pressure gives a good approximation for the penetration resistance of both metallic and ceramic target materials. This agreement is better than for cylindrical cavity expansion pressure. For finite targets, whether metal or ceramic, penetration resistance decreases with decreasing thickness. It follows that when evaluating ceramics in a DOP configuration, thickness of the ceramic tile and the metallic substrate must be taken into account.

The analysis of brittle materials reveals the parameters that are most important for achieving high penetration resistance. They are the one-dimensional compressive strength, Young's modulus and the slope of pressure-shear coefficient of the failed material. The shape of the

pressure-dependent shear behavior of the fracture curve does not appear to influence the penetration resistance of ceramics. Thus, the confined compressive strength (i.e., Hugoniot elastic limit) is not directly relevant to penetration resistance. The dynamic cavity expansion analyses showed that the penetration resistance of ceramic targets (Tate resistance) remains at nearly a constant value (compared to metals, whose penetration resistance strongly decreases with velocity) equal to the static spherical cavity expansion pressure until a penetration velocity of 2.5 km/s. Thus ceramics should be effective material for armor applications to counter hypervelocity projectiles.

The predictions from the new hypothesized penetration model for ductile materials yield excellent agreement with several sets of data at all velocities. However, the hypothesis needs experimental verification. This model indicates that the penetration depth always increases with velocity; thus the existence of the "hydrodynamic limit" in penetration of ductile materials, as postulated by conventional theory, will not exist.

5.3   Suggested future work

The behavior of failed ceramic is the subject of current research. A limited number of experiments exist, which indicate that above the HEL, the shear strength of the failed ceramic is constant. However, interpretation of these results is problematic, because it is unlikely that the material behind the shock is fully comminuted. Thus, a few representative values for the saturated shear strength of the failed material were considered for Al_2O_3 ceramic. Plate impact and bar impact experiments on failed ceramics would establish the level of saturated shear strength.

The cavity expansion analysis needs to be extended for finite ceramic tiles backed by a finite metal substrate to determine the utility of evaluating different ceramic materials in DOP configuration. The minimum thickness of the metallic substrate required to make it behave as an infinite medium should depend on the overlying ceramic and the impact velocity. This analysis would enable one to better interpret DOP tests and predict armor performance. Additionally, presence of the low impedance bonding agent between the laminates must be considered to explain the experimentally observed degradation of penetration resistance of thick ceramic tiles. The penetration resistance degradation model for finite targets can be used to describe behind-the-armor characteristics for the break-out situation. Before this can be achieved, a model is required for capturing the modes of break-out, i.e., shearing, plugging etc.

The cavity expansion analysis presented in this dissertation may be extended to include layered brittle materials and functionally graded materials. Another interesting extension of this analysis would be to model the phenomena of "interface defeat," in which the projectile is defeated at the ceramic/metal interface under suitable test configuration.

The hypothesis that the material surrounding the penetration cavity in the metallic target is incompressible and that extensive shear flow is restricted to this region needs experimental verification. The post-test target material should be sectioned and the micro-structure surrounding the penetration cavity must be studied. If this hypothesis is true, one must observe a damaged region of extensive straining and fluid-like flow is manifested by the presence of extruded parallel thin layers (probably a few grains thick). The surrounding compressible plastic region should demonstrate only plastic deformation, primarily within the grains themselves. The demarcation of extreme deformation by inter-granular flow and the plastic-deformation inside the grains should define the extent of the failed region. The change in density can be investigated by electrical resistance measurement and measurements of ultrasonic wave propagation.

Acknowledgment

REFERENCES

Alekseevskii, V. P., 1966, "Penetration of a Rod into a Target at High Velocity," *Fiz. Goren. Vzryra*, 2, 99.

Anderson, C. E., Johnson, G. R. and Holmquist, T. J., 1995, "Ballistic Experiments and Computations of Confined 99.5 % AI$_2$O$_3$ Ceramic Tiles," 15th International Symposium on Ballistics, Jerusalem,Israel, May, 1995.

Anderson, C. E., Littlefield, D. L. and Walker, J. D., 1993, "Long Rod Penetration, Target Resistancece, and Hypervelocity Impact," *Int. J. Impact Engng.*, Vol. 14, pp 1 -12.

Anderson, C. E., and Walker, J. D., 1991, "An examination of long rod penetration," *Int.J. Impact Engng.*, V14, pp.85-93

Anderson, C. E., Walker, J. D., Bless, S. J. and Partom, Y., 1996, "On The L/D Effect for Long Rod Penetrators," *Int. J. Impact. Engng.*, Vol. 18, No. 3, pp 247 - 264.

Arhens, T. J., Gust, W. H. and Royce, E. B., 1968, "Material Strength Effects in the Shock Compression of Alumina," *J. Appl. Phys.*, 39:4610.

Asay, J. R., and Shahinpoor, M, 1993, *High-Pressure Shock Compression of Solids*, Springer-Verlag, New York.

Awerbuch, J., and Bodner, S. R., 1974, "Analysis of the Mechanics of Perforation of Projectiles in Metallic Plates," *Int. J. Solids Structures*, Vol. 10, pp. 671- 684.

Backman, M. E., and Goldsmith, W., 1977, "The Mechanics of Penetration of Projectiles into Targets," *Int. J. Engng. Sci.*, Vol. 16, pp.1-99.

Barenblatt, G. I., 1979, *Similarity, Self-Similarity, and Intermediate Asymptotics*, Consultants Bureau, New York.

Batra, R. C., and Write, T. W., "Steady State Penetration of Rigid Perfectly Plastic Targets," *Int.J.Engng.Sci.*, Vol.24,n-1,pp.41-54,1986.

Bishop, R.F., Hill, R., and Mott, N.F., 1945, "The Theory of Indentation and Hardness Tests," *The Proceedings of the Physical Society*, Vol.57, Part 3, pp.147-159.

Bless, S. J., 1996, "Penetration Mechanics of Non-Circular Rods," in *Shock Compression of Condensed Matter-1995*, eds. S. C. Schmidt, W. C. Tao, Americal Institute of Physics.

Bless, S. J., 1997, private communication.

Bless, S. J., and Anderson, C. E., 1993, "Penetration of Hard Layers by Hypervelocity Rod Projectiles," *Int. J. of Impact Engng.*, Vol. 4, pp. 85 - 93.

145

Bless, S. J., and Brar, N. S., 1994, "Impact Induced Fracture of Glass Bars," in *High-Pressure Science and Technology-1993*, Americal Institute of Physics.

Bless, S. J., Brar, N. S., Kanel, G., and Rosenberg, G., 1992, "Failure Waves in Glass," *J. Am. Ceram. Soc.*, **75**, 1002-1004.

Bless, S. J., Brar, N. S., and Rosenberg, Z., 1990, "Failure of Ceramic and Glass Rods Under Dynamic Compression," in *Shock Compression of Condensed Matters*, eds. S. C. Schmidt et al., Elsevier Science Publishers.

Bless, S. J., Gooch, W., Satapathy, S., Campos, J., and Lee, M., 1997, "Penetration Resistence of Titanium and Ultra-hard Steel at Elevated Velocities," to appear in the *Int. J. Impact Engng.*

Bless, S. J., and Lee, M. Y., 1996, "Cavity Dynamics for Long Rod Penetration," IAT.R.0094, Institute for Advanced Technology, University of Texas at Austin.

Bless, S. J., and Lopatin, C., 1988, "Impact Behavior of Ceramics," Symp. on Dynamic Constitutive/ Failure Models, University of Dayton, OH.

Bless, S. J., and Rajendran, A. M., 1995, "Initiation and Propagation of Damage Caused by Impact on Brittle Materials," in *High Pressure Shock Compression of Solids II* (edited by L. Davinson, D. E. Grady and M. Shahinpoor), Springer, New York.

Bless, S. J., Rosenberg, Z., and Yoon, B., 1987, "Hypervelocity Penetration of Ceramics," *Int. J. Impact Engng.*, vol. 5, pp. 165.

Bless, S. J., Satapathy, S., and Simha, C.H.M., 1996, "Response of Alumina Ceramics to Impact and Penetration," in *Structures Under Shock and Impact IV*, eds. N. Jones, C. A. Brebbia, A. J. Watson, Computational Mechanics Publications, Southamton, UK.

Bless, S. J., Subramanian, R., Anderson, C. E., Jr., and Littlefield, D. E., 1993, "Prediction of Large Scale High Velocity Penetration Experiments on Ceramic Armor," Army Symp. on Solid Mechanics, Plymouth, MA.

Bless, S. J., Subramanian, R., Lynch, N., and Partom, Y., 1995, "Effects of Radial Confinement on the Penetration Resistance of Thick Ceramic Tiles," 15th International Symposium Ballistics, Jersusalem.

Brar, N., Bless, S. J., and Rosenberg, Z., 1988, "Brittle Failure of Ceramic Rods Under Dynamic Compression," *J. de Physique* C-C3, vol. 9, pp. 607-612.

Cagnoux, J., and Langy, F., 1987, "Is the Dynamic Strength of Alumina Rate Dependent?," in *Shock Waves in Condensed Matters* (edited by S. C. Schmidt and N. C. Holmes), Elsevier Sciences.

Cazamias, J., and Bless, S. J., 1997, "Scaling Effects in Penetration: A Taylor Test Approach," to appear in the *Proceedings of Dymat, 97*, Toledo, Spain.

Chadwick, P., 1959, "The Quasi-static Exapansion of a Spherical Cavity in Metals and Ideal soil," *Quart. Journ. Mech. and Applied Math.*, Vol. XII, Pt. 1.

Clifton, R. J., Ortiz, M., Camacho, F., and Sairam, S., 1995, "Penetration Simulation and Dynamic Response of Comminuted Ceramics," 12th Ceramics Modelling Working Group Meeting, Institute for Advanced Technology, Austin, TX.

Collombet, F., and Tranchet, J. Y., 1994, "Damage Behavior of Alumina Submitted to a Divergent Spherical Wave," *Journal De Physique IV*, C8-641 - C8-646.

Cosculleula, A., 1992, "Plasticite, Engdommagements, et Ruptures des Alumines Sous Sollicitations Dynamiques Triaxiales: Influence de la Taille des Grains," Thesis, University of Bordeaux I.

Courant, R., and Friedrichs, K. O., 1948, *Supersonic Flow and Shock Waves*, Springer-Verlag, New York.

Curran, D. R., Seaman, L., Cooper, T., and Shockey, D. A., 1993, "Micromechanical Model for Comminution and Granular Flow of Brittle Material under High Strain Rate Application to Penetration of Ceramic Targets," *Int. J. Impact Engng.*, vol. 13, no. 1, pp. 53-83.

Curran, D. R., Seaman, L., and Shockey, D. A., 1990, "Dynamic Failure of Solids," *Physics Reports* (Review Section of Physics Letters), 147, Nos. 5 & 6, pp. 253 - 388.

Dandekar, D. P., and Bartkowski, P., 1993, "Shock Response of AD995 Alumina," in *High Pressure Science and Technology - 1993*, eds. S. C. Schmidt et al., 733-736, A.I.P., 1994.

Donaldson, C. duP., and McDonough, T. B., 1973, "A Simple Integral Theory for Impact Cratering by High Speed Particles," Defense Nuclear Agency, DNA 3234F.

Durban, D., and Baruch, M., 1976, "On the Problem of a Spherical Cavity in an Infinite Elasto-Plastic Medium ," *J. of Appl. Mech.*, pp 633 - 638.

Florence, A. L., Gefken, P. R., Seaman, L., Curran, D. R., and Shockey, D. A., 1992, "Computational Models for Armor Penetration," SRI Project PYD-8521.

Forrestal, M. J., 1986 "Penetration into Dry Porous Rock," *Int. J. Solids Structures.*, Vol.22, No. 12, pp. 1485 - 1500.

Forrestal, M. J., 1997, private communication.

Forrestal, M.J., Brar, N. S., and Luk, V.K., 1991, "Penetration of Strain-Hardening Targets with Rigid Spherical-Nose Rods," *Journal of Applied Mechanics*, Vol.58, pp.7-10

Forrestal, M. J., and Longcope, D. B., 1990, "Target Strength of Ceramic Materials for High-Velocity Penetration," *J. Appl. Phys.*, vol. 67, pp. 3669-3672.

147

Forrestal, M. J., Longcope, D. B., and Norwood, F. R.,1981, "A Model to Estimate Forces on Conical Penetrators into Dry Porous Rock," *Journal of Applied Mechanics.*,Vol. 48 / 25 - 29.

Forrestal, M. J., and Luk, V.K., 1988, "Dynamic Spherical Cavity-Expansion in a Compressible Elastic-Plastic Solid," *Journal of Applied Mechanics*, Vol. 55, pp. 275-279.

Forrestal, M. J., Okajima, K., and Luk, V. K., 1988, "Penetration of 6061-T651 Aluminum Targets with Rigid Long Rods," *ASME J. of App. Mech.*, vol. 55, pp. 755-760.

Forrestal, M. J., and Tzou, D. Y., 1997, "A Spherical Cavity-Expansion Penetration Model for Concrete Targets," to appear in the *Int. J. Solids & Structures.A*

Forrestal, M. J., Tzou, D. Y., Askari, E., and Longcope, D. B., 1995, "Penetration into Ductile Metal Targets with Rigid Spherical-Nose Rods," *Int. J. Impact Engng.* Vol. 16, No. 5/6, pp 699 -710.

Gehring, J. W., Meyers, C. L., and Charest, J. A., 1965, "Experimental Studies of Impact Phenomena and Correlation With Theoretical Models," *Proc. 7th Symp. on Hypervelocity Impact*, Tampa, FL.

Goodier, J. N., 1965, "On The Mechanics of Indentation and Cratering In Solid Targets of Strain-Hardening Metal by Impact of Hard and Soft Spheres," *Proc. 7th Symp. Hypervelocity Impact III, AIAA*, NY.

Grady, D. E., 1995, "Dynamic Properties of Ceramic Materials," Sandia Report, Sand 94-3266.UC-704.

Graff, K., 1975, *Wave Motion in Elastic Solids*, Dover Publications, Inc., New York.

Hanagud, S., and Ross, B.,1971, "Large Deformation, Deep Penetration Theory for a Compressible Strain-Hardening Target Material," *AIAA Journal*, Vol. 9, No.5.

Hancock, J. W., and Mackenzie, A. C., 1976, "On the Mechanicsms of Ductile Failure in High-Strength Steels Subjected to Mult-axial Stress-State," *J. Mech. Phys. Solids*, Vol. 24, pp. 147 - 169.

Hauver, G. E., Netherwood, P. H., Benck, R. F., Gooch, W. A., Perciballi, W. J., and Burkins, M. S., 1992, "Variation of Target Resistance During Long Rod Penetration into Ceramics," 13th Int'l. Symp. Ballistics, Sweden.

Hermann,W., and Wilbeck, J.S., 1987, "Review of Hypervelocity Penetration Theory," *Int. J. Impact Engng.*, Vol.5, pp.307-322.

Hill, R., 1948, "A Theory of Earth Movement Near a Deep Underground Explosion," Memo No. 21-48, Armament Research Establishment, Fort Halstead, Kent, U.K.

Hill, R., 1950, *The Mathematical Theory of Plasticity*, Oxford University Press, London.

Hohler, V., and Stilp, A. J., 1987, " Hypervelocity Impact of Rod Projectiles," *Int. J. Impact. Engng.*, Vol. 5, pp. 323 -331.

Hohler, V., and Stilp, A. J., 1990, "Long-Rod Penetration Mechanics," in *High Velocity Impact Dynamics*, edited by Zukas, J. A., John Wiley & Sons, Inc., NewYork.

Hohler, V., and Stilp, A. J., 1992, *A Penetration Mechanics Database* (edited by C. E. Anderson, B. L. Morris and D. L. Littlefield) SWrI Report 3593/001, Southwest Research Institute, San Antonio, TX.

Hopkins, H. G., 1960, "Dynamic Expansion of Spherical Cavities in Metal," in *Progress in Solid Mechanics*, Vol. 1, Chapter III (edited by I. N. Sneddon and R. Hill), North-Holland Publishing Co., Amsterdam, NY.

Huang, W., Murr, L. E., Niou, C. S., Rupert, N. L., Grace, F. I., and Bless, S. J., 1996, "Microstructural Observations and Comparison for Some Rod Penetrated Metal and Alloy Targets," *Proceedings of the 16th Int. Symp. on Ballistics*, San Francisco, CA.

Huang, Y., Hutchinson, J. W., and Tvergaard, V., 1991, "Cavitation Instabilities in Elastic-Plastic Solids," *J. Mech. Phys. Solids.* Vol. 39, No. 2, pp 223 - 241.

Hunter, S. C., and Crozier, R. J. M.,1968, "Similarity Solution for the Rapid Uniform Expansion of a Spherical Cavity in a Compressible Elastic-Plastic Solid," *Quart. Journ. Mech. and Applied Math.*, Vol XXI, Pt.4.

Johnson, 1972, *Impact Strength of Materials*, Edward Arnold, London

Johnson, G. R., and Holmquist, T. J., 1992, "A computational Constitutive Model for Brittle Materials Subjected to Large Strains, and High Pressures," in *Shock-Waves and High-Strain-Rate Phenomenain Materials*, ed. M. A. Meyers, L. E. Murr, K. P. Staudhammer, Marcel Dekker.

Kipp, M. E., and Grady, D. E., 1994, "Shock phase transformation and release properties of aluminum nitride," *Journal de physique*, vol 4, pp c8-249-c8-256.

Klopp, R. W., Shockey, D. A., Seaman, L., Curran, D. L., and McGinn, J. T., 1994, "A Spherical Cavity Expansion Experiment for Characterizing Penetration Resistance of Armore Ceramics," *Proc. ASME Symp. on Mech. Testing of Ceramics and Ceramics Composites*, Chicago, IL.

Lanz, W., and Odermatt, W., 1992, "Penetration Limits of Conventional Large Caliber Anti-Tank Guns / Kinetic Energy Projectiles," *Proc. 13th Int. Symp. on Ballistics, Vol. 3*, FOA, Sweden.

Lee, J. W., and Satapathy, S., 1994, "Comparison of Measured Target Resistance and Predictions from Cavity Expansion Models for Polymethyl Methacrylate," IAT. TN. 0028, Institute for Advanced Technology, University of Texas at Austin.

Littlefield, D. L., Anderson, C. E., Partom, Y., and Bless, S. J., 1997, "The Penetration of Steel Targets Finite in Radial Extent," *Int. J. Impact Engng.*, Vol. 19, n. 1, pp.49 - 62.

Littlefield, D. L., Anderson, C. E., and Skaggs, S. R, 1994, "Analysis of Penetration of Steel and Al203 Targets," in High-Pressure Science and Technology-1993, ed. S. C. Schmidt, J. W. Shaner, G. A. Samara, and M. Ross, Americal Institute of Physics, Woodbury, NY.

Luk, V. K., Forrestal, M. J., and Amos, D. E.,1991, "Dynamic Spherical Cavity Expansion of Strain-Hardening Materials," *Journal of Applied Mechanics*, Vol. 58/1 -6.

Macdougal, D., and Harding, J., 1995, "High Strain Rate Behavior of Ti6Al4V," in *Metalurgical and Materials Applications of Shock-Wave and High-Strain-Rate Phenomena*, edited by L. E. Murr, K. P. Staudhammer and M. A. Meyers, Elsevier Science, pp. 909 - 916.

Marsh, S. P., 1980, *LASL Shock Hugoniot Data*, University of California Press, Berkeley, CA.

McClintock, F. A., 1968, "A Criteria for Ductile Fracture by the Growth of Holes," *J. Appl. Mech.*, pp. 363 - 371.

Mendelson, A, 1968, *Plasticity: Theory and Applications*, Robert E. Krieger Publishing Co.

Normandia, M. J., and Littlefield, D. L., 1996, "RHA Breakout Effects for Tungsten Alloy Penetrators," 7th Annual TARDEC Combat ·Survivability Symposium, vol. I., Naval Postgraduate School, Monterey, March 26-28.

Normandia, M. J., Satapathy, S., Littlefield, D. L., and Anderson, C. E., "Modified Cavity Expansion Analysis for Modeling Finite Target Penetration," 16th International Symphosium on Ballistics, San Francisco, CA.

Olsson, P. O., Lundberg, P., and Ragharsson, K., 1995, "Post-Mortem Studies to Investigate Replica Modelling of Alumina Targets," 15th International Symposium Ballistics, Jerusalem.

Orphal, D. L., Franzen, R. R., Piekutowski, A. K., and Forrestal, M. J., 1996, "Penetration of Confined Aluminum Nitride Targets by Tungsten Long Rods at 1.5 to 4.5 km/s," *Int J. Impact Engng.,* vol. 18, pp. 355-368.

Partom, Y., 1993, "Analysis of SST-C Target Performance with Tate's Model," IAT.TN 0009, Institute for Advanced Technology, University of Texas at Austin.

Partom, Y., 1993, "Ceramic Armor Resistance to Long-Rod Penetration (R_t) and its Dependence on Projectile Velocity," IAT.R 0017, Institute for Advanced Technology, University of Texas at Austin.

Partom, Y., 1996, "Cavity Expansion Model for Partially Confined Targets," 16th International Ball Symposium, San Francisco, CA.

Partom, Y., and Littlefield, D. L., 1993, "Dependence of Ceramic Armor Resistance on Projectile Velocity," *Proceedings of the 14th International Ballistics Symposium*, Quebec, vol. 2, pp. 563-572.

Raftenberg, M. N., 1994, "Lagrangian Hydrocode Simulations of Rolled-Homogeneous-Armor Plate Perforation by a Shaped Charged Jet," *Int. J. Impact Engng.*, Vol. 15, No. 5, pp. 619 - 643.

Raftenberg, M. N., and Kennedy, E. W., 1995, "Steel Plate Perforation by Tungsten Rods of Small L/D," *Proceedings of the 15th Int. Symp. on Ballistics*, ed. M. Mayseless, Jerusalem.

Raiser, G., and Clifton, R. J., 1993, "High Strain Rate Deformation and Damage in Ceramic Materials," *Transactions of the ASME*, Vol. 115, pp. 292 - 299.

Rajendran, A. M., 1993, "Modeling the Impact Behavior of High Strength Ceramics," ARL-TR-224, Army Research Laboratory, Watertown, MA.

Rajendran, A. M., and Bless, S. J., 1986, "Determination of Tensile Flow Stress Beyond Necking at Very High Strain Rate," *Expt. Mech.*, Vol. 26, n-4, pp. 319 - 323.

Rajendran, A. M., and Cook, W. H., 1988, "A Comprehensive Review of Modeling of Impact Damage in Ceramics," UDR-TR-88-125, University of Dayton, OH.

Recht, R. F., 1978, "Taylor Ballistic Impact Modelling Applied to Deformation and Mass Loss Determinations," *Int. J. Engng. Sci.*, Vol. 16, pp. 809 - 827.

Recht, R. F., and Ipson, T. W., 1963, "Ballistic Perforation Dynamics," *J. Appl. Mech.*, Vol. 30, No. 3.

Rice, J. R., and Tracy, D. M., 1969, "On the Ductility Enlargement of Voids in Triaxial Stress Fields," *J. Mech. Phys. Solids*, Vol. 17, pp. 201 - 217.

Rosenberg, Z., Brar, N. S., and Bless, S. J., 1991, "Dynamic high-pressure properties of AlN ceramics as determined by flyer plate impact," *J. Appl. Phy.*, 70(1), pp 167-171.

Rosenberg, Z., Marmor, E., and Mayseless, M., 1990, "On the hydrodynamic theory of long-rod penetration," *Int. J. Impact Engng.*, 10, 483-486.

Rosenberg, Z., and Tsaliah,J., 1990, "Applying Tate's model for the Interaction of Long Rod Projectiles with Ceramic Targets," *Int. J. Impact Engng.*, vol.9, pp.247.

Rosenberg, Z., Yaziv, D., Yeshurun, Y., and Bless, S. J., 1987, "Shear Strength of Shock-loaded Alumina as Determined with Longitudinal and Transverse Manganin Gauges," *J. Appl. Phys.*, Vol. 62, No. 3, pp. 1120 - 1122.

Sairam, S., and Clifton, R. J., 1994, "Pressure-Shear Impact Investigation of Dynamic Fragmentation and Flow of Ceramics," *Proc. of ASME Winter Annual Meeting*.

Satapathy, S., and Bless, S. J., 1995, "Quasi-Static Penetration Tests of PMMA: Analysis of Strength and Crack Morphology," IAT. R 0069, Institute for Advanced Technology, University of Texas at Austin.

Satapathy, S., and Bless, S. J., 1996, "Calculation of Penetration Resistance of Brittle Materials Using Spherical Cavity Expansion Analysis," *Mech. Materials*, Vol. 23, pp. 323 - 330.

Scott, B. R., 1984, "Radial Expansion of Cavities Produced by Axi-symmetric Steady Penetration of Hypervelocity Rods," Ph.D. Dissertation, University of Delaware, Newark, DE.

Shanbing, Y., Genchen, S., and Quingming, T., 1994, "Experimental laws of cratering for hypervelocity impacts of spherical projectiles into thick targets," *Int. J. Impact Engng.*, Vol. 15, n. 1, pp. 67-77.

Shockey, D. A. , Marchand, A. H., Skaggs, S. R., Cort, C. E., Burkett, M. W., and Parker, R., 1990, "Failure Phenomenology of Confined Ceramic Targets and Impacting Rods," *Int J. Impact Engng.*, vol. 9, pp. 263-275.

Silsby, G. F., 1984, "Penetration of Steel Targets by Tungsten Long Rods at 1.3 to 4.5 km/s," *Proc. 8th Int. Symp. on Ballistics*, TB31-TB36, Orlando, FL.

Silsby, G. F., Sorensen, B. R., Kimsey, K. D., Scheffler, D. R., Sherrick, T. M., and deRosset, W. S., 1989, "High Velocity Penetration: An. Experimental and Numerical Perspective," Hypervelocity Impact Symposium, San Antonio, TX.

Simha, C. H., Bless, S. J., and Brar, N. S., 1995, "Dynamic failure of AD995 Alumina," EXPLOMET '95, Int. Conf. on Metallurgical and Material application of Schock-wave and high-strain-rate phenomena, EL Paso, TX.

Steinberg, D. J., 1991, "Equation of State and Strength Properties of Selected Materials," Lawrence Livermore Nat. Lab., UCRL-MA-106439.

Sternberg, J., 1989, "Material Properties Determining the Resistance of Ceramics to High Velocity Penetration," *J. Appl. Phys.*, vol. 65, pp. 3417-3424.

Strassburger, E., Senf, H., and Rothenäusler, 1994, "Fracture Propagation During Impact In Three Types of Ceramics," *J. de Physique IV*, C8-653–658.

Subramanian, R., and Bless, S. J., 1995, "Penetration of Semi-Infinite AD995 Alumina Targets by Tungsten Long Rod Penetrators from 1.5 to 3.5 km/s," *Int'l. J. Impact Engng.*, vol 17, 807-816.

Tate, A., 1967, "A Theory for the Deceleration of Long Rods After Impact," *J. Mech. Phys. Solids*, Vol. 15, 387-399.

Tate, A., 1969, "Further Results in the Theory of Long rod Penetration," *J. Mech. Phys. Solids*, 17, 141-150.

Tate, A., 1978, "A Simple Hydrodynamic Model for The strain Field Produced in a Target by the Penetration of a High Speed Long Rod Projectile," *Int. J. Engng. Sci.*, Vol. 16. pp. 845 - 858.

Tate, A., 1986, "Long Rod Penetration Models - Part I. A Flow Field Model For High Speed Long Rod Penetration," *Int. J. Mech. Sci.*, Vol. 28, No. 8, pp 535 -548.

Tate, A., 1986, "Long Rod Penetration Methods - Part II. Extensions to the hydrodynamic theory of penetration," *Int. J. Engng Sci.*, 28(9), 599-612.

Timoshenko, S. P., and Goodier, J. N., 1987, *Theory of Elasticity*, 3rd edition, McGraw-Hill, Inc., New York, p. 406.

Tham, R., Schneider, E., and Stilp, A. J., 1980, "Metallographic Investigations on Phase Transitions in Impact Loaded Steels," in High Pressure Science and Technology, eds. B. Vodar, Ph. Marteau, Permagon Press, New York.

Walker, J. D., and Anderson, C. E., 1995, "A Time Dependent Model for Long Rod Penetration," *Int. J. Impact. Engng.*, Vol. 16, No. 1, pp. 19 - 48.

Warren, T. L., and Forrestal, M. J., 1997, "Effects of Strain Hardening and Strain-Rate Sensitivity on the Penetration of Aluminum Targets With Spherical-Nosed Rods," in press.

Weirauch, G., 1971, "Das Verhalten von Kupferstiften beim Auftreffen auf verschiedene Werkstoffe mit Geschwindigkeiten zwischen 50m/s und 1650 m/s," Ph.D. Dissertation, University of Karlsruhe.

Wilkins, M. L., and Guinan, M. W., 1973, "Impact of Cylinders on a Rigid Boundary," *J. Appl. Phys.*, Vol. 44, No. 3.

Woo, H. J., 1997, Ph.D. Thesis, University of Texas at Austin (forthcoming).

Woolsey, P., 1992, "Ceramic Materials Screening by Residual Penetration Ballistic Testing," 13th Int. Symp. on Ballistics, Stockholm, Sweden.

Wright, S. C., Huang, Y., and Fleck N. A., 1992, "Deep Penetration of Polycarbonate by a Cylindrical Punch," *Mech. Mat.*, vol. 13, pp. 277-284.

Wright, T. W., 1981, "Penetration with Long Rod: A Theoretical Framework and Comparison with Instrumented Impacts," ARBRL-TR-02323, U.S. Army Ballistic Research Laboratory, Aberdeen Proving Ground, MD.

Wright, T. W., 1983, "A Survey of penetration mechanics for long rods," in *Computational Aspects of Penetration Mechanics* (edited by J. Chandra and J.E. Flaherty), Lecture Notes in Engineering, 3, pp.85-106. Springer-Verlag, Berlin-Heidelberg.

Wright, T. W., and Frank, K., 1988, "Approaches to Penetration Problems," in *Impact: Effects of Fast Transient Loading* (W. J. Ammann, W. K. Liu, J. A. Studer, and T. Zimmerman, Eds.), A.A. Balkema, Rotterdam.

Zukas, J. A., 1990, *High Velocity Impact Dynamics*, John Wiley & Sons, Inc., New York.

Distribution List

Administrator
Defense Technical Information Center
Attn: DTIC-DDA
8725 John J. Kingman Road,
Ste 0944
Ft. Belvoir, VA 22060-6218

Director
US Army Research Lab
ATTN: AMSRL OP SD TA
2800 Powder Mill Road
Adelphi, MD 20783-1145

Director
US Army Research Lab
ATTN: AMSRL OP SD TL
2800 Powder Mill Road
Adelphi, MD 20783-1145

Director
US Army Research Lab
ATTN: AMSRL OP SD TP
2800 Powder Mill Road
Adelphi, MD 20783-1145

Army Research Laboratory
AMSRL-CI-LP
Technical Library 305
Aberdeen Prvg Grd, MD 21005-5066

Thomas J. Ahrens
CALTECH 252-21
Pasadena, CA 91125

Dr. Charles Anderson, Jr.
Southwest Research Institute
Engineering Dynamics Department
P.O. Box 28510
San Antonio, TX 78228-0510

N. Singh Brar
University of Dayton Research Institute
300 College Park
Shroyer Park Center
Dayton, OH 45469-0182

Rodney J. Clifton
Brown University
Providence, RI 02912

Dr. Datta Dandekar
Army Research Laboratory
AMSRL-MA-PD
Aberdeen PG, MD 21005-5066

William de Rosset
U.S. Army Research Laboratory
Attn: AMSRL-WT-TC
Aberdeen Prvg Grd, MD 21005-5066

Horacio Espinosa
School of Aeronautics & Astronauts
Purdue University
West Lafayette, IN 47907

Dr. Michael Forrestal
Sandia National Laboratory
Division 1922
P.O. Box 5800
Albuquerque, NM 87185

Konrad Frank
U.S. Army Research Laboratory
Attn: AMSRL-WT-TD
Aberdeen Prvg Grd, MD 21005-5066

Dr. W. J. Gillich
U.S. Army Research Laboratory
AMSRL-WT-TA
Aberdeen Prvg Grd, MD 21005-5066

George Hauver
US Army Research Laboratory
ATTN: AMSRL-WT-TA
Aberdeen PG, MD 21005-5066

Manfred Held
DASA
POSTFACH 13 40
Schrobenhausen, 86 523
Germany

Dr. V. Hohler
Ernst Mach Institute
Eckerstrasse 4
7800 Freiburg i.BR
Germany

Kailasam Iyer
US Army Research Office
P.O. Box 1221
Research Triangle Park, NC 27709-2211

Dr. Gordon Johnson
Alliant Techsystems, Inc.
Marine Systems Division
600 Second St. NE
Hopkins, MN 55343

Gennady Kanel
Institute for High Temperatures
Moscow
Russia 127912

Distribution List

Valeriy V. Kartuzov
National Academy of Sciences of Ukraine
Frantzevich Institute for Problems of
Materials Science
Department 44
3, Krzhyzhanovsky Str.
252142, Kiev, Ukraine

Dr. A. M. Rajendran
US Army Research Lab
AMSRL-MA-PD
Aberdeen PG, MD 21005-5066

Anatoli Kozhushko
Russian Academy of Sciences
Ioffe Physical Technical Institute
Hypervelocity Impact Research Group
St. Petersburg
194021 Russia

J.Y. Tranchet
Centre d'Etudes Gramat
46500 Gramat
France

Dr. Hartmuth F. Lehr
Institute Saint Louis
5, Rue du General Cassagnou
Boite Postal 34
F-68301 Saint Louis, CEDEX
FRANCE

Bill Walters
U.S. Army Research Laboratory
WMRD
Attn: AMSRL-WM-TC
Aberdeen Pvg Grd, MD 21005

Nick Lynch
DERA Fort Halstead
Bldg. A 20, Div. WX5
Sevenoaks, Kent
England TN14 7BP

Mike Zoltoski
U.S. Army Research Laboratory
Attn: AMSRL-WM-TA
Aberdeen Prvg Grd, MD 21005-5066

V. F. Nesterenko
3175-C Evening Way
La Jolla, CA 92037

Mr. Dennis L. Orphal
International Research Associates
4450 Black Ave. Suite E
Pleasanton, CA 94566

Yehuda Partom
Rafael Ballistics Center
Box 2250
Haifa 31021
Israel